On unsteady open-channel flows : a contribution to nonstationary sediment transport in runoff flows and to unstable non-Newtonian mudflow studies

Guilherme Henrique Fiorot

Thèse

UNIVERSITE BRETAGNE LOIRE

THESE INSA Rennes
sous le sceau de l'Université Bretagne Loire
pour obtenir le titre de
DOCTEUR DE L'INSA RENNES
Spécialité : Génie Civil

présentée par

Guilherme Henrique Fiorot

ECOLE DOCTORALE : *SDLM*
LABORATOIRE : *LGCGM*

On unsteady open-channel flows: a contribution to non-stationary sediment transport in runoff flows and to unstable non-Newtonian mudflow studies

Erick DE MORAES FRANKLIN
Maître de Conférences habilité à l'UNICAMP, Brésil / Examinateur invité

Thèse soutenue le 01.07.2016
devant le jury composé de :

Alexandre VALANCE
Directeur de Recherche CNRS à l'Institut de Physique de Rennes / Président
Luigi FRACCAROLLO
Associate Professor à l'Università Degli Studi di Trento, Italie / Rapporteur
Ana Luiza DE OLIVEIRA BORGES
Professeur à l'Instituto de Pesquisas Hidráulicas, UFRGS, Brésil / Rapporteur
Edson DEL RIO VIEIRA
Maître de Conférences habilité à l'UNESP de Ilha Solteira, Brésil / Examinateur
Philippe FREY
Chargé de Recherche (HdR) à l'Irstea – Grenoble / Examinateur
Edith Beatriz CAMANO SCHETTINI
Professeur à l'Instituto de Pesquisas Hidráulicas, UFRGS, Brésil / Examinateur
Pascal DUPONT
Maître de Conférences (HdR) à l'INSA de Rennes / Directeur de thèse
Geraldo DE FREITAS MACIEL
Professeur à l'UNESP de Ilha Solteira, Brésil / Directeur de thèse

On unsteady open-channel flows: a contribution to non-stationary sediment transport in runoff flows and to unstable non-Newtonian mudflow studies

Guilherme Henrique Fiorot

En partenariat avec

Dedicated to myself...

The popular view that scientists proceed inexorably from well-established fact to well-established fact, never being influenced by any unproved conjecture, is quite mistaken. Provided it is made clear which are proved facts and which are conjectures, no harm can result. Conjectures are of great importance since they suggest useful lines of research.

— Alan Turing, Alan Turing: The Enigma

Acknowledgments

First of all, I want to register here my love for my family. Their kindness and love, specially during my PhD, helped (a lot) to struggle through and live the adventure of a thesis. I know they fought as hard as me against all the mixed feelings between my arrivals and departures during my nomad life.

Secondly, I would like to express my sincere gratitude to both my supervisors, Ass. Prof. Pascal Dupont and Prof. Geraldo de Freitas Maciel. They encouraged me and my project, from the begging until the very last moment, constantly inspiring me with self-trust and scientific valors.

I am very grateful to all members of the jury, from both sides of the Atlantic Ocean, Res. Dir. Alexandre Valance, Ass. Prof. Edson Del Rio, Ass. Prof. Luigi Fraccarollo, Prof. Edith Beatriz Camano Schettini, Res. Ass. Philippe Frey, Prof. Ana Luiza de Oliveira Borges and Ass. Prof. Erick de Moraes Franklin, who accepted to participate and contribute to this defense.

I reserve a special thanks for my friends and colleagues Wendy, Alexandre, Amandine, Matias, Nino, Ilham, Saly, Jianhua, Davood, Sambath, Mustapha, Layachi, Paul, Anh Duc, Deborah, Fabiana, Evandro, André, Larissa, Juliana, Ter, Augusto, Leticia, Cinthia, Leticia, Felipe and everybody else that at some point exchanged some words of support and ordinary daily life with me. For their support, patience and, above all, their friendship, my sincere thanks. Without them I don't think I would have been able to find the strength to persevere and endure given the obstacles that have presented in my path. Moreover, I know I'm not easy guys... ;-)

I cannot leave all staff from the PPGEM, LGCGM & GCU without my deepest thanks. Nathalie, Emmanuelle, Jacqueline, Jean-Luc, Jean-Yves, Raphael, Anne, Carole, Etienne, Christian, Franck, Onilda, Marcia, Graciele, Rafael, Patrick, all of them participate in this whole process and for their professional support (et aussi pour les précieux moments de papotage/e também pelos momentos de jogar conversa fora) they hold my gratitude.

I thank also the researchers and professors from PPGEM, LH2, LGCGM and IPR, for their open minds and for sharing their knowledge. That's how I believe Science is done.

At last, but not least, I'm very grateful to every chaotic event in the Universe that allowed me to get this far.

Contents

Abstract **x**

Resumo **xii**

Résumé Etendu **xv**

List of Figures xxv

List of Tables xxxiv

Notation **xxxvi**

General overview **1**

1 Natural flows and risks 3
- 1.1 Introduction . . . 3
- 1.2 Phenomenological description . . . 6
- 1.3 Objectives . . . 11

2 Physical and mathematical review 13
- 2.1 Introduction . . . 13
- 2.2 Turbulent flow and sediment transport . . . 18
  - 2.2.1 Flow hydraulics . . . 18
  - 2.2.2 Sediment transport . . . 21
- 2.3 Laminar flow and non-Newtonian fluids . . . 26
- 2.4 Free surface instabilities - Roll waves . . . 29

I Sediment transport in runoff flows 39

3 Introduction 41

4 Experimental method 49
4.1 Materials and methods . . . 49
4.1.1 Experimental flume . . . 49
4.1.2 Flow measurements . . . 49
4.1.3 Sediment transport measurement . . . 54
4.1.4 Local measurements - Particle Tracking Velocimetry System (PTV) . . . 56
4.1.5 Wave generator . . . 60
4.2 Critical analysis of measurements . . . 61
4.2.1 Sediment transport test . . . 61
4.2.2 Grain-size distribution through images . . . 64
4.2.3 Qualitative analysis and temporal partitioning of signals . 65
4.2.4 Measurements of mean solid discharge . . . 67

5 Measurements of unsteady sediment transport 71
5.1 Flow hydraulics of steady conditions . . . 71
5.1.1 Base flow . . . 71
5.1.2 Turbulent properties . . . 74
5.1.3 Friction velocity . . . 76
5.2 Turbulence effects on sediment transport . . . 81
5.2.1 Mean solid discharge . . . 81
5.2.2 Fluctuations intensities in solid discharge . . . 82
5.2.3 Spectral properties of time dependent solid discharge . . . 85
5.3 Pulsating flow . . . 89
5.3.1 Mean solid discharge . . . 90
5.3.2 Fluctuations intensities in solid discharge . . . 92
5.3.3 Spectral properties . . . 93

II Non-Newtonian fluid flows over natural environments 97

6 Introduction 99

7 Application of mathematical model to natural events: the Acquabona creek 103
7.1 Mathematical and numerical modeling of roll waves . . . 103
7.2 Site description . . . 107
7.3 Event sample . . . 109
7.4 Parameters gathering . . . 110

7.5 Prediction results . . . 112
7.6 Non-Newtonian effect on maximum wave prediction . . . 113
7.7 Roll waves modeling as a risk assessment tool . . . 113

8 Search for a more complex model 119
8.1 Introduction . . . 119
8.2 Mathematical development . . . 120
8.2.1 Boundary Condition . . . 120
8.2.2 The velocity profile $u(y)$ . . . 123
8.2.3 Mean flow velocity u_0 . . . 124
8.3 Verification of solution for less complex conditions . . . 124
8.3.1 Bingham rheology . . . 124
8.3.2 Power law rheology . . . 125
8.3.3 Newtonian rheology . . . 125

9 Numerical simulations 127
9.1 Numerical modeling . . . 128
9.2 Numerical results . . . 129
9.2.1 Flow inside the porous medium . . . 129
9.2.2 Open-channel flow . . . 131
9.2.3 Boundary conditions verification . . . 134
9.3 Mathematical analysis . . . 135

10 Revisiting Acquabona 139
10.1 Parameter gathering . . . 139
10.2 Recalculating Acquabona event . . . 140

III Final remarks 145

11 Discussion and conclusions 147
11.1 Runoff flows and time-variable transport . . . 148
11.1.1 Experimental method . . . 148
11.1.2 Time-dependent solid discharge in turbulent permanent flow 149
11.1.3 Time-dependent solid discharge in pulsating flows . . . 150
11.2 Mathematical models for free surface instabilities in mudflows . . . 152
11.2.1 Acquabona test-case . . . 152
11.2.2 More complex model for non-Newtonian flows in natural environment . . . 153

12 Perspectives 155
12.1 Part I - Sediment transport in runoff flows . . . 155
12.1.1 Technical improvements . . . 155
12.1.2 Statistical analysis of particle counting events . . . 156

12.1.3 Mathematical model bottom shear stress on roll waves regime 156
12.2 Part II - Non-Newtonian fluid flows over natural environments . . 156
12.2.1 Mathematical modeling and validation 156
12.2.2 Non-Newtonian fluid flow over porous medium 157

Bibliography 159

On unsteady open-channel flows: a contribution to non-stationary sediment transport in runoff flows and to unstable non-Newtonian mudflow studies

This thesis was motivated by the need to better understand time-dependent features related to mudflow evolution on natural sloped channels. Basically, the research is focused on events that are confined in channels formed due to the topography. The rain, source of the liquid discharge, generates the runoff flow which is responsible for wetting the soil surface, promoting reduction of soil cohesiveness and erosion of small particles such as clay and sand. From this point, the sediment transport can increase as small water flows merge and form greater streams. The scenario keeps its evolution until it reaches high concentration of particles in the fluid mixture.

In the first part, to study the non-permanent feature of sediment transport, an open-channel experiment was designed for simulating runoff flow over a mobile bed. A measurement system was designed and constructed to instantaneously inspect the solid discharge of particles and the flow friction at the bed. This apparatus is further used to explore the influence of free-surface waves on the sediment transport. Hydraulic properties of flows are qualitatively and quantitatively studied and data are used to correlate characteristics of flow and sediment transport. A set of experimental runs is presented and explored. Analysis of results shows that for fixed flow conditions, waves induce an overall smaller quantity of transported sediment.

In a second part, the dynamics of high concentrated flows is addressed and this thesis attempts to apply a first-order roll-wave model for Herschel-Bulkley laminar fluid flow to a registered natural event. Results presented point out that roll waves could have occurred during this already published case-study event. Simulations could predict wave heights within 8% on uncertainty with respect to the mean amplitude of measured waves. Finally a new theoretical solution for the velocity profile is proposed taking into account the porosity of the bed. Results are then compared with numerical simulation performed in FLUENT. A parametric analysis is employed and the case-study is once again evaluated.

As general conclusion, the non-permanent phenomena that can appear during the evolution of a mudflow event affect the overall dynamics of the coupled system (hydraulic-sediment transport) in comparison to the steady and uniform case. Verifying that such phenomena could appear should indeed be an important part in hydraulic engineering projects, especially when dealing with lives, which is the case of mudflows.

Escoamentos não-permanentes de superfície livre : uma contribuição para o estudo do transporte não estacionário de sedimentos em escoamentos superficiais e para instabilidades em corridas de lamas

Dentro da temática de riscos naturais, mais precisamente no contexto das corridas de lama, esta tese surge da necessidade que existe na literatura em melhor se conhecer as características temporais destes eventos. A chuva, fonte da vazão liquida, conduz aos escoamentos superficiais, responsáveis pela redução da coesão do material sedimentar do solo (areia e argila) e seu consequente transporte. Em locais de topografia íngreme, de montante a jusante, a vazão sólida do escoamento principal pode, eventualmente, evoluir devido às contribuições laterais de pequenos escoamentos, alterando não só as propriedades reológicas do fluido e dinâmicas do escoamento, como se manter até que o transporte sólido atinja elevada concentração na composição do fluido.

Na primeira parte desta tese, um experimento de superfície livre foi projetado para reproduzir escoamentos superficiais sobre um fundo móvel, com o objetivo de estudar propriedades não-permanentes do transporte de sedimentos. Um sistema de medição foi projetado e construído com o intuito de medir quase instantaneamente a vazão solida e suas correlações com as propriedades hidráulicas do escoamento. Este aparato é também utilizado para observar a influência de instabilidades de superfície livre sobre o transporte. Um conjunto de resultados é apresentado e analisado e mostra que a presença de ondas pode, em média, reduzir a quantidade total de sedimentos transportada.

Na segunda parte desta tese, a dinâmica de escoamentos com elevada concentração de sedimentos é estudada. Neste trabalho, executa-se a aplicação de um modelo de primeira ordem de roll waves para fluidos de reologia Herschel-Bulkley para simular um evento natural registrado na literatura. Os resultados apresentados mostram que roll waves poderiam, de fato, ser identificadas no evento e que a amplitude média observada poderia ter sido estimada com 8% de incerteza. Assim, um modelo mais complexo para a solução do perfil de velocidade é proposto, adicionando a porosidade do solo ao problema. Resultados do modelo são comparados com simulações numéricas. Uma análise paramétrica é efetuada e o caso de estudo é novamente avaliado.

Como conclusão geral do trabalho, a presença de fenômenos não-estacionários durante a evolução escoamento superficial — corrida de lama afeta a dinâmica global do sistema acoplado hidráulica-transporte de sedimentos, quando comparado ao caso permanente e uniforme. Assim, a verificação de que tais fenômenos podem aparecer deve constituir parte de projetos engenharia, especial-

mente quando estes, em situações de catástrofes, envolvem danos a infraestruturas civis e quase sempre perdas de vidas, como é o caso das corridas de lama.

Des écoulements instationnaires à surface libre: contribution aux études du transport instationnaire de sédiments en écoulement ruisselant et des instabilités de coulées de boue non-newtonienne

Aperçu général

Chapitre 1 - Les écoulements naturels et les risques associés

Les catastrophes naturelles peuvent être décrites comme le résultat de l'interaction défavorable entre un événement naturel et une communauté vulnérable. Elles sont le résultats de la convolution des paramètres météorologique, géologique/géomorphologie et anthropique. Cette thèse, financée par le gouvernement brésilien, se situe dans ce contexte général lié aux risques naturels. Dans les dernières années, le Brésil a été l'hôte de nombreux événements naturels tels que des inondations et des glissements de terrain (Pinho et al., 2013). A la saison des pluies, entre les mois de décembre et de février, la région de la *Serra do Mar*, une région montagneuse à forte déclivité appartenant aux départements du Sud-Ouest brésilien, a subi un type d'événement naturel qui est souvent la cause de catastrophe: les coulées de boue. Les catastrophes qui y ont eu lieu sont considéré par le gouvernement brésilien comme les plus grandes qu'est subi le pays. A titre d'exemple, nous faisons appel aux événements de la région cotière du département de Rio de Janeiro en 2011 (Guidugli et al., 2012) et de São Paulo (voir Figure 1.1). Dans cette thèse, des aspects de ce type de phénomène sont étudiés.

Les coulées de boue peuvent avoir différentes évolutions, mais deux mécanismes principaux sont mis en avant:

- déstabilisation de la pente saturé d'eau, et liquéfaction abrupte du sol, ce qui forme un front de masse à haut débit fluide;
- incorporation graduelle de matière sédimentaire au sein de l'écoulement, qui peut, selon la géométrie, augmenter dû à l'union des affluents, jusqu'à ce que le fluide devienne très chargé en sédiments.

Dans le cadre de cette thèse, nous nous intéressons au deuxième cas, que nous appelons *les coulées de boue graduellement développées*. Ce type d'évolution d'un événement peut alors être décrit par quatre étapes (voir Figure 1.2):

I précipitations de forte intensité sur la topographie escarpée. La saturation rapide du sol conduit au ruissellement sur la zone;

II le ruissellement sur les régions concaves du bassin érode peu à peu le sol, produit des ravines, et transporte de la matière sédimentaire vers l'aval et les affluents plus importants;

III quelque part, les ruissellements aboutissent un débit intermédiaire important capable d'éroder de plus en plus de sédiments;

IV très en aval, au pieds de la montagne, les affluents se rejoignent et constituent un écoulements très chargé en sédiments qui peut être désormais appelé coulée de boue.

D'après les théories de la mécanique des fluides, les ruissellements compris dans les étapes II et III peuvent être étudiés comme des écoulements turbulent d'eau claire avec transport de sédiments. Le problème primordial dans ce cas est de connaître la quantité de sédiments transporté par l'écoulement. Cette mesure indiquerait la vitesse auquel le processus

d'évolution se passerait (graduelle augmentation de l'entrainement de sédiments), et à quel moment l'étape IV serait aboutie. Cependant, la prédiction de cette quantité est toujours un sujet actuel dans la recherche scientifique. En d'autres termes, le transport de sédiments n'est pas encore un phénomène totalement dévoilé. Étant donné la nature turbulente de ces écoulements, plusieurs source de non-stationnarité peuvent être présentes. Ces instabilités et leur effets induisent des incertitudes sur les modèles de masse solide transportée.

Parallèlement, l'étape IV est caractérisée par un écoulement plus dense, où les propriétés visqueuse du fluide diverge de celles de l'eau. Sur la configuration de coulée de boue, l'écoulement est normalement laminaire et son évolution peut être établi d'après des lois du mouvement plus simples. Par contre, le problème qui se pose est de connaître les propriétés de la mixture eau-sédiments, un problème fortement étudié dans la littérature (Coussot, 1994; Ancey, 2007). Par ailleurs, certains types d'instabilités de surface libre peuvent apparaître dans ce cas. La présence d'instabilités au sein de l'écoulement va augmenter la variabilité spatio-temporel de l'événement et ainsi intervenir les modèles de prédiction des caractéristiques hydrauliques tels que les hauteurs de l'écoulement ou ses vitesse.

Cette thèse développe deux études indépendantes, participants à améliorer deux aspects du phénomènes de coulée de boue: une étude expérimentale

du transport sédimentaire d'écoulements ruisselants en régime turbulent et présence d'ondes ; et une étude théorique-numérique sur les coulées de boue en régime laminaire instable. Le but est de comprendre comment les phénomènes instationnaires vont intervenir dans l'évolution potentielle coulée de boue.

Chapitre 2 - Cadre théorique général

Les écoulements à surface libre peuvent être modélisés mathématiquement avec les lois de conservation de masse et de quantité de mouvement. Le tenseur de contrainte dans le fluide est adapté en fonction de la concentration en sédiments dans la mixture fluide-sédiments. Par conséquence, la dynamique de l'événement, turbulent ou laminaire, est fortement influencé par les conditions du problème étudié et la capacité de l'écoulement à entraîner des sédiments. Des grandeurs adimensionnelles telles comme le nombre de Reynolds, de Froude et de Shields sont utilisées pour représenter ces dynamiques fluides et sédimentaires.

Le ruissellement (écoulement mince, turbulent, à faible concentration de sédiments) et les coulées de boue (écoulements laminaire à forte concentration de sédiments) peuvent être mis sur le même diagramme ou les paramètres en jeu sont le taux de déformation et la concentration de solide au sein de la mixture (voir Figure 2.2, d'après Coussot and Ancey (1999)). Pourtant, le diagramme ne prévoit pas le passage d'un type d'écoulement à l'autre. L'une des questions initiales à l'origine de cette thèse est l'existence d'un passage/évolution continu entre ces deux régimes. Ce passage semble possible grâce à la pente du chenal. D'après Berzi and Fraccarollo (2013), la distribution vertical (concentration) de sédiments est contrôlée par la déclivité du chenal, paramètre qui joue un important rôle sur la stabilité de l'écoulement. En fonction des caractéristiques géométriques, du débit et du fluide, les écoulements à surface libre peuvent être susceptibles à de développer des phénomènes d'instabilités de surface. Parmi les instabilités possibles, un type particulier est souvent relié aux événements de mouvement de masse: les roll waves. Il s'agit d'un train d'ondes de grandes amplitudes qui se forme lorsque les conditions sont favorables. Ces ondes viennent affecter la dynamique du transport (Davies, 1990; Colombini and Stocchino, 2005; Balmforth and Vakil, 2012) et la bonne prédiction d'un événement indispensable au dimensionnement des ouvrages et à la sécurité des personnes et des biens autour de l'écoulement.

Première Partie - Le transport de sédiments au ruissellement

Chapitre 3 - Introduction

Plusieurs travaux de recherche trouvés dans la littérature montrent que les phénomènes instationnaires ont un effet important sur la dynamique du transport. Les ruptures de barrage (Fraccarollo and Capart, 2002), l'imminence du transport (Ancey et al., 2006), les structures du lit mobile (Colombini and Stocchino, 2005) et les ondes de surface libre (Kranenburg et al., 2013) sont quelques exemples de phénomènes variables dans le temps et dans l'espace qui sont déterminants. Pour étudier ces problèmes, l'approche expérimentale constitue un outil puissant, capable de donner des indices utiles à la compréhension des phénomènes physiques. Les mesures nécessaires pour développer l'étude du transport instationnaire de sédiments doivent être capables de donner des informations temporelles à la fois sur l'écoulement et sur transport lui-même, à l'échelle du ruissellement. Une estimation rapide de ces échelles du problème permet de comprendre les enjeux techniques de l'exécution de ce travail (Amir et al., 2014).

Chapitre 4 - La méthode expérimentale

Un banc de ruissellement a été conçu et construit lors de ce thèse. Ce banc permet la génération des écoulement ruisselants et la mesure de ses propriétés (hauteur d'eau, débit massique). Le chenal a une section rectangulaire et un fond rugueux fixe où l'écoulement turbulent se développe et atteint un régime uniforme. A la fin de ce fond fixe, un lit mobile est installé, où le sédiment-test est disposé. L'écoulement turbulent établi arrive ainsi au lit mobile et transporte les grains vers l'aval, où un piège est placé. Ce piège permet la capture des grains et leur visualisation de manière à quantifier le transport.

Les mesures plus fines des propriétés de l'écoulement et du transport solide sont faites à l'aide des techniques d'imagerie. Un système de velocimétrie à partir des images de traceurs (*Particle Image Velocimetry* — PIV) permet l'obtention des caractéristiques de l'écoulement et la validation de ses propriétés turbulentes. Un système de suivi de particules (*Particle Tracking Velocimetry* — PTV) au niveau du piège horizontal fournit les informations de débit solide au cours du temps. Le système PTV a été conçu en prenant comme base les expériences rapportés dans la littérature par Frey et al. (2003). La méthodologie PTV permet obtenir la vitesse des

particules piégées et ainsi le débit solide (voir équation 4.20 et 4.24). Pour étudier les écoulements perturbés (écoulements où il y a le passage d'ondes de surface libre), un système de batteur a été installé en amont du chenal, il permet la génération de perturbation à des fréquences contrôlées. Une analyse des résultats de la méthode est présentée pour valider la qualité des résultats obtenus. L'influence des propriétés des grains, de la qualité des images et du signal obtenu sont évalués.

Chapitre 5 - Mesures sur le transport instationnaires de sédiments

Une série de résultats expérimentaux est présentée où les caractéristiques du transport solide sont mise en avance. Trois études principales sont menées: le débit moyen en fonction du nombre de Shields; les distributions spectrales de puissance des signaux; l'intensité des fluctuations du transport solide.

Tout d'abord nous étudions les résultats obtenus dans le cas d'un écoulement pas perturbé. L'analyse sur les propriétés moyennes montrent que les mesures sont en accord avec des lois empiriques classiques de la littérature (Meyer-Peter and Müller, 1948; Wong and Parker, 2006) (voir Figure 5.10). Une analyse des densités spectrales de puissance (PSD) permet trouver de mettre en évidence la sensibilité du transport aux propriétés de l'écoulement proche de la paroi. Pour les écoulements proches du seuil de mise en mouvement ($\mathrm{Sh} < 2.5\mathrm{Sh}_c$), on aperçoit une loi de décroissance des PSD à la puissance -1 avec la fréquence. Ce résultat serait en concordance avec d'autres de la littérature qui prévoyaient que le transport par charriage est contrôlé par les structures turbulentes proches de la paroi (qui ont cette même loi de décroissance -1). En revanche, la loi de décroissance passe à la puissance $-5/3$ pour les écoulements à nombres de Shields plus forts pour lesquels les perturbations tridimensionnelles du lit mobile sont plus fortes (voir Figures 5.14 et 5.15). Même si le transport solide se fait par charriage, ces résultats montrent que, lors de la présence des structures morphologiques du lit, la dynamique turbulente contrôle les fluctuations du transport solide.

L'intensité des fluctuations du transport solide montrent le même type de loi empirique que celle utilisée pour le débit solide moyen quand on les relie aux intensités de fluctuations de la vitesse de frottement. La dernière analyse portée sur les fluctuations de débit solide, illustré par la figure 5.11, permet de conclure que loin du seuil de mise en transport ($\mathrm{Sh} > 4\mathrm{Sh}_c$), le niveau de fluctuations est à peu près constant et suis les propriétés de

l'écoulement moyen.

A l'aide du batteur placé en amont, une perturbation de la surface libre est générée et les mesures sont analysés de la même façon que pour l'écoulement pas perturbé. L'analyse de la quantité moyenne de masse transportée indique qu'il y a une diminution de la capacité de transport de l'écoulement (Figure 5.16). Pour un nombre de Shields donné, l'écoulement perturbé a un débit solide moyen moins important que l'écoulement stationnaire non perturbé. Nous discutons les possibles causes de ce phénomène en s'appuyant sur résultats dans la littérature pour le profil de frottement d'un écoulement avec la presence des instabilités de surface libre type roll waves. Nous montrons le frottement moyen lors du passage d'une onde décroit et est plus faible que ce de l'écoulement moyen. Les densités spectrales de puissance ne présentent aucun changement significatif par rapport aux intensités et aux loi de décroissance trouvées pour l'écoulement pas perturbé. Elles corroborent les résultats précédents. De la même que ce dernier, les fluctuations de transport solide gardent ses caractéristiques, en suivant les fluctuations de vitesse de l'écoulement.

Deuxième Partie - Les écoulements non-Newtoniens sur un sol naturel

Chapitre 6 - Introduction

Dans cette deuxième partie de la thèse, un travail d'ingénierie est initialement engagé pour appliquer un modèle mathématique à la prévision d'un événement naturel. On se servira d'un modèle constitué préalablement (Maciel et al., 2013) pour estimer les caractéristiques des ondes de surface libre type *roll waves* au sein d'un écoulement boueux (mixture eau et sédiments) de propriétés non-Newtoniennes type Herschel-Bulkley. Une étude de cas est faite à partir d'un événement mesuré et décrit dans la littérature par Berti et al. (1999, 2000).

Chapitre 7 - Application d'un modèle mathématique à un événements naturel: l'étude de cas de Acquabona

Dans ce chapitre, le modèle pris en considération est brièvement décrit. Dans ce modèle, les équations de conservations sont manipulés en prenant le modèle rhéologique Herschel-Bulkley pour le fluide. Les principaux paramètres

caractéristiques de l'écoulement sont rappelés comme, par exemple, la vitesse moyenne, la vitesse superficielle et la hauteur de plug. La méthodologie d'utilisation du modèle est systématiquement présentée (voir figure 7.1). Une étape importante consiste à vérifier que l'écoulement respecte quelques conditions: le régime doit être laminaire; les hypothèses d'eau peu profonde doivent être applicables; l'écoulement doit être instable. L'obtention des paramètres d'entrées est l'une des tâches les plus importantes. Vu qu'il s'agit d'un modèle laminaire, les caractéristiques du fluide vont avoir une importance cruciale sur les résultats. Le site d'Acquabona est décrit en mettant l'accent sur les propriétés qui seront décisives pour la bonne obtention des paramètres d'entrée.

Une fois les paramètres d'entrée estimés, les instabilités de surface libre sont simulées et comparées avec les résultats présentés par Berti et al. (2000). La sensibilité aux propriétés rhéologiques est évalué. Comme les ondes mesurées par les auteurs représentent un phénomène naturel et que le modèle mathématique correspond aux propriétés d'une onde en régime permanent et uniforme, une comparaison directe n'est pas possible. Ceci dit, l'amplitude moyenne des ondes mesurées est comparée au modèle, ce qui donne une différence de valeurs de 8%. Ce résultat montre une robustesse du modèle à prévoir une valeur caractéristique de l'événement naturel. Dernièrement, un diagramme a été produit (voir Figure 7.7) pour expliciter l'importance de considérer un modèle mathématique pour la prévision d'un tel événement naturel de mouvement de masse.

Chapitre 8 - La recherche d'un modèle plus complexe

Après avoir vérifié la qualité des résultats d'un modèle établi dans la littérature, nous avons poursuit la recherche d'un modèle mathématique plus complexe. Cela nous a mené à intégrer l'effet de la porosité dans le problème, étant donné que la solution mathématique d'un écoulement à surface libre d'un fluide non-newtonien type Herschel-Bulkley sur un fond poreux n'était pas encore complètement définie.

Le modèle proposé par Beavers and Joseph (1967) pour un fluide newtonien est utilisé comme base. Grâce au travail de Chevalier et al. (2013), les conditions limites pour l'écoulement d'un fluide type Herschel-Bulkley dans un milieu poreux ont pû être mieux comprises. D'autres études comme celles de Chhabra et al. (2001), Rao and Mishra (2004) et Pascal (2006) pour les fluides qui présentent des lois rhéologiques de type loi de puissance ont permis d'adapter les conditions limites exigées par le problème. Dans

ce cadre, le modèle mathématique est développé et détaillé. La solution analytique pour le problème posé est ainsi donnée. Le profil de vitesse, donné par l'équation 8.17, vérifie les solutions obtenues auparavant pour les fluides de rhéologie moins complexes.

Chapitre 9 - Simulations numérique

Pour valider la solution analytique obtenue, des simulations numériques sur FLUENT ont été faites. Les simulations ont respecté la configuration géométrique utilisée par Prinos et al. (2003) et Chan et al. (2007). Les fluides test utilisés avaient des propriétés réels qui reproduisaient les mixtures de Carbopol utilisés expérimentalement par Roberts and Barnes (2001) et Leite (2009) (voir tableaux 9.2).

Les résultats obtenus numériquement montrent que la vitesse dans le milieux poreux est du même ordre de grandeur que celle prévue par le modèle. En ce qui concerne la solution du profil de vitesse de l'écoulement au-dessus du fond, le modèle mathématique est capable de reproduire les valeurs caractéristique de vitesse de plug ($u(z = z_0)$) et de vitesse au fond ($u(z = 0)$) avec un écart faible de 1 et 5%, respectivement. Des analyses mathématiques faites à posteriori illustrent les effets du paramètre de porosité sur la solution, ainsi que l'effet combiné entre la porosité et les propriétés rhéologique du matériau.

Chapitre 10 - Retour à l'étude de cas d'Acquabona

Finalement, après avoir étudier comment la porosité peut modifier l'écoulement, l'étude de cas d'Acquabona est à nouveau traité. Les paramètres de porosité sont assumés à des valeurs classiques et la courbe $h_0 \,\mathrm{X}\, q_0$ est complétée. Vis-à-vis des effets de porosité assez faible pour le cas d'Acquabona, les résultats montrent une légère différence, qui serait négligeable si l'on considère les incertitudes des paramètres d'entrée du modèle.

Chapitre 11 - Discussions et Conclusions

Ce chapitre apporte des discussions sur les résultats obtenus dans le cadre de cette thèse dans les deux configurations : érosion par ruissellement et instabilité de coulée de boue.

Dans le cas du ruissellement, la validité de la méthodologie employée a été discutée. Les résultats expérimentaux obtenus en régime permanent et

uniforme ont démontré la capacité de la méthodologie à estimer les fluctuations du transport solide lors d'un écoulement ruisselant. Les résultats lors d'un régime instationnaire ont montré que la présence des instabilités de surface libre modifie le transport solide : la quantité moyenne des sédiments transportés à l'échelle du temps étudiée est inférieure à celle correspondant à un lit de sédiment plat.

Dans le cas des coulée de boue, l'utilisation d'un modèle simplifié pour la prédiction des propriétés d'un événement naturel type coulée de boue a été détaillée. La méthodologie utilisée a permis la vérification de la présence des instabilités type roll wave lors d'un événement réel rapporté dans la littérature. Ce modèle théorique a mené à l'estimation de quelques propriétés de l'événement en question, ce qui a démontré la capacité du modèle à prévoir ce type d'événement naturel et à améliorer la prévention du risque. En outre, un modèle mathématique plus complexe prenant en compte la perméabilité du fond a été proposé et analysé dans la perspective de mieux représenter ce type d'événement.

Pour conclure, les instabilités hydrauliques doivent être considérées lors de la modélisation d'un événement naturel potentiellement dangereux afin de mieux prédire et estimer les caractéristiques physiques de cet événement.

Chapitre 12 - Perspectives

Si les résultats et discussions présentées dans ce travail contribue à une meilleur compréhension et modélisation de l'influence des phénomènes transitoires dans des événements naturels de type coulée de boue, ils ne permettent pas une modélisation complète et ce dernier chapitre apporte quelques suggestions de prolongement du travail réalisé du point de vue expérimental, théorique et numérique.

D'un point de vue expérimental, par rapport au ruissellement, les résultats obtenus peuvent être exploités selon une approche statistique. D'après Heyman (2014), chaque passage de particule correspond à un événement. Lors d'un essai, l'ensemble des événements peut ainsi être analysé pour décrire le comportement moyen et fluctuant du transport de sédiments.

En ce qui concerne les approches utilisées pour la coulée de boue, la perspective initiale est de valider le modèle théorique de roll waves employé pour d'autres événements réels de la littérature. Cela montrerait la capacité et la robustesse du modèle. Pour la suite, le modèle mathématique peut être modifié pour prendre en compte d'autres effets comme la turbulence et la porosité. Ce dernier a été étudié dans ce thèse dans le chapitre 8. Toutefois, on propose la simulation numérique pour différentes géométrie afin de de

valider la solution analytique proposée pour un écoulement non-newtonien sur un fond poreux et la conditions limite employée.

List of Figures

1.1 Photos from Brazilian largest natural hazards. 4
1.2 Illustration of process for gradually developed mudflow event. 7

2.1 Schematic representation of a three-dimensional open-channel flow and the geometrical characteristics of interest in such problems. 14
2.2 Simplified diagram of flow regimes from Coussot and Ancey (1999) using shear rate $\dot{\gamma}$ and particle concentration in mixture ϕ_v. The transitions between regimes are described using dimensionless numbers. For details of such numbers, see Coussot and Ancey (1999). . . . 15
2.3 Schematics representation of gradually developed mudflow. Increase in flow height represent discharge income. Gray shade represent high concentration of sediments in fluid mixture. 17
2.4 Classification of mass movements on steep slopes as a function of solid fraction and material type. From Coussot and Meunier (1996). 17
2.5 Examples of runoff flows in different environments. 2.5(a): runoff on paved street; 2.5(b): runoff on mountain region; 2.5(c): runoff in vegetable area; 2.5(d): runoff occurring on agriculture zone. 19
2.6 Law of the wall as presented by Von Kármán (1930). Blue lines represent viscous dominant and log law behavior. Black dots reproduce a typical velocity profile. 21
2.7 Critical Shields number against dimensionless grain diameter as presented by 2.7(a), van Rijn (1984) referencing the work of Shields (1936); and 2.7(b) more recent work from Paphitis (2001). 22
2.8 Schematic representation of open-channel flow in presence of a mobile bed. 23
2.9 Experimental and theoretical degree of saturation as a function of the bed slope for plastic particles in water. In the up-right corner, sketch of the flow configuration with the frame of reference and a generic concentration profile (Berzi and Fraccarollo, 2013). The degree of saturation is the ratio between mean flow height and maximum height of transported particles jumps. For such ratio equals to 1, particles trajectories cover all position in the flow height. 26

2.10 Examples of non-Newtonian fluid flows in different environments. 2.10(a): mud dam-break event of Mariana district, Minas Gerais state, Brazil, 5th November 2015; 2.10(b): lahar flow from late November 1985 in Río Lagunillas, former location of Armero, Colombia; 2.10(c): concrete been poured; 2.10(d): drilling mud used in oil industry; 2.10(e): cornstarch mixture subdue to stress from speaker vibration. 27

2.11 Schematic representation of flow. The gray color indicates that particles concentration are high in the mixture. 29

2.12 Examples of free surface instabilities in natural flows. 2.12(a): sea wave breaking when approximating the shore; 2.12(b): tidal bore at Vayres, Gironde, photo from Jacques Dassie personal website; 2.12(c): roll waves on clean water turbulent flow at Turner reservoir, San Diego County, California, on February 24, 2005, from personal website of Victor Miguel Ponce; 2.12(d): free-surface instabilities in a complex non-Newtonian fluid (Chanson et al., 2006). 30

2.13 Open-channel flow when in presence of surface instabilities. wave properties are highlighted. 31

2.14 From Richard and Gavrilyuk (2012). Comparison of the theoretical solution to the model proposed by the authors (line) and Brock's (Brock, 1967) experimental results (dots) for two different test cases. On the horizontal axis, dimensionless Lagragean longitudinal coordinate scale to the wavelength. On the vertical axis, wave profile scale to mean flow height. 34

2.15 From Ng and Mei (1994). Dimensionless profiles for roll waves solution (free surface height, mean flow velocity and bottom shear stress) for a constant index flow value $n = 0.4$ and different Froude number. . . . 35

2.16 The stability criteria found by Maciel et al. (2013) for different values of flow index (represented by lines). Symbols represent experimental results from Coussot (1994): crosses represent flows where no roll waves were noticed, whereas triangles show very likely roll waves configuration at the free surface of flow. 37

3.1 Experimental images from Fraccarollo and Capart (2002) which shows dam-break event advancing over mobile bed. The strong non-linear event properties subject a discontinuous profile of sediment transport. 42

3.2 Example of discontinuous transport and anomalous diffusion of mass due to non-constant stress applied. Sediment transport can only happen if flow applies enough stress to overcome particle submerged weight, represented by a threshold velocity u_c. Turbulent fluctuations can interfere with continuous state of transport when mean flow is close to particles threshold velocity. 43

3.3 Examples from scientific researches that indicate possibles effects between roll waves instabilities and sediment transport. 3.3(a): Picture from Davies (1990) illustrating how roll waves and sediment waves interact; 3.3(b): stability plot showing that anti-dunes instabilities from mobile bed can appear together with roll waves flow instability (Colombini and Stocchino, 2005). 44
3.4 Sketch of open-channel flow configuration over mobile bed. Dark line represent free surface in steady and uniform conditions. Dashed line represent free surface instabilities propagating downstream. 45

4.1 4.1(a): Sketch of experimental setup, dimensions not to scale; 4.1(b): top view from the experiment. 50
4.2 Algorithm to obtain flow measurements from contact needle (CN - global) and PIV system (PIV - local). 50
4.3 Principle of Particle Image Velocimetry (PIV) technique functioning. A double-pulsed laser sheet crosses a ROI of the flow, which then is recorded through high-speed camera. The pair of image is used to calculate the displacement of seeding particles in the flow, and respective velocity. Their velocity is assumed equals to flow velocity. (DANTEC Dynamics) 52
4.4 Histogram for sediment used in experiments. Lines represent cumulative distribution, circles normalized histogram. Gray lines represent brand new glass spheres, dark lines represent used ones. To the right, MEV images for particles showing regularity of shape. 55
4.5 Schematic representation of horizontal trap section. For sake of visualization, illustration represent a longitudinal cut following the trap. . 55
4.6 Raw image of horizontal trap from high-speed camera. 57
4.7 Images from an experimental run. 4.7(a): original image in gray-scale obtained from camera acquisition; 4.7(b) enhanced image; 4.7(c) binary image showing shadows from particles. 58
4.8 Scheme of particle counting inside the ROI. Open circle denotes particles in time step t_{k-1} and black circle denotes particles Δt seconds after, time step $t_k = t_{k-1} + \Delta t$. 59
4.9 Schematics of the side view from the upstream part of the channel where the disturbance system is positioned. 61
4.10 Artificial image created to test PTV methodology for solid discharge calculation. 62
4.11 Artificial sequence type A created to test PTV methodology dependence on ROI size. 62
4.12 Dependency of sediment discharge on vertical length of ROI Δy_{ROI}. 4.12(a): well-behaved artificial run; 4.12(b): experimental runs gb1-3. 63
4.13 Example of solid transport signal from a same experimental run using different ROI. 63

4.14 Comparison between grain-size distribution of sediment particles obtained from laser grain-size distribution and imagery technique. The red line indicates the probability density function obtained from laser grain-size distribution. Black line represents measurements from image technique employed. Yellow circles and purple triangles show different corrections that can be employed to correct particles diameter. 64

4.15 Pictures showing different stages of image processing technique where the artificial increase in diameter is observed. 65

4.16 Solid discharge for experimental run gb2-2 as function of time. Signal is sectioned following the classification described in subsection 4.2.3. . 65

4.17 Cumulative mean solid discharge for experimental run gb2-2 as function of time window. Gray shaded zone indicate uncertainties for cumulative mean in the positive direction of time, and red shaded zone indicate the same property in negative direction of time. 67

4.18 Cumulative mean solid discharge for experimental run gb2-2 sectioned in: 4.18(a) q_s^{III}, between 15 and 25 seconds and 4.18(b) q_s^{IV}, from 2(seconds and forward. 68

4.19 Comparison between different transport rate measurements: q_{s_W} represented the total weighted mass of particles displaced during the experimental run; $q_{s_{PTV}}$ represented the measured solid discharge through PTV method. The dashed line represent the solid discharge limit value where particles quantity can start to affect the solid discharge assertiveness. The solid line indicate the relation between both measured solid discharges under the limit of assertiveness. 69

4.20 Limitations found in the PTV method employed to calculate sediment discharge. Solid arrows illustrate real displacement of particle. Dashed arrow indicate calculated displacement. 69

5.1 Correlation between friction velocity computed through both methods $u_{*\mathrm{CN}}$ and $u_{*\mathrm{PIV}}$. Solid line represent linear relation between both methods for friction velocity calculation. Dashed line represents equality $u_{*\mathrm{PIV}} = u_{*\mathrm{CN}}$. 73

5.2 Averaged vertical velocity profile $\langle\bar{v}\rangle(y)$ compared to PIV system precision e_{PIV} for experimental run gb5. 74

5.3 Results for average profiles of mean flow velocity $\langle\bar{u}\rangle(y)$ and standard deviation $\langle u_{\mathrm{RMS}}\rangle(y)$ for runs gb1 to gb8. See section 5.1. 75

5.4 Turbulent characteristics of average profile of mean flow velocity. Lines indicate theoretical values: solid line is $u^+ = \kappa^{-1}\log y^+ + 5$ for log region; dashed line is $u^+ = y^+$ for viscous layer. 75

5.5 Turbulent intensities for runs gb1 to gb8. Lines indicate computed values following empirical results from Antonia and Krogstad (2001). 5.5(a): longitudinal turbulent intensities u^+_{RMS}; dark line represent run gb1, and gray line, run gb8, following Equation 5.4. 5.5(b): vertical turbulent intensities v^+_{RMS}; dark line represent computed values from Equation 5.5. 76
5.6 Instantaneous fluctuation field (u', v') for experimental run gb5. Shades indicates absolute value for velocity $(\sqrt{u'^2 + v'^2})$; 77
5.7 Correlation between $\langle u \rangle(y_0)$ and $u_{*\mathrm{PIV}}$. 5.7(a): Different possible correlation between $u_{*\mathrm{PIV}}$ and $\langle \bar{u} \rangle(y_0)$.5.7(b): Highlight for $y0 = 0.70$ mm in Dark line represents first-order polynomial Equation 5.6. Dashed lines are 95% confidence boundaries. 78
5.8 Time dependent signal of friction velocity $u_*(t)$ for PIV measurement gb5, using $y_0 = 0.46$. 79
5.9 Power spectral density of $u*F$ for PIV experimental experimental run gb5 for two different flow heights y_0: one close to close $y_0 = 2.25D$ (image to the left); and another far from the bed $y_0 = 9D$ (image to the right). Red line indicates -1 slope; blue line $-5/3$ slope. Re $=$ 5625; Fr $= 0.87$; Sh $= 0.060$. 80
5.10 Empirical relation between Shields number and dimensionless solid discharge. Gray circles represent solid discharge q_s^{III} and gray squares q_s^{IV}. Dark solid lines represent uncertainties of measurement. Horizontal uses upper and lower limit curves from Paphitis (2001) to estimate the uncertainties on $\mathrm{Sh} - \mathrm{Sh}_c$. Purple dashed line represent fit of values from the present work. 82
5.11 Fluctuations intensity of solid transport against Sh. The shaded region indicates the region for high Shields number as indicated by Equation 5.17. The blue solid line represents Equation 5.15 for $u'_{*\mathrm{RMS}}/u_* =$ 19%. Dashed lines uses maximum and minimum for $u'_{*\mathrm{RMS}}/u_*$. 84
5.12 Normalized power spectral density for experimental run gb1-4 (q_s^{III}), with Sh $= 0.079$; Fr $= 1.10$; Ro $= 2.90$. Dotted blue line represents $-5/3$ slope and red line -1 slope. Gray line indicates negligible information. 86
5.13 Normalized power spectral density for experimental runs 5.13(a) gb1-2 (q_s^{III}), with Sh $= 0.068$; Fr $= 1.16$; Ro $= 3.12$; 5.13(a) gb1-2 (q_s^{III}), with Sh $= 0.075$; Fr $= 1.20$; Ro $= 2.99$. Dotted blue line represents $-5/3$ slope and red line -1 slope. Gray line indicates negligible information. Shaded yellow zone highlight possible spectral gap. 87
5.14 Normalized power spectral density for experimental run gb2-2, with Sh $= 0.159$; Fr $= 1.54$; Ro $= 2.05$. 5.14(a): no bedforms captured; 5.14(b); bedforms detected on the signal. Dotted blue line represents $-5/3$ slope and red line -1 slope. Gray line indicates negligible information. Shaded yellow zone highlight possible spectral gap. 88

5.15 Normalized power spectral density for experimental run gb4-1, with Sh = 0.285; Fr = 2.66; Ro = 1.53. Dotted blue line represents −5/3 slope and red line −1 slope. 89

5.16 Results solid discharge for pulsating flows. Dotted lines indicate empirical relation found for solid discharge in steady flow conditions. Dashed line represent fit from disturbed flow conditions. 90

5.17 Fluctuation intensity of velocity field for steady and pulsating flow. Steady flow experiments are represented by black symbols and disturbed flow by gray ones. 91

5.18 Ratio between u_{*F} calculated for disturbed and steady flow conditions for $y_0 = 0.70$ mm. 92

5.19 Results from the mathematical model for laminar roll waves (Maciel et al., 2013; Toniati et al., 2015) for different fluids. 93

5.20 Fluctuations intensity of solid transport for steady and disturbed flow conditions against Sh. The shaded region indicates the region for high Shields number as indicated by Equation 5.17. The blue dotted line represents the undisturbed flow conditions. Red lines (solid and dashed) present Equation 5.15 for values for $u'_{*\mathrm{RMS}}/u_*$ in disturbed conditions. 94

5.21 Normalized power spectral density for experimental runs 5.21(a) gbw5 (q_s^{III}), with Sh = 0.063; Fr = 0.79; Ro = 3.24; 5.21(b) gbw2 (q_s^{IV}), with Sh = 0.198; Fr = 1.60; Ro = 1.83; and 5.21(c) gbw4 (q_s^{IV}), with Sh = 0.399; Fr = 2.34; Ro = 1.29. Dotted blue line represents −5/3 slope and red line −1 slope. 95

6.1 Conceptual rheological classification of mass movements as a function of fine content and solid fraction. The exact limits between the different parts of the diagram should be determined for each material and may slightly vary with flow characteristics. (From Coussot (1992). . . . 101

7.1 Diagram showing methodology employed for roll waves model application Maciel et al. (2013). To the left, parameters gathering finds through iterative solution of constitutive equations the proper set of input parameters whenever necessary. To the right, roll waves model verifies flow regime and stability condition and gives the solution of roll waves as well as wave properties. 104

7.2 Schematics on roll waves properties for permanent flow. Dashed line represent based flow with properties h_0 and u_0, where u_∞ is flow freestream velocity. Solid line represent the same flow when roll waves are present and its main properties: wavelength λ_w, wave celerity c and amplitude Δh. 104

7.3 From Genevois et al. (2000). 7.3(a): Location of Acquabona monitoring site. 7.3(b): Grain size distribution envelopes of Acquabona debris flows mixture composition; a - region 1, source area and upstream marls flow channel; b - region 2, downstream marls flow channel; c - region 3, deposition area. 108
7.4 Measurements from station 3, downstream channel, collected through ultrasonic equipment on August 17th, 1998, related by Berti et al. (2000). Highlighted wave train identified as possible roll wave formation. 110
7.5 Influence of rheological properties on waves amplitudes Δh normalized by expected wave amplitude $\Delta h_e = 1.05$ m. The star indicates properties chosen for expected roll waves prediction. 114
7.6 Influence of yield stress τ_0 on waves profiles $h(t)$. Profiles are scaled to each mean flow height h_0 and showed as function of dimensionless longitudinal coordinate ξ. 115
7.7 Mean flow height h_0 as function of the specific discharge q_0 for different friction laws. Curves represent different frictions laws. Shaded zone shows amplitudes of roll waves for the respective friction law. q_{acqua} represents specific discharge in the Acquabona creek for the event here studied based on Equation 7.11. q_{min} is the minimum specific discharge required for roll waves to appear in Acquabona creek given the non-Newtonian rheology. Vertical bar indicates prediction of mean flow height using cases from Table 7.4, for less and more non-Newtonian fluids. 116

8.1 Schematic representation of flow. The non-Newtonian fluid is now flowing inside the porous bed. 120

9.1 Schematic illustration of computational element of the porous bed. The element repeats its pattern along the total length of computational domain where the bottom impermeable wall is the lower boundary of the domain. 128
9.2 Velocity profile for numerical run Q1I3F3. Impermeable wall is located at $y = 0$. The channel bottom line ($y = h_p$) represent the interface between porous bed and open-channel flow. The plug height ($y = y_0$) identifies limit between sheared and plug zone. 131
9.3 Comparison between numerical results for Darcian velocity $u_{p_{\text{num}}}$ and theoretical scale of the same velocity U_p. Dotted line indicates perfect correlation. Solid line represents interpolation of measured points. . . 132
9.4 Comparison between numerical and theoretical solutions of velocity profile for tests cases Q1I3 and Q1I4. 133
9.5 Velocity profiles for all numerical runs. Velocity $u(y)$ is scaled to mean flow velocity u_0 and vertical coordinate to mean flow height h_0. 133
9.6 Theoretical characteristics velocities u_B and u_{y_0} scaled by numerical results as function of γ parameter. 134

9.7 Verification of boundary condition validity. Dotted line indicate perfect correlation between theory and numerical results. 135

9.8 Analysis of rheological properties and porous medium on flow velocity. 9.8(a): contour of velocity at the interface $U|_{Y=0}$ as function n and γ, for $C^* = 0$; 9.8(b): contour of mean flow velocity $\bar{U}$ as function C^* and γ for different values of n. 137

9.9 Dimensionless comparison of mean flow velocity profile for Herschel-Bulkley open-channel flows over porous bed with the ones over flat fixed beds: contours for $\bar{U}/\bar{U}|_{\gamma=0}$ for different values of C^*, as functions of n and γ. 138

10.1 Mean flow height h_0 as function of the specific discharge q_0 for different friction laws and considering porous bed for non-Newtonian fluid. Curves represent different frictions laws. Shaded zone shows amplitudes of roll waves for the respective friction law. q_{acqua} represents specific discharge in the Acquabona creek for the event here studied based on Equation 7.11. q_{min} is the minimum specific discharge required for roll waves to appear in Acquabona creek given the non-Newtonian rheology. Vertical bar indicates prediction of mean flow height using cases from Table 7.4, for less and more non-Newtonian fluids. 141

10.2 Mean flow velocity u_0 as function of the specific discharge q_0 for different friction laws and considering porous bed for non-Newtonian fluid. Curves represent different frictions laws. Shaded zone shows amplitudes of roll waves for the respective friction law. q_{acqua} represents specific discharge in the Acquabona creek for the event here studied based on Equation 7.11. q_{min} is the minimum specific discharge required for roll waves to appear in Acquabona creek given the non-Newtonian rheology. Vertical bar indicated prediction of mean flow height using cases from Table 7.4, for less and more non-Newtonian fluids. 142

10.3 Ratio between mean flow properties (u_0 and h_0) from flow with and without porous effect as function of γ. 143

10.4 Influence of 10.4(a): form factor χ; and 10.4(b): porosity p, in the relation between velocity ratio ($u_0/u_0|_{\gamma=0}$) and dimensionless of porosity γ. 143

11.1 Energy budget for a turbulent volume of a flow. Total energy of flow $= \bar{E} + \bar{e}$. To the left, mean flow energy from different nature (A) volumetric (gravity in our case); (B) pressure; (C) viscous; (D) turbulence. To the right, fluctuating flow energy and their nature: (b) pressure; (c) viscosity. (d) represents the turbulent diffusion. Dissipation are noted by $\bar{\phi}$ and $\bar{\varphi}$. Δ represent the energy transfer between mean and fluctuating field. Extracted from Chassaing (2000), with authorization from Cépaduès-Editions for this specific thesis. Reproduction not authorized. 151

List of Tables

2.1 Mixture flows simplified classification (Graf and Altinakar, 2000). . . . 25
2.2 Values for Fr_{min} for different combination of channel cross-section and type of friction. Adaptation from Vedernikov (1945); Chow (1959); Ponce (1991). The variables ϑ and φ are coefficients calculated based on rheological properties of fluid; $f(\gamma)$ is a function dependent on the porosity parameter γ (to be described in the Part II of this thesis), that depends itself on the porosity, permeability and other porous medium characteristics. 33

5.1 Data compilation of PIV measurements for experimental tests with fixed bed. 72
5.2 Lookup table for constants of function F used to obtain u_{*F}. 78
5.3 Data summary for all experimental tests with fixed glass beads bed in steady flow conditions. 81
5.4 Data summary for all experimental tests with fixed glass beads bed in disturbed flow conditions. 90

7.1 Waves properties collected from Berti et al. (1999) and flow properties calculated using Maciel et al. (2013) model. *: mean value calculate for column; $^+$: calculated using model, based on mean values. 111
7.2 Input parameters for 1D model simulation for expected wave based on mean value for wave velocity propagation. 112
7.3 Output data from mathematical/numerical simulation from 1D model to respect of Acquabona case-scenario from August 17th, 1998. Results are presented for each wave (from A to E) and for the expected wave based on mean flow properties. 112
7.4 Output data from mathematical/numerical simulation for expected wave when varying rheological properties of mud. The range of rheological properties is in agreement with research from the literature (Ancey et al., 1999; Maciel et al., 1997). 114

9.1 Geometrical characteristics of the porous bed element. 129

9.2 Rheological properties of employed fluids. The fluids were carbopol solutions made in laboratory by Leite (2009) and Roberts and Barnes (2001). 129
9.3 Summary of numerical runs performed. Uniform flow parameters obtained are shown and characteristic dimensionless numbers. Note: experimental runs for different carbopol solutions are represented by: F1, Leite (2009) carbopol solution at 0.13%; F2, Roberts and Barnes (2001), at 0.08%; and F3, Roberts and Barnes (2001) at 0.10%. 130

Greek letters

Symbol	Description	Units
α	Momentum coefficient distribution	-
Δh	Amplitude of free surface instabilities	m
Δt	Discrete time interval between images from PIV/PTV system	m
$\Delta t_{\text{esc}}^{k}$	Mean escape time of particle at time stamp t^k	s
$\Delta \vec{r}_i^{k}$	Displacement of particle$i$ at time stamp t^k	m
$(\Delta x_{ROI}, \Delta y_{\text{ROI}})$	Size of region of interest (PIV/PTV)	m
θ	Channel slope	$^\circ$
γ	Dimensionless porosity parameter	-
$\dot{\gamma}$	Flow shear rate	$^{-1}$
κ	Von Kármán constant	-
λ_w	Wavelength of free surface instabilities	m
μ	Newtonian fluid dynamic viscosity	Pas
μ_B	Bingham fluid plastic viscosity	Pas
μ	Power-law fluid plastic viscosity	Pas^n
ν	Newtonian fluid kinematic viscosity	Pas
ξ	Mobile longitudinal coordinate for roll-wave equations	-
ρ	Fluid density	kgm^{-3}
ρ_s	Solid particles density	kgm^{-3}
σ_{ij}	Components of the stress tensor	Pa
τ_0	Fluid yield stress	Pa
τ_b	Bottom shear stress	Pa
τ_{ij}	Components of viscous stress tensor	Pa
ϕ_m	Concentration in mass of sediment particles in mixture	%
ϕ_v	Volumetric concentration of sediment particles in mixture	%
χ	Porous medium form factor	-

Symbol	Description	Units
c	Free-surface waves propagation velocity	ms^{-1}
C^*	Dimensionless yield stress	-
D	Solid particles diameter	m
D_*	Dimensionless solid particles diameter	-
f_w	Frequency of free-surface instabilities	Hz

f_s	Acquisition frequency (PIV an PTV measures)	Hz
F_i	Generic body forces components	m^{-2}
Fr	Froude number	-
Fr_{min}	Minimum Froude number for roll waves generation	-
g_i	Gravity acceleration components	ms^{-2}
h	Free surface height	m
h_0	Mean flow height	m
k_I, k_K	Permeability coefficients for non-Newtonian fluids	m, m^{n+1}
K_n	Consistency index	Pas^n
l_0	Channel width	m
l_t	Horizontal trap width	m
L_0	Channel length	m
L_t	Horizontal trap length	m
m_i^k	Mass of particle$i$ at time stamp t^k	kg
$M(t^k)$	Total mass of particles at time stamp t^k	kg
n	Flow index for non-Newtonian fluids	-
p	Bed porosity	-
P	Fluid flow pressure	Pa
q	Flow specific discharge	m^2s^{-1}
Q	Flow discharge	m^3s^{-1}
q_*	Dimensionless solid particles specific discharge	-
q_s	Solid particles specific discharge	$kgm^{-1}s^{-1}$
Q_s	Solid particles discharge	kgs^{-1}
$\vec{r}_i^k$	Position particle$i$ at time stamp t^k	m
R_h	Hydraulic radius	m
R^2	Coefficient of determination in data fit	-
Re	Reynolds number	-
s	Density ratio ρ_s/ρ	-
Sh	Shields number	-
Sh_c	Critical Shields number	-
u_*	Friction velocity	ms^{-1}
u_{*c}	Critical friction velocity	ms^{-1}
u_∞	Free surface flow velocity	ms^{-1}
u_B	Bottom flow velocity or slip velocity $u_B = u(y = 0)$	ms^{-1}
u_i	Velocity field components ((u, v, w) for $i = 1 : 3$)	ms^{-1}
(u_s, v_s)	Particles velocity	ms^{-1}
t	Time variable	s
t^k	Discrete time stamp at image k from PTV measures	s
T_w	Period of free-sruface instabilities	s
x_i	Spatial coordinates ((x, y, z) for $i = 1 : 3$)	m
y_0	Plug height in non-Newtonian flows	m

Notation

Symbol	Description
e_X	Uncertainties of measurement X
X'	Fluctuating variable
X^+	Variable scaled to wall coordinates
X_{CN}	Property/measure based on contact needle system
X_{PIV}	Property/measure based on PIV system
X_{PTV}	Property/measure based on PTV system
X_{RMS}	Root-mean square of variable
X_{W}	Property/measure based on weighting
X_{p}	Property/measure in/of porous medium
$\bar{X}$	Time-average of variable
$\langle X \rangle$	Spatial-average of variable to respect of longitudinal coordinate x

General overview

Chapter 1

Natural flows and risks

Debris flows (also referred to as mudslides, mudflows, or debris avalanches) generally occur during intense rainfall on water saturated soil. They usually start on steep hillsides as soil slumps or slides that liquefy and accelerate to speeds as great as 35 miles (56 km) per hour. Multiple debris flows that start high in canyons commonly funnel into channels. There, they merge, gain volume, and travel long distances from their source.

United States Geological Survey Fact Sheet FS-071-00
May 2000

1.1 Introduction

Natural hazards, generally speaking, can be described as the result from the interaction between natural phenomena and vulnerable human societies. They are the convolution of meteorological, geological/geomorphological effects with anthropic actions leading to damages perceived by society. They emerge as worldwide events, result as the interaction between many factors such as global warming, landscape usage and misguided urban management, which happens to affect every part of the globe (Burton, 2005). More specifically, in Brazil, people have confronted successive natural events such as floods and landslides year after year during the rainy season (Pinho et al., 2013). In South and Southeast regions, another kind of mass movement event also takes place: mudflows. It usually happens during the rainy season and over *Serra do Mar*, the mountain range that extends along the shore (Guidicini and Nieble, 1984). According to Brazilian Ministry of Science and Technology, landslides and mudflows are the greatest cause of death

among all Brazilian natural hazards.

As matter of meteorological phenomena, on the Southeast Region of Brazil, a particular one takes place during the warm season called South Atlantic Convergence Zone - SACZ (*Zona de Convergência do Atlântico Sul*), which is often responsible for hazardous events in the country. It appears mostly late spring and during summer and is responsible for high precipitation levels, around 200 mm in a couple of hours. This phenomenon is represented by a local maximum level in cloudiness and precipitation across an elongated axis oriented in a Northwest-Southeast manner over South Amazônia, Southeast and West-Center Brazilian regions reaching the Atlantic Ocean.

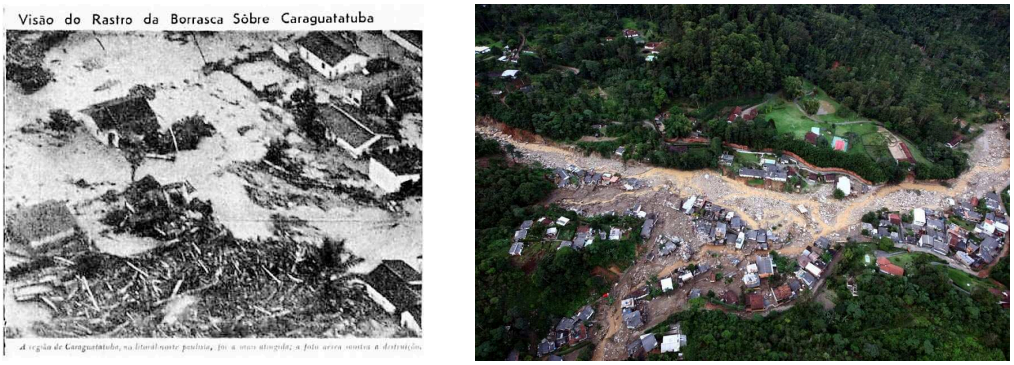

(a) Caraguatatuba, 1967. (b) Teresópolis, 2011.

Figure 1.1: Photos from Brazilian largest natural hazards.

The topography of the region affected by SACZ helps maintaining the strength of the event, mainly on the Southeast region where a mountains range called *Serra do Mar* blocks the passage of clouds. Exactly in this region we find the Rio de Janeiro's state mountain region where a massive hazard took place in 2011. Heavy rains (200 to 300 mm in just few hours) considerably reduced cohesiveness of the thin layer of soil, allowing an enormous volume of muddy material to flow down the hills and devastate areas downstream. Clearly, the mis-occupation and anthropic action were important factors for the dramatic consequences. According to statement released by Civil Defense of Rio de Janeiro State, on January 28th, 8.777 homeless, more than 20 thousand dislodged, 950 dead and 430 missing people were estimated (Guidugli et al., 2012). This last event is now considered as the largest Brazilian natural hazard since the event of Caraguatatuba city, in

March 1967. At that time, São Paulo state northern coast faced a long rainy period; rivers overflowed and were strong enough to drag trees and civil constructions in flooded zones; mud and rocks fell down the hills on successive landslides burying entire houses. The event resulted in great financial losses and death of 500 people (Rebello et al., 2012), thus pointing out the importance of researching such matter in order to avoid such disastrous consequences from happening again. Both events are shown on Figure 1.1. Correctly developing models and predicting evolution of such events might help stakeholders to better estimate risks and find more arguments to develop more efficient policies.

Mudflows are mass movement events that are triggered by intense rainfall and usually start in the upper part of mountains where slopes are stronger. One important feature from flowing fluid is that it is basically composed by water with high concentration of sediments (thus different viscous properties). The source material that constitute the flowing material comes from the soil, basically sediment from different origins (silt, clay and sand in different concentrations). The mixture have then high density which combined with strong slopes, leads to an extremely rapid flow with high kinetic energy and considerable high velocity (mean velocity 5 m/s (18 km/h), up to 10 m/s (36 km/h) (Hungr et al., 2001)).

As far as it is known, gravity-driven mass movement are far to be completely understood by scientific community. The knowledge of such kind of flow is clearly necessary to enhance prevention tools for Engineering when applied to modeling natural events such as mudflows, mud floods and debris flow. Two main scenarios for mudflows generation can be described (Oliveira and Brito, 1998; Chambon et al., 2010):

- sudden fluidification of saturated soil after complete fail of slopes, leading to a massive discharge of solid material at once;
- gradual incorporation of soil into tributaries from the watershed, from upstream to downstream the basin, which can join greater streams and increase in discharge and erosion, thus gradually leading to a stream of muddy material.

The first, which we should call here *suddenly developed mudflow*, can be analogously compared to a dam-break event in which a fluid is suddenly released and moves rapidly downstream. The second, *gradually developed mudflow* have a slower evolution, maturing along the watershed, incorporating sediment material and changing its dynamics. In this work, the second

scenario is explored. As a hydro-geological process, three main features can be identified in the study of mudflows formation:

- rainfall duration and intensity;
- soil characteristics;
- topography.

Rainfall is the triggering mechanism for mass movements such as mudflows, lahar flows, and landslides. For landslides, for example, a stable soil layer saturates with water during a rainy event, acquiring a certain level of fluidity. Eventually, if the fluidity level is high enough, the soil will fail and move. This kind of event could be present during a suddenly developed mudflow, contributing to the increase in sediment concentration in the flow. Rainfall also relates to runoff discharge, directly related to flow capacity of transporting sediments in soil. For such scenario, there is an increase in *momentum*, therefore kinetic energy, related to the flow which is established over a saturated soil, as verified by Iverson et al. (2011). In any case, natural vegetation cover and land use (arable fields, pastures, soil sealing, etc.) also affect flow friction laws, becoming a great issue in regions without proper sustainable environmental management.

1.2 Phenomenological description

The gradually developed mudflow event scenario can be separated in four main stages:

I high intensity rainfall over a steep topography. Increased water absorption by soil and fast saturation of it leads rapidly to runoff;

II initial runoff is established in concave areas from the watershed and erodes its way down in gullies, transporting fine materials downstream, reaching greater tributaries;

III intermediary runoff continuously erode the soil, increasing in solid concentration and discharge, forming sometimes ravines and/or creeks;

IV rainfall peak is reached and the result of the unification of tributaries forms of a main stream with increased discharge and high sediment concentration, achieving the status of mudflow.

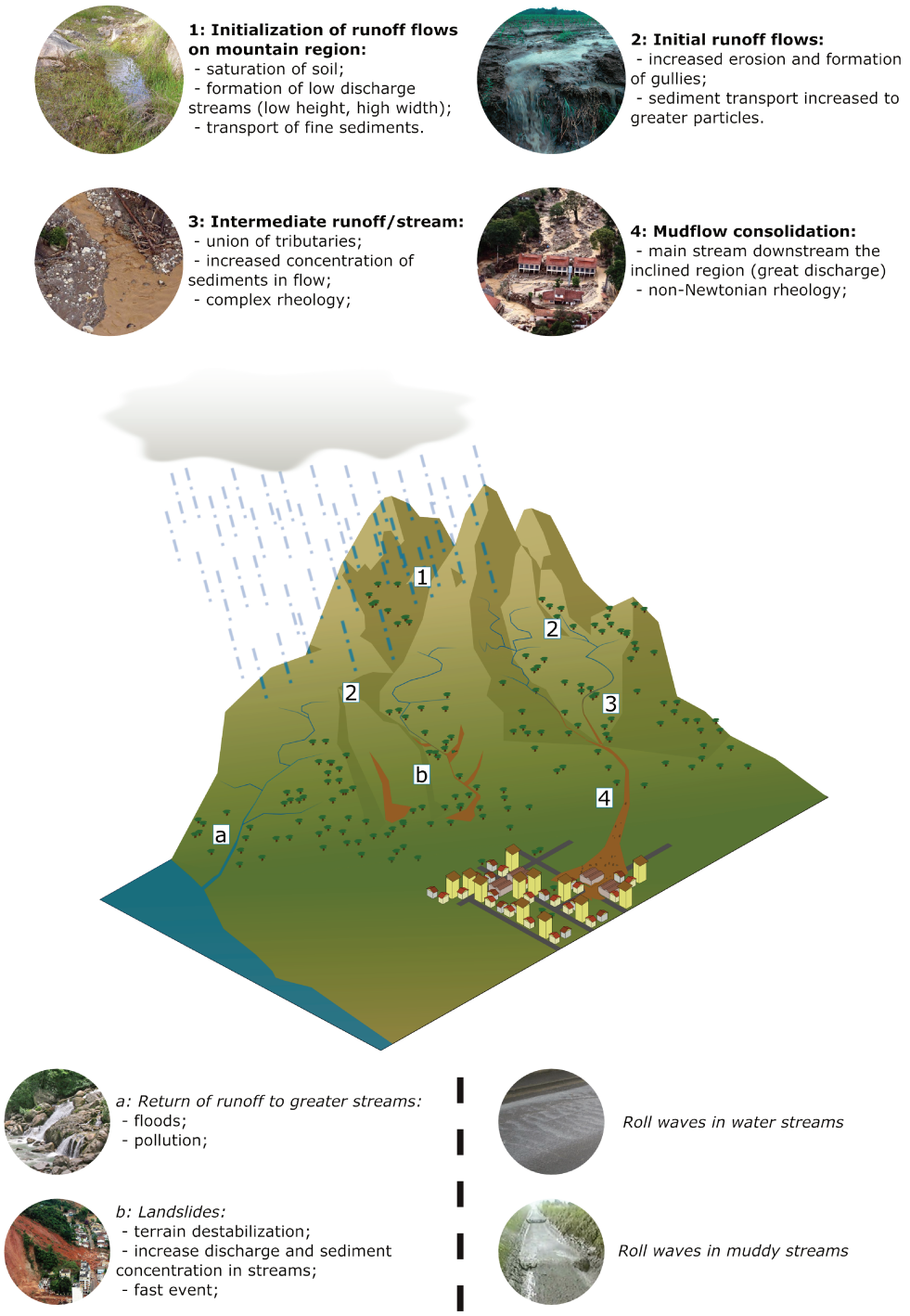

Figure 1.2: Illustration of process for gradually developed mudflow event.

From a mechanical approach, the runoff flow established during the initial and intermediary stage can be defined, in most of the cases, as turbulent flow of almost clean water. Sometimes, in the presence of vegetation, constriction of paths and even topography (convex areas), the flow can be thin and/or narrow, creating a thin layer of flow with intermediary dynamic between laminar and turbulent (Strahler, 1952). Due to the increased slope, mean flow velocities are sufficiently strong to have considerable capacity of transporting fine sediment material.

Depending on flow dynamics and sediment properties, transport mode of sediment in such flows can achieve different forms: sediment can rest in contact with the bottom (bed load), eventually jump and/or project itself into the flow (saltation), or completely be carried away by flow (suspension). For runoff, transport mechanisms of fine sediments are mainly bedload and saltation, sometimes praising suspension when flow occurs over clayey soil. However, as flow discharge in gullies are relatively small, volume concentration of solid in fluid do not exceed 8% in the composition of the fluid, thus keeping it as a Newtonian fluid (Graf and Altinakar, 2000).

In the last stage, the established mudflow usually diverge its viscous properties from the initial stage, since the increase in discharge made possible to carry more sediments along with flow. Despite the relatively high velocity achieved in such flows, they are usually laminar, with a completely different dynamic from the initial and intermediary stage (Coussot, 1994; Coussot and Piau, 1994).

Some questions may arise when dealing with those natural event such as:

- mudflow success of generation, i.e. whether the three main features said before (rainfall, soil and topography) convolute to lead to a so to speak mudflow event;
- once the event is established, what would be the properties of final stage event (flow and fluid properties);

The first addressed question can sometimes be answered for suddenly generated events if quantified values are obtained for the three main features involved in the mudflow generation (precipitation, soil and topography). With sufficient information about the soil, one can determine how much water will flow over the surface and how much will be the seepage of

water through the soil. Given the topography, it is possible to run models of stability and determine whether dislodge volume of solid and water will form a "continuous" flux of mud along the basin (Luna et al., 2011; Gomes et al., 2008; van Asch et al., 2007).

However, the gradually generated events scenario is theoretically "weaker", with a flow that has a hypothetic maximum capacity of transport sediment material (Graf and Altinakar, 2000). Thus, the sediment transport during runoff has to be properly estimated to allow correctly prediction on how fast flow dynamics would change (from turbulent clean water to laminar muddy fluid flow). Of course this matter also depends on topography and increase in discharge (so flow capacity of transport would increase), but predictions on sediment transport for free surface flows are still a matter of discussion in the scientific community and this work takes part on such matter and addresses the effect of fluctuations of flow dynamic properties on the transport.

In the other hand, flow and fluid properties in the final stage of the event should be the major data required. One can relate flow properties (such as height and velocity) with energy level and thus destructive capacity of events (Zeng et al., 2015) although few works seem to develop such approach. However, flow properties only make sense as long as we know what fluid we are dealing with. In fact, fluid properties generally indicate how flow will behave, thus pointing out that they must be primarily quantified to estimate flow properties. We must recall that fluid properties of mixtures must be studied from a rheological point of view which shows that such muddy material behave very differently from water. Apart from the fluid itself, the geometry of the channel and its properties also play an important role to determine flow properties. Nevertheless, flow properties are not restrict to mean values. Usually in natural events, many types of unsteady phenomena can have place during the event.

For the initial runoff stage, given the turbulent nature of the flow, many are the sources responsible for non-stationary phenomena and unsteadiness. The turbulent fluctuations present in such flows are themselves an important source of time and spatial variations of velocity property. It is known that sediment transport occurring due to steady and uniform turbulent flows do present variability of solid discharge (Frey et al., 2003; Ancey et al., 2008). Free surface flows such as those can be easily disturbed (by topography, rain, etc.) and lead to formation of surface instabilities (i.e. variation of flow properties along time and space). Differently from empiri-

cal laws established for steady and permanent flows, transport phenomenon doesn't happen the same way, as significant variations of stress applied over grains are identified and grains develop horizontal acceleration. Conversely, recalling the suddenly developed mudflows, it is possible to model it as a dam break flow, in which an abrupt variation of flow properties is propagate downstream.

Specially, a particular kind of free surface instability can appear in both scenarios, runoff and mudflow. This instability, usually called roll wave, is defined as steep periodic surges, propagating downstream in stabilized form, i.e. with constant wave properties (amplitude, wavelength and propagation velocity). Such waves appear naturally if flow conditions are favorable and random disturbances applied to flow by environment are inside a proper range. Low/high disturbances are amplified/damped until permanent configuration is reached, after traveling a certain channel length. Such waves receive a particular name called roll waves.

From the hydraulic perspective, regarding turbulent flows, these waves appear like hydraulic jumps, i.e. transitions between fluvial to torrential flow. Widely known, such structure is highly dissipative and could induce many different levels of risks depending on nearby civil infrastructure. When present in runoff, less is known about roll waves, whether they appear, if they contribute to the sediment transport, or how they interact in the formation of gullies and ravines. They can be perceived as non-constant flow but how such feature interacts with the mobile bed structure still rests not completely understood. Much more is known about roll waves in mudflows. Zanuttigh and Lamberti (2007) for example summarizes much of what is found in the literature about such events. The challenge however is: first, approximate models to the realistic problem, given its complexity; second, associate its presence with risks incurred by endangered societies. Despite of the fact that no proof of roll waves appearance have been noticed on Brazilian territory, other countries like New Zealand, China, Switzerland and Italy have already confirmed presence of surges and wave trains on mudflows over mountain regions (Zanuttigh and Lamberti, 2007).

1.3 Objectives

The question addressed in this research is an issue that interest not only Brazilian Government[1] but world communities: **how unsteady flow dynamical properties (from turbulence or roll waves) would change the evolution of one potential mudflow?** Upstream, when runoff takes place, how turbulent properties affect the variability found in total amount of sediment transport? Furthermore, how would surface instabilities (specially roll waves) change (or not) sediment transport dynamics? And downstream, where mudflow is developed, can we satisfactorily predict roll waves properties based on the most realistic scenario? The answer to these questions should help understand how important are such hydraulic instabilities for a precise evaluation of a potential mudflow event. From an Engineering perspective, the better we know about a problem and time-dependent phenomena that are related to it, the more precisely we can predict those events characteristics and thus optimize process, design structures, and reduce social and financial losses.

This thesis brings a work that will try to answer these questions by two different approaches on two different stages of an event:

- a laboratory experiment for turbulent open-channel flow over a mobile bed of sediments, looking for the source of sediment transport variations and trying to understand what happen when surfaces instabilities are present;

- a second approach will study roll waves main properties from a theoretical approach, based on the mudflow configuration, flowing down an inclined porous bed, and will try to verify the validity of such model based on *in situ* measurements.

This thesis brings then two parts concerning each of the approaches previously explained. The first part will detail the experimental methodology used in this work in order to obtain flow and sediment transport properties over time. Such information allowed some further investigations on the relations between both and show how mean and fluctuating flow properties are related to mean and fluctuating solid transport properties. The effects of free surface instabilities over the solid transport is then analyzed. The second part brings an application of roll waves mathematical model to a

[1] Conselho Nacional de Desenvolvimento Científico e Tecnológico - CNPq - is the Brazilian Government Institution that finance the author's scholarship

natural event occurred in Acquabona watershed. Based on the informations that could be gathered from the site, we show that it is possible to assess the amplitude of roll waves instabilities that could have been developed on that natural environment with a certain margin of error. A more complex model for the velocity profile is then proposed, considering the porosity of the bed. The test-case is again evaluated. In the third part, we bring discussions about the results presented and some perspectives of this work.

Chapter 2

Physical and mathematical review

2.1 Introduction

As addressed in the introductory part, when looking for gradually developed mudflows, two different scenarios are at stake during its evolution: the runoff, where initial sediment transport is observed; and mudflow, a flow of aqueous mixture of solid sediment particles. Considering the following geometry for the channel in both scenarios:

- rectangular cross-sectional;
- slope angle of θ degrees;
- long waves approximation - longitudinal characteristic length L_0 is much greater than cross-sectional l_0 or vertical h_0 ones ($L_0 \gg l_0 \gg h_0$);
- negligible friction on the lateral walls[1] - cross-sectional characteristic length l_0 is much greater than vertical one ($l_0 \gg h_0$);

Schematically, the representation of such flow would be as shown in Figure 2.1. Characteristics properties of flow are: flow discharge Q ($\mathrm{m^3 s^{-1}}$); mean flow height h_0 (m); mean flow velocity u_0 ($\mathrm{ms^{-1}}$); specific flow discharge ($\mathrm{m^2 s^{-1}}$),

$$q = Q/l_0 = h_0 u_0. \tag{2.1}$$

[1] This hypothesis requires that channel width should be at least 20 times much larger than flow height.

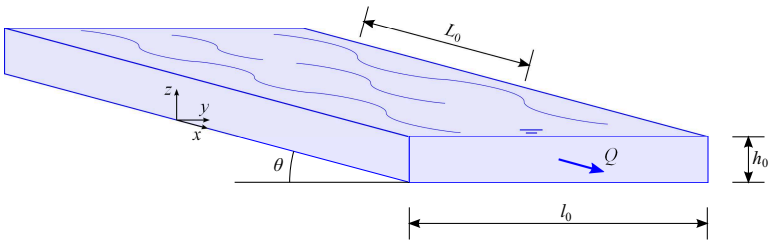

Figure 2.1: Schematic representation of a three-dimensional open-channel flow and the geometrical characteristics of interest in such problems.

The equations that govern the problem are mass and *momentum* conservation equations (Chassaing, 2010):

$$\frac{\partial \rho}{\partial t} + \frac{\partial (\rho u_i)}{\partial x_i} = 0; \tag{2.2a}$$

$$\frac{\partial \rho u_i}{\partial t} + \frac{\partial (\rho u_i u_j)}{\partial x_j} = \rho F_i + \frac{\partial \sigma_{ij}}{\partial x_j}, \tag{2.2b}$$

where $i, j = 1, 2, 3$ are index that identify components of spatial coordinates x_i; t is the time variable; u_i are components of velocity field; F_i are components of body forces; σ_{ij} represents the components of the stress tensor; and ρ is the fluid density.

Since dealing with open-channel flows, the only body force acting on the problem is the gravity, represented by its acceleration g_i. The influence of gravity on each direction depend on the slope. Fluid is considered incompressible. The stress tensor, symmetrical, can be separated on normal and shear stress components. The former is represented by pressure P (scalar), that acts uniformly on every direction. The latter, by the viscous forces, represented by τ_{ij} which vary depending on the fluid rheology. Mathematically:

$$\sigma_{ij} = -P\delta_{ij} + \tau_{ij}, \tag{2.3}$$

where δ_{ij} is the Kronecker delta (unit tensor) such that δ_{ij} is 1 if $i = j$ and 0 if $i \neq j$.

Fluid density and viscous stress tensor should depend on the volumetric concentration of particles ϕ_v in the fluid mixture, so that $\rho(\phi_v)$ and $\tau_{ij}(\phi_v)$, but then again, ϕ_v is constant during a process. At this point, we should remember the Reynolds number, which represents the ratio between inertial forces (represented by mean flow velocity u_0) and viscous forces, opposing

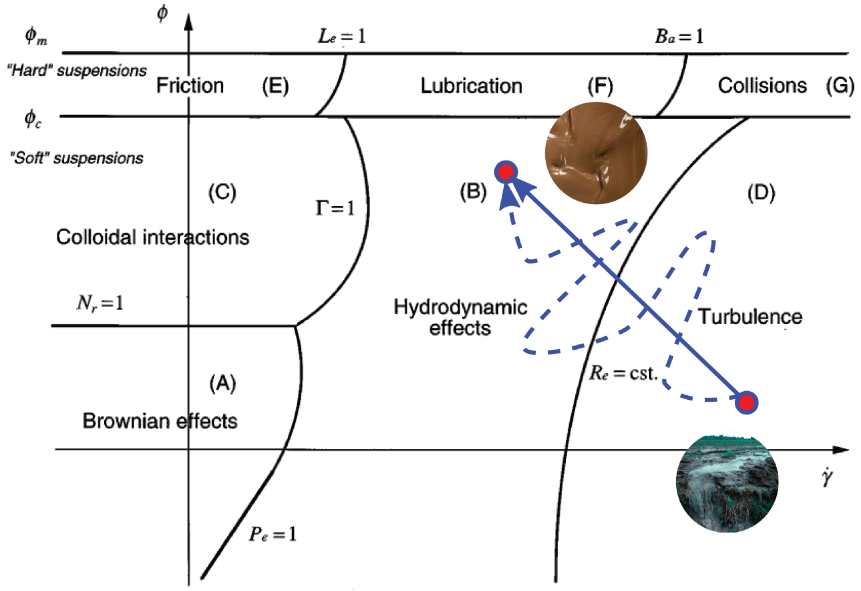

Figure 2.2: Simplified diagram of flow regimes from Coussot and Ancey (1999) using shear rate $\dot{\gamma}$ and particle concentration in mixture ϕ_v. The transitions between regimes are described using dimensionless numbers. For details of such numbers, see Coussot and Ancey (1999).

the fluid movement. The Reynolds number should assume different forms depending on the rheological approach given to the fluid. Then, the two scenarios at stake can be differentiated based on two main features: concentrations of particles in the fluid; and flow shear rate, $\dot{\gamma} = \partial u_i / \partial x_j$. Such categorization is summarized in the work from Coussot and Ancey (1999) by Figure 2.2. For the runoff stage, concentration of particles should be low ($\phi_v < 1\%$), than the viscosity is the viscosity of the interstitial fluid (water, $\sim 10^{-3}$ Pas). High shear rate is noticed ($\dot{\gamma} \sim 10^2$ s^{-1})[2], thus fitting into region (D). For mudflow stage, high concentration of particles will change fluid rheology and flow dynamics, increasing viscous effects, reducing shear rate ($\dot{\gamma} \sim 10^0$ s^{-1}), thus fitting to region (B). Many effects are neglected in the approach undertaken in this work such as the presence of colloidal substances, temperature gradient, and hard suspensions (prominent particle-particle interactions). Both regions of interest here, (B) and (D), are governed by fluid mechanics laws such as Equations 2.2a and 2.2b, previously presented. The evolution of properties from a flow from region

[2]combination of low viscosity and high shear rate leads to great Reynolds number - Turbulent flow.

(D) to region (B) however is not quite well understand. Many effects could be present during a natural event that can change the path of transition. For example, the flow capacity of transport is related to the flow discharge and characteristics of soil particles. Any variation of geometry and/or flow discharge would change the overall flow capacity, thus also changing the particle entrainment rate. Nevertheless many time-variable effects appear which somehow are supposed to affect the flow dynamics and its interaction with sediment transport. Such kind of events require a more specific approach. One among them is the roll waves instabilities, which are considered in this work, as will be shown.

Using the hypothesis presented before (incompressibility of fluid and flow) and the form stress tensor (Equation 2.3), the conservations equations can be rewritten as:

$$\frac{\partial u_i}{\partial x_i} = 0; \tag{2.4a}$$

$$\frac{\partial u_i}{\partial t} + u_i \frac{\partial u_j}{\partial x_j} = -\frac{1}{\rho}\frac{\partial P}{\partial x_i} + g_i + \frac{1}{\rho}\frac{\partial \tau_{ij}}{\partial x_j}. \tag{2.4b}$$

To summarize the evolution of a gradually developed mudflow, one should assume for example a longitudinal line from watershed, as illustrates 2.3(a), starting one end at the beginning of the runoff stage and the other end at the consolidated mudflow stage. Following this line, discharge in the stream will continuously increase. Consequently, flow erosion capacity will also increase and so the quantity of solid sediments entrained. What could be observed, schematically, would correspond to the 2.3(b). A clear water flow, turbulent and Newtonian, where particles initiate their movement, that continuously suffers increase of discharge and transport capacity (affecting particles entrainment/transport), incorporating sediment material on the fluid (changing ϕ_v), until reach a maximum concentration of particles in the fluid mixture for the conditions at stake. Such change in concentration could be able to lead to a change in fluid rheological properties and consequently in flow dynamics (Coussot and Meunier, 1996; Graf and Altinakar, 2000). If this evolution is successful, the flow would now be laminar and non-Newtonian.

In the specific literature for mass movements, the rheological classification of an event would depend basically on the fraction of fine sediments to the total volumetric concentration of solid sediments (Figure 2.4), as proposed by Coussot and Meunier (1996). Then, when flow capacity Celik and Rodi (1991) is low, sediments are entrained close to the bottom. Two-phase

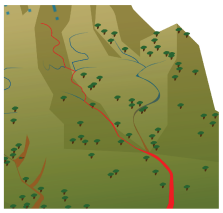

(a) : Line from the watershed.

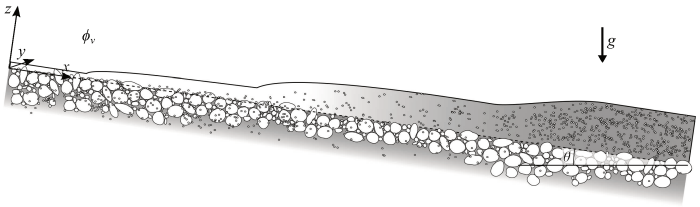

(b) : Illustration for mudflow evolution.

Figure 2.3: Schematics representation of gradually developed mudflow. Increase in flow height represent discharge income. Gray shade represent high concentration of sediments in fluid mixture.

flow is established and sediments are transported in bedload discharge. As flow discharge increases, more and more particles are entrained and incorporated to mixture, especially fine sediments which are easily washed downstream. This would change the overall dynamics of the fluid, and flow is frequently modeled as equivalent one-phase flow.

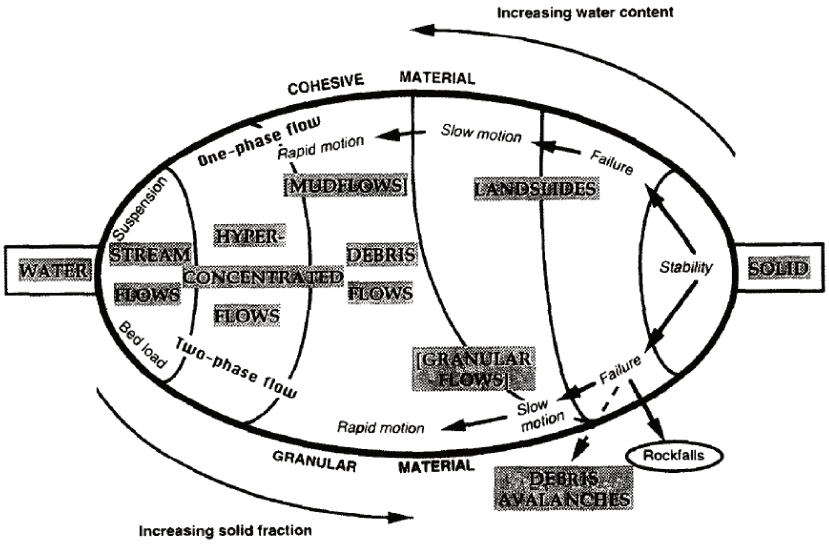

Figure 2.4: Classification of mass movements on steep slopes as a function of solid fraction and material type. From Coussot and Meunier (1996).

2.2 Turbulent flow and sediment transport

On open-channel hydraulics, sediment transport is a matter of study that have great interest due to its importance to the environment. Informations such as quantity of solid material transported by flow and properties of bedform structures are the main concerns of that matter of study.

Flows occurring over large surfaces, with a small flow height, are a common scenario where sediment transport is established. Rain pouring over sedimentary or non-sedimentary soils induce the formation of preferential flow paths, usually of small height (< 10 mm), even when compared to its width. This kind of flow is called runoff and is one of the most common flow of water cycle on Earth surface. As shows Figure 2.5, such kind of flow is present in many environments, artificial or natural, changed or not by human interference.

2.2.1 Flow hydraulics

Runoffs are usually turbulent, composed by water with very small concentrations of particles, and have a considerable capacity of transporting sediment material and pollutants. Depending on flow dynamics and sediments grain size distribution, transport mode of sediment can vary from bed load (for coarse and fine sands), praise saltation and reptation regimes (for fine sands and silt) and even reach intrinsic suspension mode (for clay and pollutants).

For runoff flows, shallow clear water flow occurs over a mobile bed. The fluid being Newtonian, the viscous stress tensor is:

$$\tau_{ij} = \mu \left(\frac{\partial u_i}{\partial x_j} + \frac{\partial u_j}{\partial x_i} \right), \tag{2.5}$$

where μ is the fluid dynamic viscosity[3].

At this point, we can define the Reynolds number for this kind of fluid:

$$\mathrm{Re} = \frac{4\rho h_0 u_0}{\mu}. \tag{2.6}$$

For turbulent flow, $\mathrm{Re} > 2000$. Considering the geometrical hypothesis before (section 2.1), the flow could be modeled as one-dimensional, and

[3]The dilation/compression effects are neglected, $\partial u_i / \partial x_i = 0$

(a)

(b)

(c)

(d)

Figure 2.5: Examples of runoff flows in different environments. 2.5(a): runoff on paved street; 2.5(b): runoff on mountain region; 2.5(c): runoff in vegetable area; 2.5(d): runoff occurring on agriculture zone.

considering the flow dynamic is turbulent, the problem is "simplified" into the following system:

$$\frac{\partial u}{\partial x} + \frac{\partial w}{\partial z} = 0; \tag{2.7a}$$

$$\frac{\partial u}{\partial t} + u\frac{\partial u}{\partial x} + v\frac{\partial u}{\partial y} = -\frac{1}{\rho}\left(\frac{\partial P}{\partial x}\right) + g_x + \nu\left(\frac{\partial^2 u}{\partial x^2} + \frac{\partial^2 u}{\partial y^2}\right); \tag{2.7b}$$

$$\frac{\partial v}{\partial t} + u\frac{\partial v}{\partial x} + v\frac{\partial v}{\partial y} = -\frac{1}{\rho}\left(\frac{\partial P}{\partial y}\right) + g_y + \nu\left(\frac{\partial^2 v}{\partial y^2} + \frac{\partial^2 y}{\partial y^2}\right); \tag{2.7c}$$

where u and v are instantaneous longitudinal and vertical velocity components and $\nu = \mu/\rho$ represents the kinematic fluid viscosity. The velocity can be decomposed in mean and fluctuating variables:

$$u_i(x_j, t) = \bar{u}_i(x_j, t) + u'_i(x_j, t), \tag{2.8}$$

where $\bar{u_i}$ represents the statistical mean value over time and u_i' the fluctuations. In permanent and steady conditions, further simplifications of the problem can be performed through the boundary layer theory (Schlichting, 1979). The problem is solved and the law of the wall (Von Kármán, 1930) is reached so that we obtain flow velocity profile $\bar{u}(y)$, with a negligible mean vertical velocity and a mean longitudinal velocity depending on the vertical component y. In that theory, two different zones are presented: one where the drag comes mainly from fluid viscosity (viscous sublayer - small scale/molecular), close to the walls; and another far from the wall where viscosity is negligible and only turbulent dissipation can be considered (log-law region). The problem is scaled to the specific velocity u_* called friction velocity where

$$u_* = \sqrt{\frac{\tau_b}{\rho}}, \tag{2.9}$$

and τ_b is the shear stress applied to the walls/bottom. When in steady and permanent configuration for a flat bed, hydrostatic conditions are reached. The bottom shear stress can be written as function of the water column:

$$\tau_b = \rho g h_0 \sin\theta. \tag{2.10}$$

The scaling is done as:

$$u^+ = \frac{u}{u_*}; \tag{2.11a}$$

$$y^+ = \frac{u_*}{\nu} y. \tag{2.11b}$$

.

Then the velocity profile present the behavior illustrated on Figure 2.6. The flow velocity profile $u(y)$ assumes different form depending on each zone of the boundary layer. For the viscous dominant, velocity depends linearly on the vertical coordinate

$$u^+ = y^+, \tag{2.12}$$

and for turbulent dominant region (log-law region), it follows

$$u^+ = \frac{1}{\kappa} \log y^+ + B, \tag{2.13}$$

where $\kappa = 0.41$ is the von Kármán constant and B is an adjustment coefficient depending on the channel wall roughness.

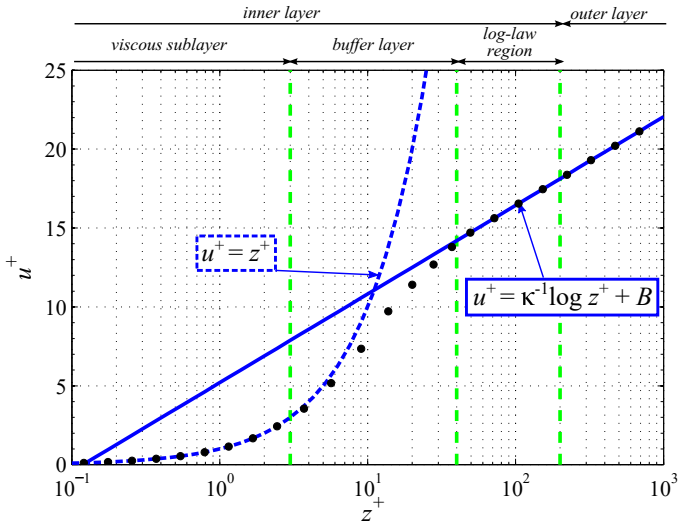

Figure 2.6: Law of the wall as presented by Von Kármán (1930). Blue lines represent viscous dominant and log law behavior. Black dots reproduce a typical velocity profile.

2.2.2 Sediment transport

Wall roughness is given based on the type of sediments that are distributed in the bed, their mobility and the subsequent bedform presence. Bed sediments are characterized depending on their density ρ_s and their size (diameter) D. Depending on shear rate applied by flow on bed particles, or more precisely flow friction at the bed, flow is capable to overcome static state of particles, and then to transport sediment material along with it. This threshold state is related to particles geometry and submerged weight (Shields, 1936) (see figure Figure 2.7) and threshold is often related to a minimum stress value or critical value τ_c (or a critical friction velocity u_{*c} (Armanini and Gregoretti, 2005)). The relation between kinetic energy available on the flow and sediments potential energy is given by the Shield's number Sh (Equation 2.14):

$$\mathrm{Sh} = \frac{\tau_b}{(\rho_s - \rho)gD} > \mathrm{Sh_c}, \tag{2.14}$$

The minimum Shield's number is represented by $\mathrm{Sh_c}$.

One of the factor that is included into the critical shear velocity concept is the sedimentation velocity v_s, which represent the particles weight. The relation between friction velocity and sedimentation velocity relation is also

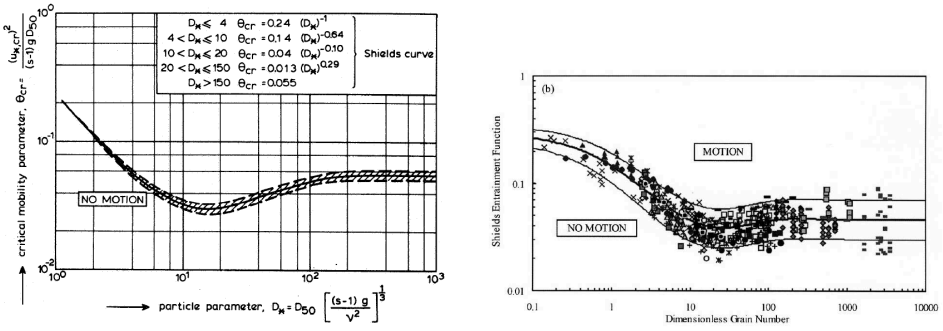

(a) (b)

Figure 2.7: Critical Shields number against dimensionless grain diameter as presented by 2.7(a), van Rijn (1984) referencing the work of Shields (1936); and 2.7(b) more recent work from Paphitis (2001).

called movability number and can also be used to understand the imminence of movement. Recent works (Paphitis, 2001; Beheshti and Ataie-Ashtiani, 2008) use the movability number as function of dimensionless grain diameter D_*,

$$D_* = D\left(\frac{g(s-1)}{\nu^2}\right)^{\frac{1}{3}}, \tag{2.15}$$

to study the threshold of sediment movement, as shows Figure 2.7. The empirical equation proposed by Paphitis (2001) that covers a large range of dimensionless grain diameter was found based on many experimental runs collected from the literature:

$$\mathrm{Sh}_c = \frac{0.273}{1+1.2D_*} + 0.046(1-0.57e^{-0.02D_*}), \tag{2.16}$$

for $0.1 < \mathrm{Re}_* < 10^4$, where $\mathrm{Re}_* = u_* D/\nu$. This equation represents the mean threshold curve estimated by those authors. The lower and upper limits shown in Figure 2.7 are:

$$\mathrm{Sh}_c = \frac{0.165}{0.7+1.2D_*} + 0.03(1-0.57e^{-0.02D_*}), \tag{2.17a}$$

$$\mathrm{Sh}_c = \frac{0.380}{1.2+1.2D_*} + 0.07(1-0.57e^{-0.02D_*}), \tag{2.17b}$$

respectively. These limits should be used to estimate the uncertainties of measurement.

Depending on particle-flow interaction, different kind of transport modes can appear. During their movement, particles will eventually fall back to bed with velocity v_s which depends on flow dynamics and particles themselves:

$$v_s^2 = \frac{\nu}{3}\frac{(s-1)gD}{C_d}, \tag{2.18}$$

where $s = \rho_s/\rho$ and C_d is the drag coefficient of the particle. Simpler and empirical relations have been studied for practical purpose such as the one reached by (Zhiyao et al., 2008) based on experiments from the literature:

$$v_s = \frac{\nu}{D} D_*^3 \left[38.1 + 0.93 D_*^{12/7}\right]^{-7/8}. \tag{2.19}$$

If particles sedimentation velocity is much greater than friction velocity, particles will be stuck in the bed, and will not be transported. If friction velocity is greater enough to surpass the critical value, particles will stay in contact with the bed, making small displacement, characterizing the bedload transport. For greater shear stress applied to the bottom, particles will be able to make higher jumps (saltation regime), and eventually being suspended (suspended load) and carried away by flow (Bagnold, 1966) (Figure 2.8). The relation between sedimentation velocity and shear velocity can be used to identify how transport will happen.

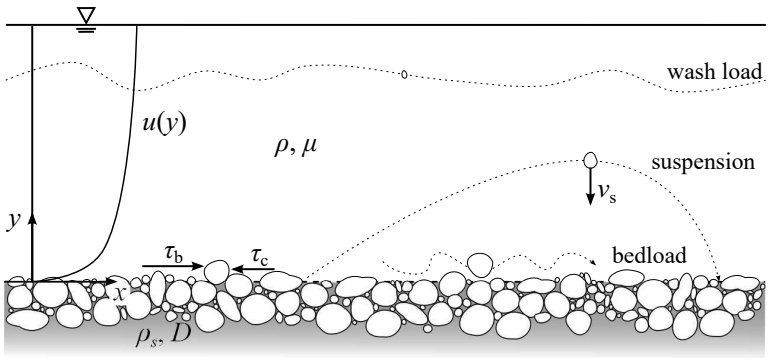

Figure 2.8: Schematic representation of open-channel flow in presence of a mobile bed.

Considering for example a poly-dispersed mobile bed, i.e. very broad grain-size distribution. For $v_s/u_* > 1$, the sedimentation velocity is high enough so smaller sediments will move rolling, sliding or jumping in small hops. For $v_s/u_* < 1$, particles make long jumps, eventually falling back to the bed, but travel more time along the flow, sometimes even reaching the flow surface. This particle transport mechanism is called inhomogeneous

suspended load, presenting a concentration profile that decreases with vertical coordinate. For v_s/u_* small enough, the flow stress applied into the mobile bed is great enough to make small particles travel along the flow, characterizing the intrinsic suspended load or wash load and the concentration profile becomes almost a constant. The Rouse number:

$$\mathrm{Ro} = \frac{v_s}{\kappa u*}, \tag{2.20}$$

sometimes is also used to relate the same behavior:

- Ro > 2.5 - bedload transport;
- $1.5 <$ Ro < 2.5 - up to 50% suspended load;
- $0.8 <$ Ro < 1.2 - up to 100% suspended load;
- Ro < 0.8 - intrinsic suspended load.

So, for a fixed mono-dispersed grain-size distribution (particles with a Gaussian distribution centered at a specific diameter D), the proportionality between shear rate and Shield's number allow us to identify regions of transport modes inside the regions (B) and (D) from Figure 2.2:

- at low shear rate, bed load transport takes place. A thin sheet of particles moves close to bed. Fluid keeps its original properties and small influence is perceived by flow. Flow capacity is usually limited to values smaller than packing concentration ϕ_c and no fluid variation is perceived along vertical coordinate.
- For intermediate shear rates, suspended transport mode takes place. Particles concentration become better distributed along vertical coordinate. Quasi-Newtonian rheologies could be still employed on fluid representation as their presence might change fluid viscosity.
- at higher shear rates, sediments concentration can become more equally distributed in y. Concentration might reach relatively high values, sometimes reaching minimum packing value ϕ_c, and then changing flow regime.

Parallel to the one presented on Figure 2.4, considering water-sediment mixture, Graf and Altinakar (2000) define the type of sediment transport as function of the concentration of sediment particles, which can also change flow dynamics, as shown on Table 2.1.

Table 2.1: Mixture flows simplified classification (Graf and Altinakar, 2000).

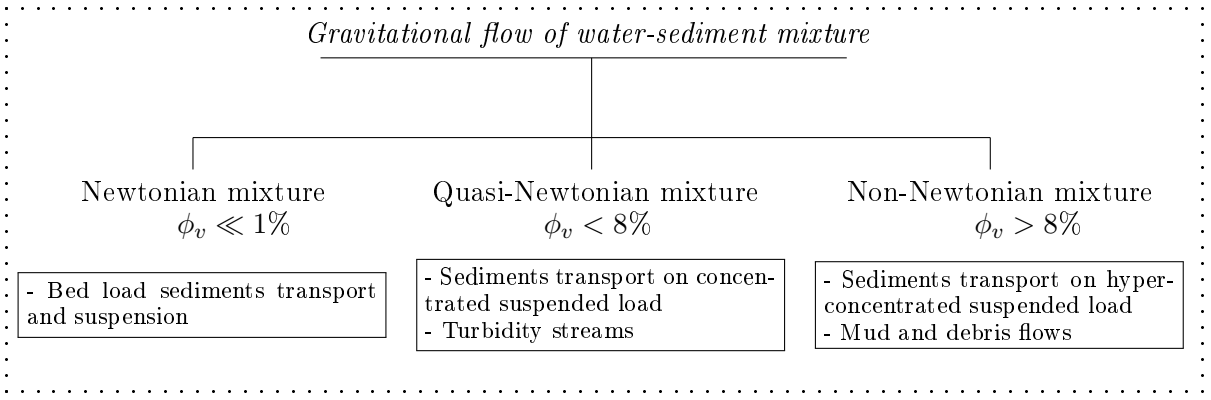

- Flow mixture will behave as Newtonian if the volume concentration of particles (sediments) is very low, i.e. $\phi_v \ll 1\%$. Bed and suspended load are characterize by this level of concentration and are the most frequent type of flow on water streams.

- Flow mixtures will behave as quasi-Newtonian solutions if the concentration is still low, $\phi_v < 8\%$. Concentrated suspended load and turbidity streams are characterize by concentrations of this magnitude.

- Finally, flow mixture will behave as non-Newtonian if $\phi_v > 8\%$. Non-Newtonian fluids have completely different behavior from Newtonian ones and change flow dynamics drastically, included friction. Particles will rest suspended for long time and sedimentation velocity will be influenced by the concentration. Sediments transport in hyperconcentrated solutions characterize mud flows and also hyperconcentrated turbidity streams. It can be generate by a great discharge rate of fine sediments on a low steep water open-channel flow, which usually can be seen on rainy season. Another possibility are the formation of torrential lavas on very steep channels, $\theta > 15°$, that are composed by a vast domain of particles, from cohesive fine particles to large blocks of rock (~ 1 m^3), and are considerably fast.

Experiments from Maciel et al. (2009) confirm that non-Newtonian behavior on water-sediment mixtures for $\phi_v > 5\%$, slightly before the 8% from Graf and Altinakar (2000). The transition between Newtonian and non-Newtonian behavior for one single event can be explained by Berzi and Fraccarollo (2013): channel steepness control the distribution of sediment

particles in the vertical coordinate, and thus its influence on the mixture overall behavior (Figure 2.9). In this way, increasing the steepness, higher concentrations could be achieved.

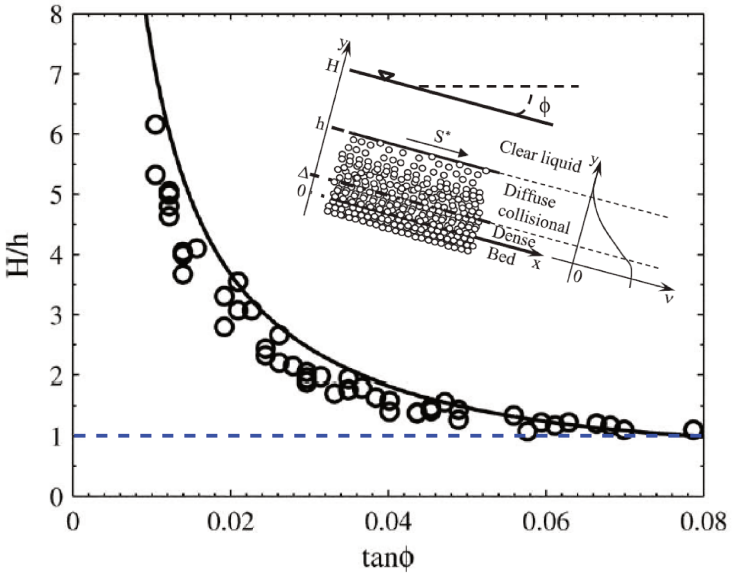

Figure 2.9: Experimental and theoretical degree of saturation as a function of the bed slope for plastic particles in water. In the up-right corner, sketch of the flow configuration with the frame of reference and a generic concentration profile (Berzi and Fraccarollo, 2013). The degree of saturation is the ratio between mean flow height and maximum height of transported particles jumps. For such ratio equals to 1, particles trajectories cover all position in the flow height.

2.3 Laminar flow and non-Newtonian fluids

Mudflows are often characterized as saturated flows, aqueous mixtures with high concentration of solid material. The variability found on solid-liquid fraction composing the mixture contribute to the complexity of the fluid which could acquire cohesive or non-cohesive behavior, depending on the material in suspension, specially for natural environments (Malet et al., 2003; Remaître et al., 2005). For mixtures where sediment concentration is high and the energy dissipation is mainly viscous, the mixture behavior can be characterized by an equivalent fluid model, employing a rheological model, which sums up contributions of particles and fluid interactions. The

main feature of such models is the presence of a yield stress, thus pointing out non-Newtonian rheological behavior of fluid.

To our knowledge, flows of complex fluids are yet to be completely understood by scientific community. Present in many branches of technological and scientific matters, the knowledge of such kind of flow, and even of complex fluids, is clearly an open task that interest all community. From complex fluids, one should understand fluids that present a non-Newtonian rheology, where shear stress and shear ratio are not linearly proportional by a constant fluid viscosity (μ).

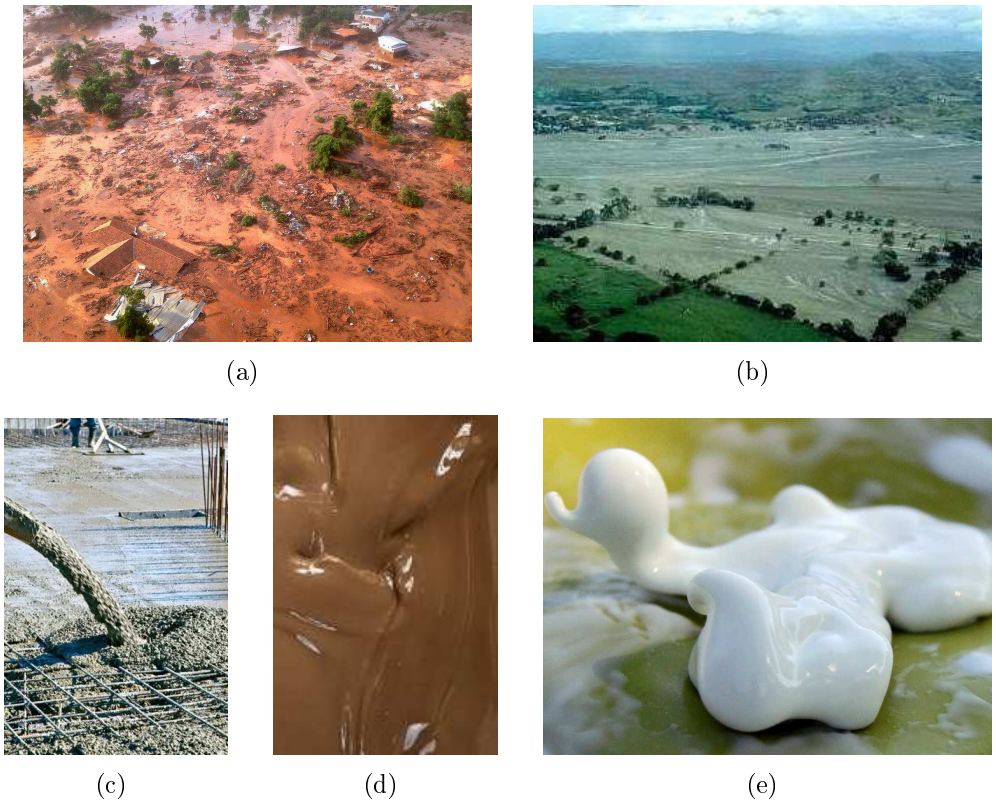

(a) (b)

(c) (d) (e)

Figure 2.10: Examples of non-Newtonian fluid flows in different environments. 2.10(a): mud dam-break event of Mariana district, Minas Gerais state, Brazil, 5th November 2015; 2.10(b): lahar flow from late November 1985 in Río Lagunillas, former location of Armero, Colombia; 2.10(c): concrete been poured; 2.10(d): drilling mud used in oil industry; 2.10(e): cornstarch mixture subdue to stress from speaker vibration.

Particularly, Herschel-Bulkley fluids show yield and also non-linearity between shear rate and shear stress. Polymer mixtures (gels), water mixtures of solid particles (cement, mud), emulsions, sols and many others are classical examples of such fluids (Balmforth et al., 2014), as illustrates Figure 2.10. When dealing in simple shearing conditions, those fluids can be represented by the following model,

$$\tau_{xy} = \tau_0 + K_n \left(\frac{\partial u}{\partial y} \right)^n, \quad \text{for} \quad \tau > \tau_0, \tag{2.21}$$

where τ_0 represents the yield (formally fluid yield stress), K_n is called consistency index, and n is the power-law index for fluid, which gives the non-linearity between shear stress and shear ratio. When dealing with water-solid mixtures in isothermal conditions, these three parameters depend exclusively on the sediment properties: concentration, geometry, density, etc (Mueller et al., 2009). From the mathematical perspective, such model is rather interesting since it can be used to represent less complex fluids by simple manipulation of parameters: for $n = 1$, Bingham fluids are represented; for $\tau_0 = 0$, power-law fluids are fit; for $n = 1, \tau_0 = 0$, Newtonian fluids can also be represented. Even though research about modeling of yield stress still continues (Barnes, 1999; Rajagopal, 2006; Ovarlez et al., 2013), the model gives interesting insight and practical results about many kind of fluids.

For such kind of fluid, the Reynolds number have to be adapted to a more generic form (Haldenwang et al., 2002; Burger et al., 2010, 2015) to better fit the set of parameter used to define the rheological properties of the fluid:

$$\mathrm{Re} = \frac{8\rho u_0^2}{\tau_0 + K_n (2u_0/h_0)^n}, \tag{2.22}$$

considering the steady and permanent case, which velocity and free surface height are both constant values u_0 and h_0, respectively, as shows Figure 8.1.

The system of equations that govern the problem can be simplified from Equations 2.2a and 2.2b, considering the geometry and the laminar flow

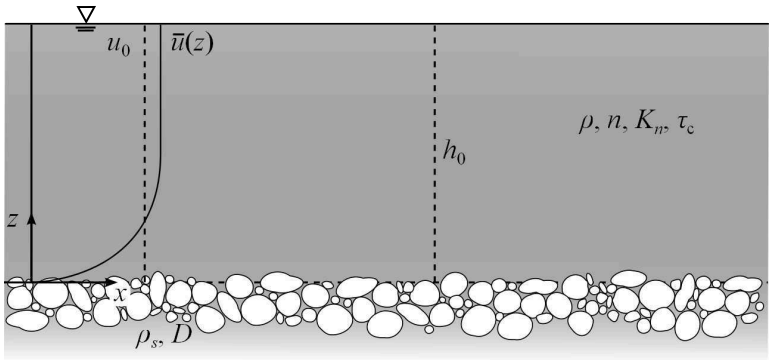

Figure 2.11: Schematic representation of flow. The gray color indicates that particles concentration are high in the mixture.

into the following equations:

$$\frac{\partial u}{\partial x} + \frac{\partial v}{\partial y} = 0; \tag{2.23a}$$

$$\frac{\partial u}{\partial t} + u\frac{\partial u}{\partial x} + v\frac{\partial u}{\partial y} = -\frac{1}{\rho}\frac{\partial P}{\partial x} + g\sin\theta + \frac{1}{\rho}\frac{\partial \tau_{xy}}{\partial y}; \tag{2.23b}$$

$$0 = -\frac{1}{\rho}\frac{\partial P}{\partial y} - g\cos\theta. \tag{2.23c}$$

At this point it is also important to define a dimensionless number that relates yield stress with flow height, which gives the idea on how important is flow yield compared to the bottom shear stress:

$$C^* = \frac{\tau_0}{\rho g h_0 \sin\theta}. \tag{2.24}$$

This dimensionless number is analogous to the Bingham number (for non-Newtonian fluid flows in pressure driven flows). It is the ratio between the fluid yield and the driven force, represented by the shear stress.

2.4 Free surface instabilities - Roll waves

Free surface instabilities are phenomena that inspire researches on many different subjects related to open-channel flows. From breaking waves and tidal bores, to roll waves instabilities (Figure 2.12), the interest on such phenomena lies in the fact that their appearance change the steady and permanent configuration of flow, sometimes affecting flow interaction with

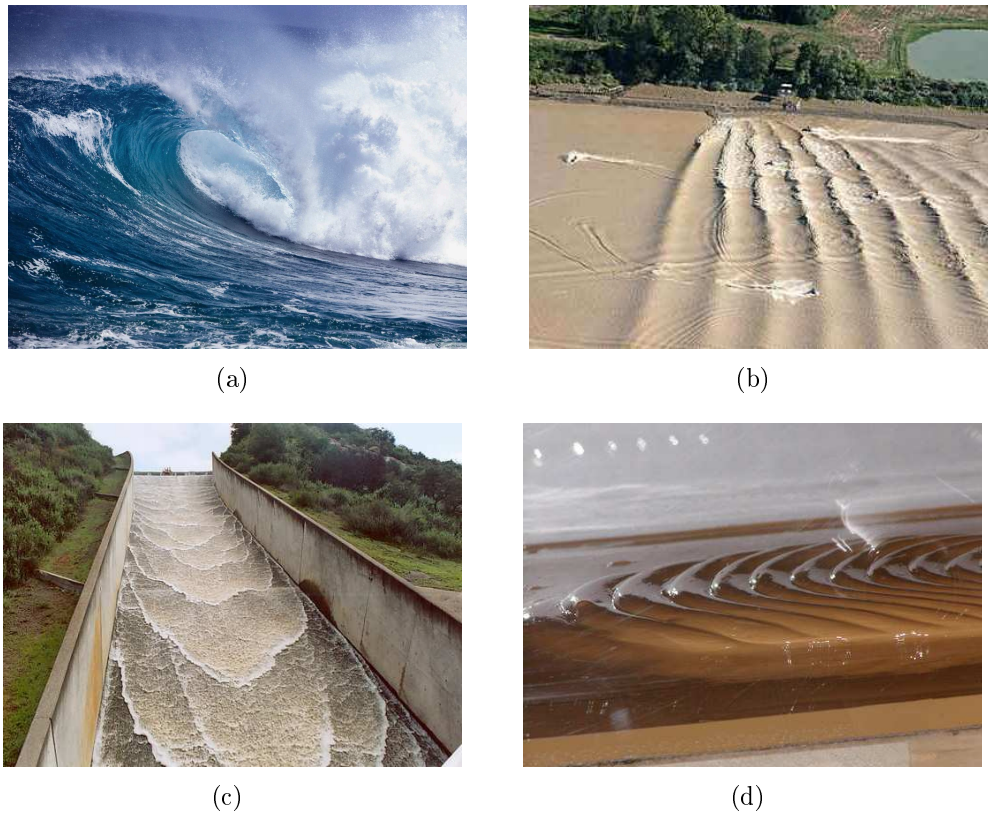

(a) (b)

(c) (d)

Figure 2.12: Examples of free surface instabilities in natural flows. 2.12(a): sea wave breaking when approximating the shore; 2.12(b): tidal bore at Vayres, Gironde, photo from Jacques Dassie personal website; 2.12(c): roll waves on clean water turbulent flow at Turner reservoir, San Diego County, California, on February 24, 2005, from personal website of Victor Miguel Ponce; 2.12(d): free-surface instabilities in a complex non-Newtonian fluid (Chanson et al., 2006).

the medium.

Shore erosion due to waves (van der A et al., 2013; Kranenburg et al., 2013) ans tidal bores (Chanson et al., 2012) are still matter of research in coastal engineering nowadays. When studying instabilities such as roll waves, which can appear not only on clean water turbulent flow but also on non-Newtonian flows at high steepness, there are yet questions to be answered.

When studying surface instabilities, their properties are the target. Profile $h(x,t)$, wave propagation velocity c, wavelength λ_w, wave period T_w and

amplitude Δh represent the classical set of properties, as illustrates on Figure 2.13.

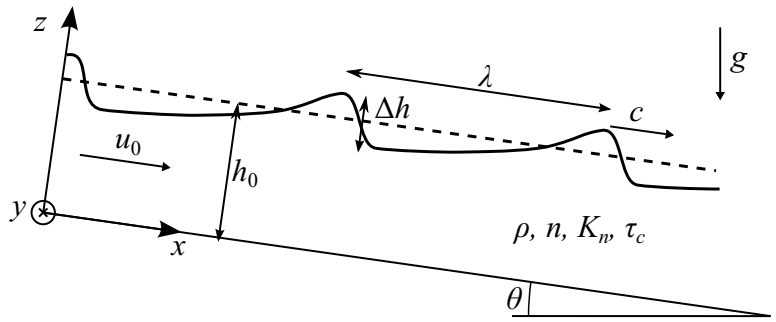

Figure 2.13: Open-channel flow when in presence of surface instabilities. wave properties are highlighted.

To obtain a representative system of equations, the conservation equations are vertically averaged by mean flow properties. The system usually employed is of the type (Balmforth and Mandre, 2004):

$$\frac{\partial h}{\partial t} + \frac{\partial (hu)}{\partial x} = 0; \tag{2.25}$$

$$\frac{\partial u}{\partial t} + \alpha u \frac{\partial u}{\partial x} + g \cos\theta \frac{\partial h}{\partial x} = g \sin\theta - C_f f\left(u, h\right) + \frac{1}{h}\frac{\partial}{\partial x}\left(h \nu_t \frac{\partial u}{\partial x}\right), \tag{2.26}$$

$$\tag{2.27}$$

where α represent a vertical *momentum* distribution coefficient,

$$\alpha = \frac{1}{h_0 u_0^2} \int_0^{h_0} u^2(y)\, \mathrm{d}y, \tag{2.28}$$

$C_f f\left(u, h\right)$ represent the bottom drag, with C_f a parameter, $f\left(u, h\right)$ a function of flow velocity and height, and ν_t the effective viscosity. When considering that flow could assume temporal and spatial variations, the hyperbolic nature of governing equations give the particular physical problem that is called roll waves. For a given set of special conditions, shock gravitational waves can be developed on the free surface of open-channel flows (Figures 2.12(c) and 2.12(d)). The basic feature to understand their appearance is the Froude number Fr, which relates flow and gravity waves velocities:

$$\mathrm{Fr} = \frac{u_0}{\sqrt{g h_0 \cos\theta}} \tag{2.29}$$

The slope is the main factor that drives the behavior of such waves. From the classical works from Vedernikov (1945); Chow (1959); Ponce (1991), roll waves might appear in every stage of mudflows evolution, presenting different conditions, represented by the Froude number, summarized by Table 2.2. Nevertheless, another important factor on such instabilities generation is the channel length. They required a minimum length to develop, considering an infinitesimal disturbance applied to permanent and uniform flow (Montuori, 1961, 1963). Given a random source of disturbances, it must exist a minimum channel length necessary for roll waves to completely develop. The amplitude and frequency of the disturbance are important to define such length. Since the solution of roll waves problem can be obtained from a second-order ordinary differential equation, the eigenvalues give the stability points and roll waves solution are an attractor of periodic solution established around one of those points. This means that the closer the initial condition (or disturbances) is to the periodic solution, the faster it will converge to it (Hwang and Chang, 1987; Needham and Merkin, 1984). Experimentally this have been observed by Fiorot (2012); Fiorot et al. (2015) for laminar Newtonian flows.

Although detailed observations on roll waves were first presented in 1910 by Cornish (1934), Jeffreys (1925) was the first to analyze the waves in clean water turbulent flows. The work determined the generation criterion for the problem as a specific value of the Froude number $\mathrm{Fr} > 2$; below this value, roll waves cannot appear. This value was then further adapted by Vedernikov (1945) to different channel configurations. Searching for more quantified data, Dressler's model (Dressler, 1949) tried to represent the wave profile. His formulation was peculiar because the solution of his equation presented an intermediate value for the wave height, at which no solution was possible. Applying the Rankine-Hugoniot shock condition, he was able to remodel the equation and construct the wave profile based on the monotonic solutions of the equation tied together by the shock point. Dressler's model simplify previous Equations 2.25 and 2.26 since the turbulent dissipation of second order is not considered ($\nu_t = 0$). Also, parameter $\alpha = 1$ meaning fully turbulent profile, no sheared zone, and $f(u,h) = u^2/h$:

$$\frac{\partial h}{\partial t} + \frac{\partial (hu)}{\partial x} = 0; \tag{2.30}$$

$$\frac{\partial u}{\partial t} + u\frac{\partial u}{\partial x} + g\frac{\partial h}{\partial x}\cos\theta = g\sin\theta - C_f\frac{u^2}{h}. \tag{2.31}$$

To obtain the roll wave solution, a coordinate transformation is usually

Table 2.2: Values for $\mathrm{Fr}_{\min}$ for different combination of channel cross-section and type of friction. Adaptation from Vedernikov (1945); Chow (1959); Ponce (1991). The variables ϑ and φ are coefficients calculated based on rheological properties of fluid; $f(\gamma)$ is a function dependent on the porosity parameter γ (to be described in the Part II of this thesis), that depends itself on the porosity, permeability and other porous medium characteristics.

Type of friction	Shape of cross-section	$\mathrm{Fr}_{\min}$
Laminar (Herschel-Bulkley)(Maciel et al., 2013)	Hydraulic wide	$\vartheta/(\alpha\vartheta^2 - 2\alpha\vartheta\varphi + \varphi^2)^{0.5}$
Laminar & Porous bed (Power-law)(Pascal, 2006)	Hydraulic wide	$n/(2n+1)^{0.5} f(\gamma)$
Laminar (Power-law)(Ng and Mei, 1994)	Hydraulic wide	$n/(2n+1)^{0.5}$
Laminar (Newtonian)(Ishihara et al., 1954)	Hydraulic wide	$1/(3)^{0.5}$
Laminar (Newtonian)	Hydraulic wide	1/2
Mixed Laminar-Turbulent (25% turbulent Manning)	Hydraulic wide	3/5
Mixed Laminar-Turbulent (25% turbulent Chezy)	Hydraulic wide	8/13
Mixed Laminar-Turbulent (50% turbulent Manning)	Hydraulic wide	3/4
Mixed Laminar-Turbulent (50% turbulent Chezy)	Hydraulic wide	4/5
Mixed Laminar-Turbulent (75% turbulent Manning)	Hydraulic wide	1
Mixed Laminar-Turbulent (75% turbulent Chezy)	Hydraulic wide	8/7
Turbulent Manning	Hydraulic wide	3/2
Turbulent Chezy	Hydraulic wide	2
Turbulent Manning	Triangular	3
Turbulent Chezy	Triangular	4
Any	Inherently stable	∞

performed, having a Lagrangian approach for the wave, using $\xi = x - ct$, so that the system of equations can be rewritten as (Noble, 2004):

$$\frac{\partial}{\partial \xi}\left(h(c-u)\right) = 0; \tag{2.32}$$

$$\frac{\partial}{\partial \xi}\left(hu\,(c-u) + G\frac{h^2}{2}\right) = GhS - C_f u^2, \tag{2.33}$$

where $G = g\cos\theta$ and $S = \tan\theta$. The system can then be condensed in one single differential equation:

$$\frac{\partial h}{\partial \xi} = -\frac{h\left(GS - C_f(ch-K)^2/h^3\right)}{(K/h)^2 - Gh} \tag{2.34}$$

where $K = h(c-u)$ which represent the discharge rate of the flow.

More precise models have been developed (Richard and Gavrilyuk, 2012) with good agreement to experimental results (Brock, 1967), as shows Figure 2.14. Even though roll waves subject have been largely studied, interactions between roll waves and sediment transport are still not completely

understood. Usually when solving two-phase problems, where we have flow and sediment transport, the solution can be reached through de-coupled systems of equations. However, when in roll waves regime, an interaction between both phases seems to takes place and proper numerical solutions can only be obtained through if equations are coupled (Colombini and Stocchino, 2005). Wave of sediments were also observed experimentally (Davies, 1990; Armanini and Recchia, 2006), but no precise mechanism has been defined. On the other hand, recent research from Balmforth and Vakil (2012) shows that particular structures on the mobile bed called cyclic steps can appear when in roll waves regime, but they usually end up stabilizing the flow, thus working as a feedback to surface instabilities. Some similar conclusions were found by Zhao et al. (2015) concerning the feedback of solid particles concentration on flow to waves properties. For a channel with fixed geometry, those researchers observed that flow would not be prone to roll waves generation as soon as a threshold solid concentration of sediment was reached. These examples prove that there are interaction effects between flow dynamics in roll waves regime and sediments transported which cannot be simply addressed.

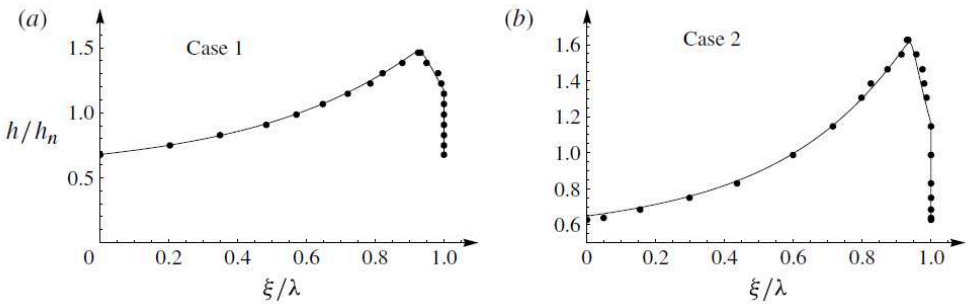

Figure 2.14: From Richard and Gavrilyuk (2012). Comparison of the theoretical solution to the model proposed by the authors (line) and Brock's (Brock, 1967) experimental results (dots) for two different test cases. On the horizontal axis, dimensionless Lagragean longitudinal coordinate scale to the wavelength. On the vertical axis, wave profile scale to mean flow height.

When studying flows in laminar regime, Ishihara et al. (1954) showed through linear stability analysis that instabilities are prone to appear when flow Froude number is greater than a specific value $\mathrm{Fr}_{\min} = 0.5774...$, and further confirmed by Julien and Hartley (1986). In the past 10 years, several mathematical models have been developed on mud and debris flows,

considering the laminar approach, adding up complex features such as arbitrary topography, non-Newtonian fluid rheology and assuming unstable conditions of the free surface (van Asch et al., 2007; Balmforth and Mandre, 2004; Zanuttigh and Lamberti, 2007). Using the same idea as Dressler (1949) but now adding some complexity in fluid rheology, Ng and Mei (1994) constructed the permanent wave profile for laminar power-law fluid flows as nonlinear waves connected by shocks. A linearized stability analysis showed an update of Ishihara's generation criterion, where the dependence of the minimum Froude number with the flow index (n) is highlighted, $\mathrm{Fr}_{\min} = n/(2n+1)^{\frac{1}{2}}$. When $n = 1$ (Newtonian fluid), Ishihara's criterion is recovered thus reassuring this method.

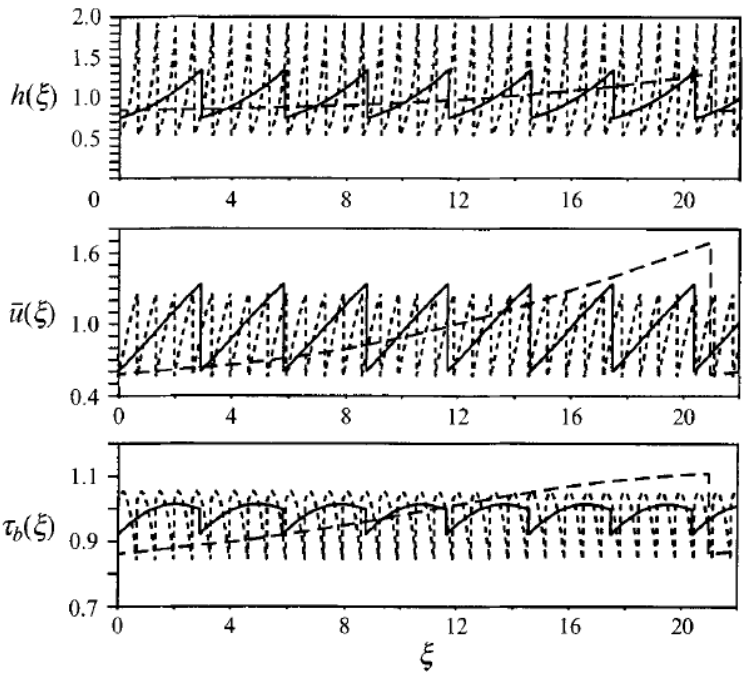

Figure 2.15: From Ng and Mei (1994). Dimensionless profiles for roll waves solution (free surface height, mean flow velocity and bottom shear stress) for a constant index flow value $n = 0.4$ and different Froude number.

Ng and Mei's model brought not only flow height but also mean vertical velocity and bottom shear stress as informations, as shows Figure 2.15. The last parameter is rather interesting when evaluating erosive capacity of such flows. Even though the power-law rheological model includes some non-Newtonian effects, that model is not the best choice to represent muddy

materials such as water-clay mixtures. Through a large experimental approach, Coussot (1994) proved that the Herschel-Bulkley rheological model best fits the profile of this type of material because it uses three parameters to represent the fluid behavior: yield stress (τ_0), flow index (n), and consistency index (K_n). The same conclusion was obtained by Maciel et al. (2009) for Brazilian clay mixtures with water; the behavior of the mixture shows the strong presence of a yield stress value. Coussot (1994) also performed linear stability analysis and obtained a threshold value for Froude number that depends on the fluid rheological parameters; he was also able to qualitatively evaluate that below that value, no instabilities were observed in his experimental bench. The work of Maciel et al. (2013) extends the domain of validity of previous works (Ishihara et al., 1954; Ng and Mei, 1994), corroborating the results found by Coussot (1994), using a more complex rheological model, the same as Coussot (1994), as presentes Figure 2.16. The figure shows also how the non-Newtonian properties control the stability domain, increasing possibility of roll waves appearance.

Nevertheless, other effects had to be also investigated to better approximate theoretical predictions to what is observed in a natural environment. The effect of topography, as mentioned before; porosity of bed; bed scour; and so on. The mobile bed that usually constitute the bottom of natural channels are porous and non flat, composed by rocks and sediments from different sizes. Pascal (2006) was able to revisit the model from Ng and Mei (1994) and redefine stability criteria based on a porous bed parameter γ.

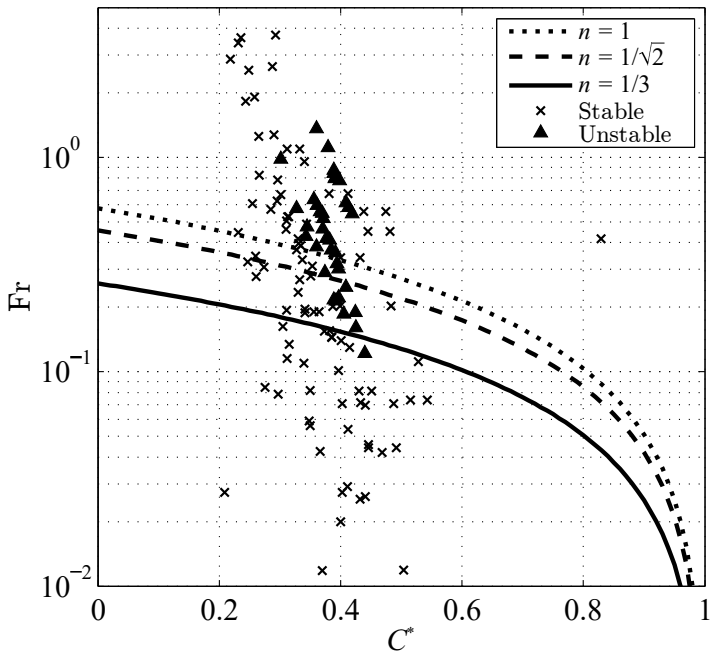

Figure 2.16: The stability criteria found by Maciel et al. (2013) for different values of flow index (represented by lines). Symbols represent experimental results from Coussot (1994): crosses represent flows where no roll waves were noticed, whereas triangles show very likely roll waves configuration at the free surface of flow.

Part I

Sediment transport in runoff flows

Chapter 3

Introduction

Surface runoffs are turbulent flows composed by water with small concentrations of particles entrained. In those flows, sediments like sand are usually transported in bedload. Even though no unifying physical model is able to describe the movement of sediment particles in a fluid flow, studies from the last century (Einstein, 1950; Bagnold, 1977) are still used as valuable references for recent works. Despite of the well-posed problem of measuring the solid discharge and difficulties concerning the representativeness of physical phenomenon, scientific efforts employed so far have led to a vast set of empirical relations. The seemingly reasonable semi-empirical relations broadly used help the understanding on how sediment transport happens in terms of mean values during steady flow configuration.

However, can those empirical laws be directly applied on time-variable problems (non-stationary phenomena) such as tidal bores, dam-break and surface instabilities? In those cases, the level of stress applied to the bottom is not accurately known and should be different depending on the flow itself, thus indicating a non-uniform transport. Taking for example the case for a dam-break, as shows Figure 3.1 from Fraccarollo and Capart (2002). Simplified empirical laws would not be capable to capture the shock wave effect on the mobile bed, and even more the erosional bore formed by directly applying the formulas. They are transitory effects that should be solved in time, thus rendering steady-like formula not easily applied. Another example of such difficulty is given by Ancey et al. (2006), as illustrates Figure 3.2. When close to the imminence of transport, fluctuations of flow could lead to intermittent transport, thus a non-zero net solid discharge, even though the mean bottom shear stress would not be able to produce sediment transport.

Most of the time, the empirical relations employed for steady and uni-

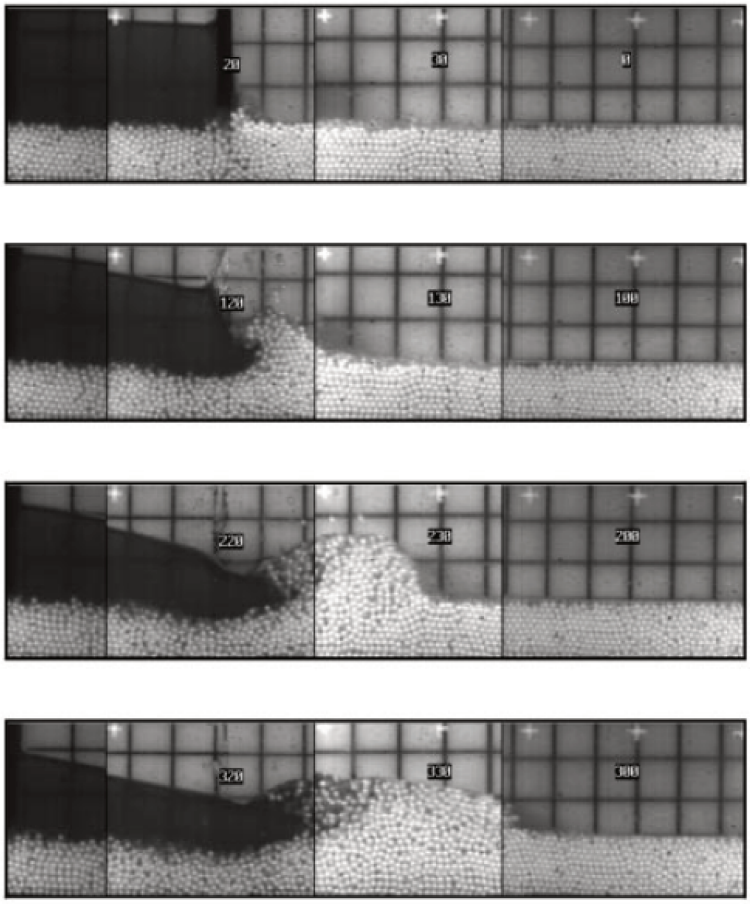

Figure 3.1: Experimental images from Fraccarollo and Capart (2002) which shows dam-break event advancing over mobile bed. The strong non-linear event properties subject a discontinuous profile of sediment transport.

form flow aren't able to satisfactory represent how sediment dynamics would be affected by non-stationary phenomena. One could guess that time-dependent effects such as horizontal accelerations, phase lags, and sometimes even flow velocity fluctuations should not be fit to that approach. Nevertheless, the same empirical relations can be sometimes adapted into numerical solvers. Through discretization of conservation equations, time and spatial numerical solutions can be considered steady and uniform assumptions at time steps/discretization cells. The solution of solid and liquid phase are usually computed separately (Colombini and Stocchino, 2005; Siviglia et al., 2008) using Saint-Venant equations for the liquid phase and Exner equation for the solid phase. Recently the coupling between both

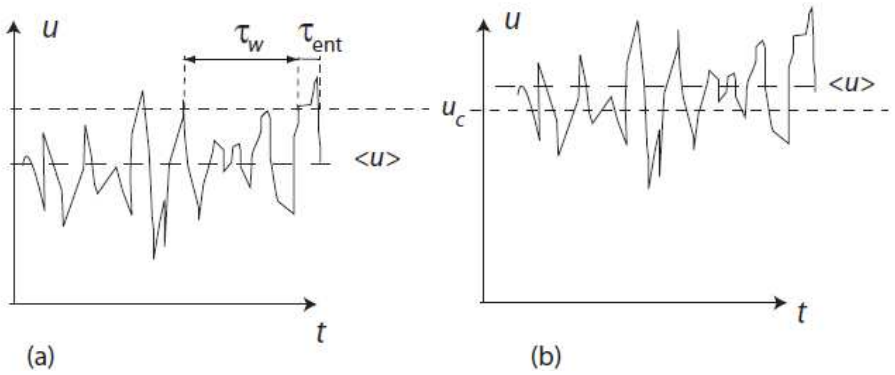

Figure 3.2: Example of discontinuous transport and anomalous diffusion of mass due to non-constant stress applied. Sediment transport can only happen if flow applies enough stress to overcome particle submerged weight, represented by a threshold velocity u_c. Turbulent fluctuations can interfere with continuous state of transport when mean flow is close to particles threshold velocity.

phases solution started to be explored (Audusse et al., 2012; Balmforth and Vakil, 2012), pointing out that a strong interaction between flow and sediment are at stake in some cases.

Hydraulic instabilities represent a vast set of classical Engineering problems where steady and uniform conditions can't be considered. Their presence might difficult or mis-lead the computation of solid discharge. Researchers from Oceanography have dealt with such problem on shore erosion and have been adapting the semi-empirical laws to their problems. Researcher usually modify the empirical functions of sediment transport to employ wave friction, phase lag between waves and sediment transport and other features to better estimate solid discharge (van Rijn, 2007; Kranenburg et al., 2013).

Another example of hydraulic instabilities are roll waves which are fast-moving steep waves with fixed wavelength and amplitude (See chapter 2). Their influence on sediment transport rate is still not well understood but have already been experimentally studied (Davies, 1990). On highly-concentrated flows, Davies (1990) have perceived that such waves changed how transport occurred, generating sediment waves and increasing mean discharge (Figure 3.3(a)). Similar observations have also been made for low-concentrated flows (Armanini and Recchia, 2006). Numerical simulations show that when these hydraulic instabilities appear, flow and sediment

dynamics can no longer be solved separately (Colombini and Stocchino, 2005). Figure 3.3(b) shows the stability diagram for the coupled system (mobile bed-flow), presenting the superposition of bed and flow instabilities for low wavenumbers and high Froude. Even though total discharge seems to change by roll waves presence, neither experiments nor numerical simulations have reached any specific relation and/or value to quantify their effect. The logical conclusion is that there must exists a physical interaction between roll waves and transport sediment that is not taken into account.

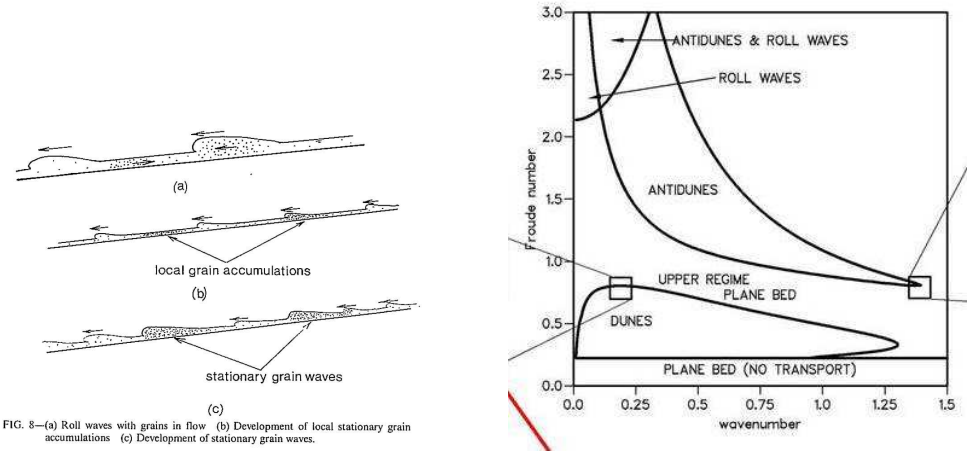

(a) (b)

Figure 3.3: Examples from scientific researches that indicate possibles effects between roll waves instabilities and sediment transport. 3.3(a): Picture from Davies (1990) illustrating how roll waves and sediment waves interact; 3.3(b): stability plot showing that anti-dunes instabilities from mobile bed can appear together with roll waves flow instability (Colombini and Stocchino, 2005).

Considering, for example, the open-channel flow represented on Figure 3.4 by the dark line: an incompressible Newtonian fluid with density ρ and kinematic viscosity ν flows down a channel, with width l_0 and characteristic length L_0, inclined of θ. The flow established is steady and uniform, with characteristics as mentioned in section 2.2. In this case, turbulent dissipation is much greater than viscous one so that the last can be neglected, far from the walls. In the bottom of the channel lies a mobile bed of sediments with density ρ_s and mean diameter D. The capacity of flow to transport sediment is related to the average stress applied to the bottom, τ_b, or friction velocity u_* (Equation 2.9), or Shields number (Equation 2.14).

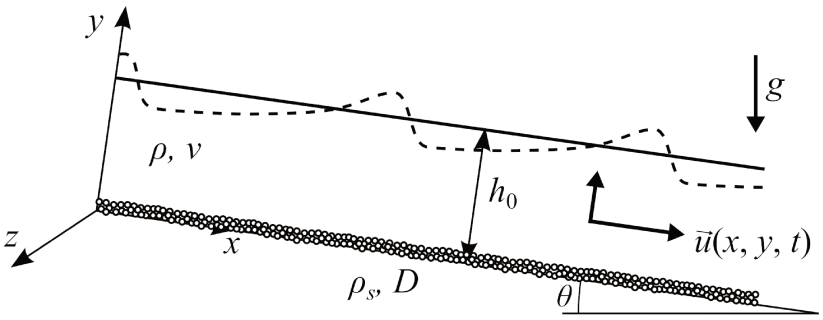

Figure 3.4: Sketch of open-channel flow configuration over mobile bed. Dark line represent free surface in steady and uniform conditions. Dashed line represent free surface instabilities propagating downstream.

Common sediment transport formulas rely on steady and uniform flow informations to estimate the mean value of solid discharge (Meyer-Peter and Müller, 1948; van Rijn, 1984; Wong and Parker, 2006). For bed-load, for example, a representative way of expressing the relation between the solid discharge, represented by q_*, and Shields number is:

$$q_* \propto A(\mathrm{Sh} - \mathrm{Sh}_c)^B, \tag{3.1}$$

where q_* is the dimensionless solid discharge also known as Einstein bed-load parameter $q_* = q_s/(\rho_s\sqrt{(s-1)gD^3})$ with q_s being the bedload solid discharge in weight per unit width per second; and A and B are constants calibrated on flow and mobile bed properties (8 and 3/2 for Meyer-Peter and Müller (1948) and 4.93 and 8/5 for Wong and Parker (2006), respectively).

Nevertheless, it is difficult to apply Equation 3.1 when non-stationary flow properties are important. For example, given a flow with constant discharge q, consider the two following situations: an observer fixed in a position (x_0, y_0) inside the flow so that $0 < y_0 \leq h_0$; an observer fixed at the free surface (x_0, h_0) when surface instabilities are present (dashed line in Figure 3.4). For the first case, depending on the fluctuations scales from turbulence, a certain degree of friction velocity variation would be perceived; for the second one, free surface would culminate in the variation of mean flow characteristics. In both conditions, flow parameters vary with time, implying that bottom shear stress and friction velocity also vary ($\tau_b(t)$, $u_*(t)$, respectively). A first approach that can be done to deal with such problem can be performed by simply inserting a time dependent friction velocity $u_*(t)$ (Nielsen and Callaghan, 2003; van der A et al., 2013) into

Equation 2.14. The classical formulas represented by Equation 3.1 should now read:

$$q_*(t) \propto A(\mathrm{Sh}(t) - \mathrm{Sh}_c)^B, \tag{3.2}$$

where both solid discharge and Shields number are time-dependent.

The discharge $q_*(t)$ is estimated by a nonlinear function to $\mathrm{Sh}(t)$ (threshold value Sh_c and with $B \neq 1$). Small variation on $q_*(t)$ are noticed when $\mathrm{Sh}(t)/\mathrm{Sh}_c \gg 1$ what implies that it might be difficult to identify variations on mean sediment discharge through classical formulae and common measurement systems (gravimetric, p.e.). On the other hand, for $\mathrm{Sh}(t)/\mathrm{Sh}_c \approx 1$, a strong nonlinear effect is at stake and sediments can be taken from its inertial non-movement state to movement with an infinitesimal increment of $\mathrm{Sh}(t)$ (Ancey et al., 2008). This effect would be averaged over time through commonly used measurement systems, thus changing the expected mean value (to respect mean flow properties) and confirming the difficulty in measuring such interaction (Recking et al., 2009; Ancey et al., 2006). Experimental investigation from Recking et al. (2009), for example, show that when $\mathrm{Sh}/\mathrm{Sh}_c < 2.5$ sediment transport shows high variations with time, presenting peak values of solid discharge which are much higher than the mean value. Once again the problem is to measure those variations of bottom shear stress, specially for low Shields number and runoff flows where the desired precision for stress measure would be in order of 10^{-2} Pascals (Amir et al., 2014). To the best of our knowledge, this measurements have not yet been performed/disclosed.

To make such kind of study further possible, two main actions should be undertaken: identify fluctuations of bottom shear stress and/or friction velocity; and identify fluctuations of solid discharge. Despite great efforts that have been undertaken by the scientific community, it seems that there is no systematic evidence from measurements that prove strong relation between time-variable bottom shear stress and solid discharge. Works that follow Kuhnle and Southard (1988) approach, for example, try to study the source of time variability found in the discharge signal, but since the time-scale is considerable high ($\sim$ minute), relating those phenomena to turbulence (that have also much smaller time scales) might be biased. More recently, image analysis have often been used to explore time features from flows and fluctuations on bed load discharge, as it has been explored by Frey et al. (2003). Those authors found that poly-dispersed sediments show greater fluctuations, which were not observed for mono-dispersed materials.

Based on the problem exposed, the aim of this work was to present a set of experimental methods that could allow measurement of both flow dynamic features and solid discharge over time when sediments are transported close to bed (bed load and saltation regime) for low and moderate Shields number.

To study flow dynamics, a Particle Image Velocimetry system (PIV) was employed and a special relation was constructed to obtain friction velocity over time (Ould Ahmedou et al., 2007; Singh et al., 2009; Radice et al., 2009). For the sediment transport, a horizontal sand trap was employed, based on experiments from Ho et al. (2012); Guignier (2014). The methodology here presented could then be used to better understand origins of solid discharge fluctuations.

On chapter 4 the experimental set-up developed is detailed as well as the measurement systems employed to characterize flow dynamics and sediment discharge. Section 4.2 brings a critical analysis of measurements and methods employed which allowed the validation of results presented. chapter 5 the results from a set of time-dependent sediment transport experiments were explored using three main analysis: mean value of solid discharge; spectral analysis of the signal; fluctuations intensities of solid transport. The same chapter presents results for solid discharge experimental runs when disturbances were applied to the flow.

Chapter 4

Experimental method

4.1 Materials and methods

4.1.1 Experimental flume

A small Plexiglas flume (0.2 m wide - l_0, 2.0 m long) was installed over a tilting desk (Figure 4.1). Water flow was employed in a closed system using a constant level reservoir to control discharge (Q = 0.4 l/s maximum). Inlet flow was subdue to a set of nylon grids where undesired large-scale turbulent structures were significantly reduced. In order to impose fixed turbulent properties to the flow, cylindrical obstacles (10 mm in diameter, 2 cm long) were placed after the grids. Downstream the inlet section, flow passed through several parts (Figure 4.1): a fixed bed of 1.35 meter long with test sediment attached; a test zone, where flow measurements were collected in the final 2 cm of the fixed bed; a mobile bed of $L_b = 0.38$ meter long filled with glass beads evenly spread (porosity $p = 0.39$); a horizontal sand trap 0.30 meter long (L_t) where sediment discharge was recorded; and the outlet section.

4.1.2 Flow measurements

Two measurement system were installed in the test zone: A graduated contact needle (CN) and a Particle Image Velocimetry system (PIV). The contact needle was used to measure mean free surface height at different points of the channel to check for the steady and uniform regime of flow. Mean flow height measured $h_{0\mathrm{CN}}$ indicated the mean flow dynamics, thus measurements derived from this method are called global measurements. Measures from PIV system came from a 2D plane positioned in the center

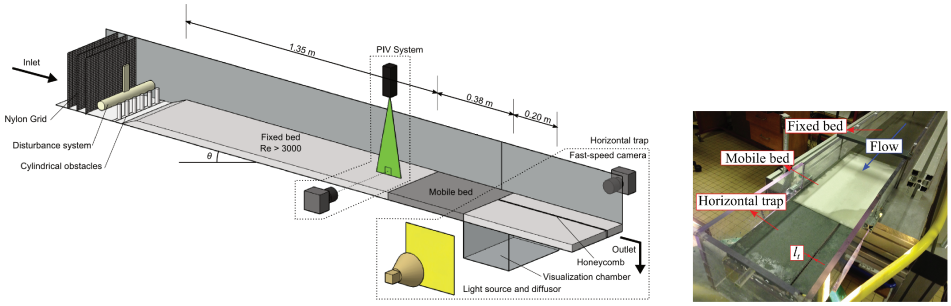

(a) (b)

Figure 4.1: 4.1(a): Sketch of experimental setup, dimensions not to scale; 4.1(b): top view from the experiment.

line of the flow and gave as results the flow field at that position. PIV based measurements are called local measurements. The methodology employed is summarized in Figure 4.2.

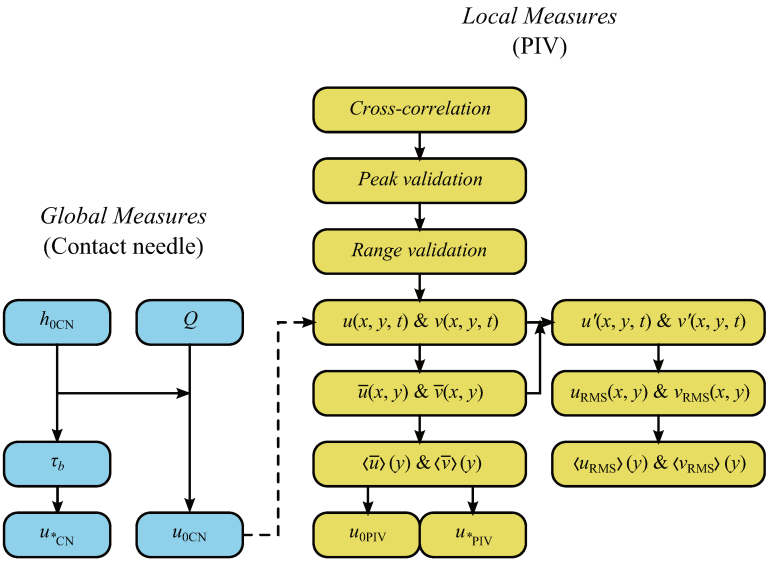

Figure 4.2: Algorithm to obtain flow measurements from contact needle (CN - global) and PIV system (PIV - local).

Global measurements - Contact needle (CN)

Global properties of flow were calculated combining two measures:

- measure of flow discharge Q - through a bucket, precision balance and a chronometer;
- mean flow height through contact needle $h_{0\mathrm{CN}}$;

The flow discharge was constant and then known, with precision e_Q at $\pm 1 - 3\%$. Mean flow height measurements showed precision $\delta_{h_0} = \pm 0.25mm$. These two values combined give the mean flow velocity $u_{0\mathrm{CN}}$:

$$u_{0\mathrm{CN}} = \frac{Q}{l_0 h_{0\mathrm{CN}}}, \tag{4.1}$$

with precision $e_{u_0} = \pm 1 - 7\%$.

For a steady and uniform flow, in shallow water conditions, pressure is hydrostatic. Then, the bottom shear stress reads:

$$\tau_b = \rho g h_{0\mathrm{CN}} \sin\theta, \tag{4.2}$$

and finally the friction velocity can be found using Equation 2.9. The precision of u_* depends on the slope and mean flow height precision and varies between $e_{u_{*\mathrm{CN}}} = \pm 1 - 20\%$. Global measures were further used to calculate the dimensionless numbers that characterize the flow: Reynolds (Equation 2.6), Shields (Equation 2.14) and Froude (Equation 2.29) numbers, previously defined.

Local measurements - Particle Image Velocimetry system (PIV)

The PIV measurement gave information of flow velocity field through an intense double-pulsed laser sheet and a high-speed camera. Such equipment produced a pair of images that was then used to calculate the displacement of packs of seeding particles dispersed in the flow for sub-zones inside the image, called regions of interest (ROI). The calculated displacement was then used to calculate the velocity based on the time between each laser pulse (Time Between Pulses - TBP). The velocity of particles was then assumed equal to flow velocity (Figure 4.3).

Taking into account the global aspect ratio of the flow, PIV measurements employed a rectangular ROI (64 x 16 or 128 x 32 pixels, depending on seeding quality). The effective area of measurement was 1664 x 1280 pixels, corresponding to 11.12 mm x 9.03 mm. The open-channel flow was seeded with silver-coated hollow glass spheres with a diameter around 10 μm. The particles were illuminated by the thin laser sheet created by a single-head Laserglow laser coupled to a cylindrical lens. The laser was operated at a

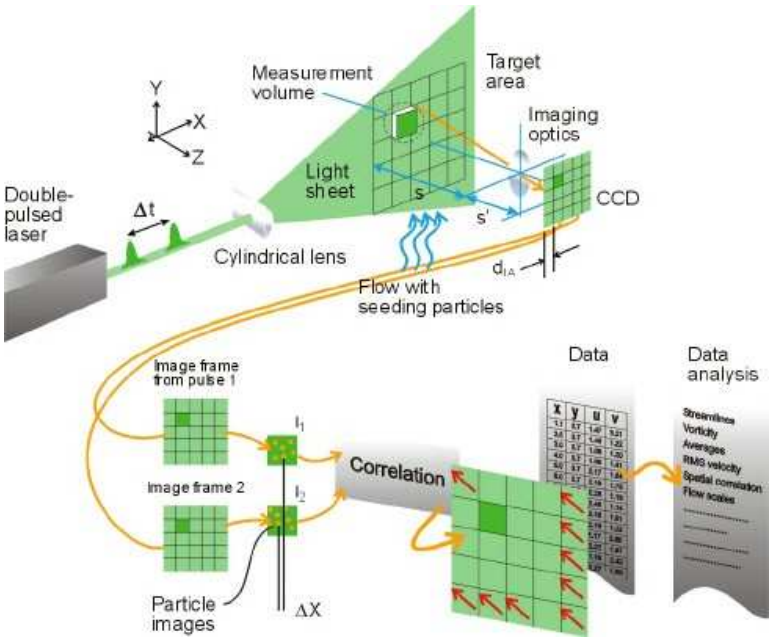

Figure 4.3: Principle of Particle Image Velocimetry (PIV) technique functioning. A double-pulsed laser sheet crosses a ROI of the flow, which then is recorded through high-speed camera. The pair of image is used to calculate the displacement of seeding particles in the flow, and respective velocity. Their velocity is assumed equals to flow velocity. (DANTEC Dynamics)

wavelength of 532 nm and double-pulsed at 7 Hz, with each pulse delivering approximately 5-15 mJ of energy, sufficient enough to illuminate the seeding particles. The scattered laser light from seeding particles was recorded with a 2048 x 2048 pixel CCD camera from Dantec Dynamics, during 100-300 μs of exposure time, depending on estimated mean flow velocity. The time separation between the laser pulses (TBP) was also adjusted according to global mean flow velocity $u_{0\mathrm{CN}}$.

Cross correlation was then firstly applied to images (Keane and Adrian, 1993) by software DynamicStudio (Dantec Dynamics A/S). Secondly, peak and range validation of vectors were employed. The minimal signal/noise ratio used was 1.2. Range validation of vector were based on estimative of mean flow velocity $u_{0\mathrm{CN}}$. Then, for longitudinal velocities, the range accepted varied from $-0.20u_{0\mathrm{CN}}$ to $1.75u_{0\mathrm{CN}}$ and for vertical velocities from $-0.50u_{0\mathrm{CN}}$ to $0.50u_{0\mathrm{CN}}$. To avoid statistical bias, only valid vectors were used for flow velocity field (u, v), with $u = u(x, y, t)$ the longitudinal component and $v = v(x, y, t)$ the vertical velocity component. For each run, we

acquired at least 1000 images, and the total amount of valid vectors used for each position in y was approximately 3000. Precision of PIV measurements e_{PIV} was calculated based on equipment characteristics, as suggests (Lazar et al., 2010). For our equipment and mounting, $e_{\mathrm{PIV}} = 4.5\%$.

Since the flow produced was preferentially in the longitudinal direction x, the velocity profile that should have established depended mainly on vertical coordinate y. Each velocity component (u, v) was separated in mean and fluctuating components through data processing in Matlab:

$$u(x, y, t) = \bar{u}(x, y) + u'(x, y, t); \tag{4.3}$$

$$v(x, y, t) = \bar{v}(x, y) + v'(x, y, t); \tag{4.4}$$

$$\bar{u}(x, y) = \frac{1}{N_t} \sum_t u(x, y, t); \tag{4.5}$$

$$u'(x, y, t) = u(x, y, t) - \bar{u}(x, y); \tag{4.6}$$

where N_t is the number of valid vector from initial to final time step. Afterwards, the average profile of mean flow velocity $\langle \bar{u} \rangle(y)$ was calculated averaging through longitudinal coordinate x:

$$\langle \bar{u} \rangle(y) = \frac{1}{N_x} \sum_x \bar{u}(x, y), \tag{4.7}$$

with N_x is the number of valid vector on the calculated zone along x. Velocity field standard deviation $u_{\mathrm{RMS}}(x, y)$ was calculated as:

$$u_{\mathrm{RMS}}(x, y) = \sqrt{\frac{1}{N_t} \sum_t u'^2(x, y, t)}, \tag{4.8}$$

which can then be also used to calculate the average profile for standard deviation of velocity field:

$$\langle u_{\mathrm{RMS}} \rangle(y) = \frac{1}{N_x} \sum_x u_{\mathrm{RMS}}(x, y). \tag{4.9}$$

The same procedure was applied to vertical component of velocity. Mean flow height and velocity can be estimated based on velocity profile through integration of $\langle \bar{u} \rangle(y)$ and flow discharge (Equation 2.1), thus giving $h_{0\mathrm{PIV}}$

and $u_{0\mathrm{PIV}}$.

The flow average velocity $\langle\bar{u}\rangle(y)$ was transformed in wall coordinates (Equations 2.11b and 2.11a) using the global value for friction velocity $u*\mathrm{CN}$. Then, the profile was fitted to the universal solution for turbulent flows (Equation 2.13) and the value for the friction velocity $u_{*\mathrm{PIV}}$ was refined. Quality of fluctuation field was verified by turbulent intensities $u^+_{\mathrm{RMS}}(y) = \langle u_{\mathrm{RMS}}\rangle(y)/u_{*\mathrm{PIV}}$ and $v^+_{\mathrm{RMS}}(y) = \langle v_{\mathrm{RMS}}\rangle(y)/u_{*\mathrm{PIV}}$, compared to experimental results from the literature.

Since the proposal of this work was to study sediment transport over time, friction velocity also needed to be determined as function of time. A method derived from Ould Ahmedou et al. (2007) was here adopted which consisted in founding a relationship between the flow velocity at some point and mean friction velocity. Ould Ahmedou et al. (2007) work proves that, for eolian sediment transport, the discharge is correlated with the instantaneous velocity in an arbitrary position close to the bed. In this way, based on $\langle\bar{u}\rangle(y)$, a vertical coordinate y_0 was chosen and values from the velocity field $\langle u\rangle(y_0, t)$ were correlated to the average friction velocity $u_{*\mathrm{PIV}}$. This methodology is further evaluated on section 4.2.

4.1.3 Sediment transport measurement

Test-sediment used during experimental tests were glass beads with mean diameter $D_{50} = 200\mu$m (dispersion between 150 and 250 μm) and density ρ_s of 2430 kg/m^3. These particles have terminal fall velocity $v_s \sim 0.02$ ms^{-1}. Figure 4.4[1] shows results from particles grain size distribution made through laser diffraction method on two samples: brand new particles; and used particles. Histograms show that no substantial difference is noticed on particles distribution size. Critical value for Shields (Sh_c) calculated through empirical values from the literature (Paphitis, 2001) points out a value of 0.062 ($u_{*c} = 0.013$ m/s) and lower and upper limits equal to 0.057 and 0.088 (-9%; +40%) respectively.

For the sediment discharge measurement, two measurement system were also employed: a filtering fabric positioned at channel output; and the horizontal trap (Figure 4.5). The horizontal trap was designed based on wind tunnel experiments from Ho et al. (2012) and internal water flow from Guig-

[1]Acknowledgment: Thanks to Jean-Luc Metayer and Siham Kalim-Bernard for their support in performing such measures.

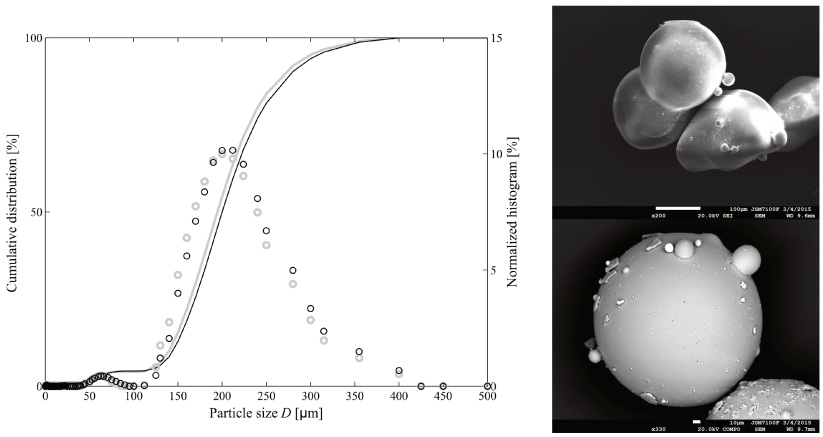

Figure 4.4: Histogram for sediment used in experiments. Lines represent cumulative distribution, circles normalized histogram. Gray lines represent brand new glass spheres, dark lines represent used ones. To the right, MEV images for particles showing regularity of shape.

nier (2014) where such kind of trap was used to study sediment transport in saltation regime. This method is quite interesting because it evaluates not only sediment discharge but also their scattering in space allowing differentiation of transport modes. This method was here adapted and allowed basically the same informations to be acquired with an extra temporal description.

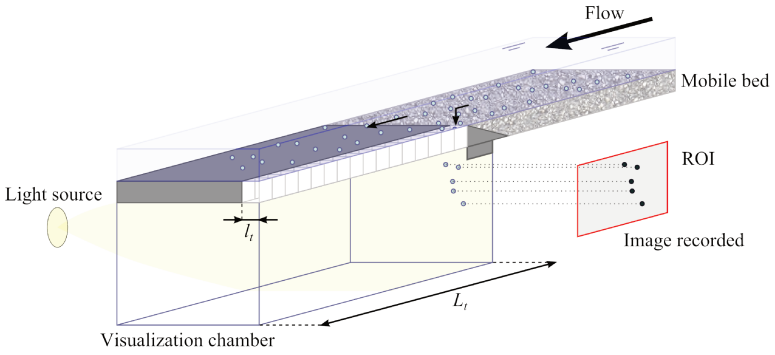

Figure 4.5: Schematic representation of horizontal trap section. For sake of visualization, illustration represent a longitudinal cut following the trap.

Global measurements - Total mass weighting (W)

The global measurement of solid discharge consisted on weighing the sediment mass transported during the experimental run. From the filter installed at channel outlet, particles transported and not trapped were collected. Adding the trapped mass to such value, the global mean discharge $\bar{Q}_{s\mathrm{W}}$ was estimated dividing the mass by the total time of the experimental run.

4.1.4 Local measurements - Particle Tracking Velocimetry System (PTV)

The horizontal trap had a small width (4.1(b), $l_t = 3.9$ mm), which represented part of the total solid discharge. In this way, measurements from the trap were local. Particles not trapped were transported downstream where the filtering fabric was installed allowing to capture all transported particles. Particles move over mobile bed by rolling, sliding or saltating, with trajectories that depend on the transport mode (as explained in chapter 2. Minimum sand trap length was designed based on particles longest displacement along x, i.e. the deposition length L_{dep}, which is related to particles highest jumps during their entrainment. In the general case, particles maximum height is proportional to the mean free surface. So,

$$L_{\mathrm{dep}} \propto \frac{u_0}{v_s} h_0. \tag{4.10}$$

However, for bed load transport, particles vertical movement scales with particles diameter D (Fourrière et al., 2010) which leads to the following relation:

$$L_{\mathrm{dep}} \propto \frac{u_0}{v_s} D. \tag{4.11}$$

Considering a mean flow velocity $u_0 = 0.2$ ms^{-1}, the maximum deposition length is roughly 2 mm, meaning that no drawback should be noticed by the measurements performed in the trap ($L_t = 0.30 \gg L_{\mathrm{dep}} = 0.002$ m).

Particles entrained by flow reached the trap, fell through the honeycomb and arrived in the visualization chamber. They were illuminated by a diffused light source positioned in the opposite side of the camera. Shadows from particles were recorded with a 2048 x 2048 pixel CCD high-speed camera sampling at 100 frames per second, which gave a time between each frame of $\Delta t = 10$ ms. Exposure time was settled at 1 ms. Raw images were recorded in grayscale as shown on Figure 4.6. Images were then

processed through a Particle Tracking Velocimetry program developed in Matlab (PTV) to compute solid discharge.

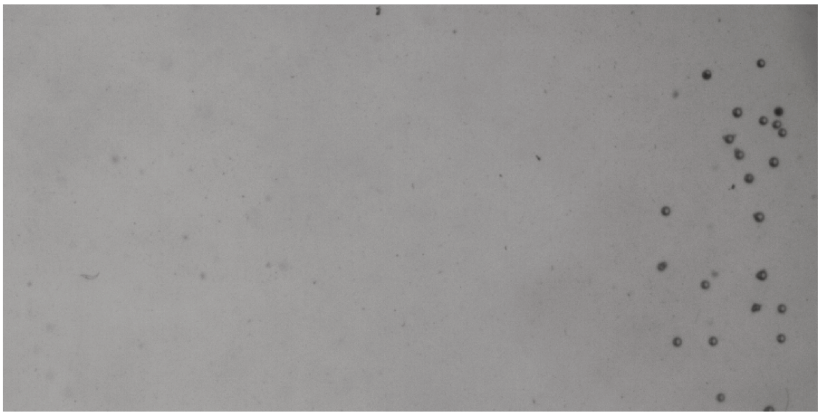

Figure 4.6: Raw image of horizontal trap from high-speed camera.

Images obtained at the counting chamber were processed with Matlab image processing toolbox. The method here employed was similar to the one used by Frey et al. (2003). Original images were cropped into an image I_0 to eliminate undesired features from experimental set-up. Since different experimental runs can have different light properties, images were enhanced to standardize images contrast and optimize particle detection algorithm. To do so, a linear adjust of contrast was performed using the background image B (when no shadows of particles are present) as:

$$I_1 = I_0 - B, \tag{4.12}$$

$$I_2 = \frac{255}{\max(I_1) - \min(I_1)}(I_1 - \min(I_1)). \tag{4.13}$$

After image enhancing, images were transformed into binary using Canny edge detection filter (Canny, 1986). For the threshold required in the edge filter, Otsu's threshold method (Otsu, 1979) was applied following indication of Fang et al. (2009). Morphological operations were performed on the binary image. Firstly, the operation of closing was performed using a structural binary element that allow optimal closing of particles shadow edges. Those edges were then filled and consecutive operations of erosion and dilatation were performed to eliminate spurious objects and dust particles. Examples of raw, enhance and binary image are shown in Figure 4.7.

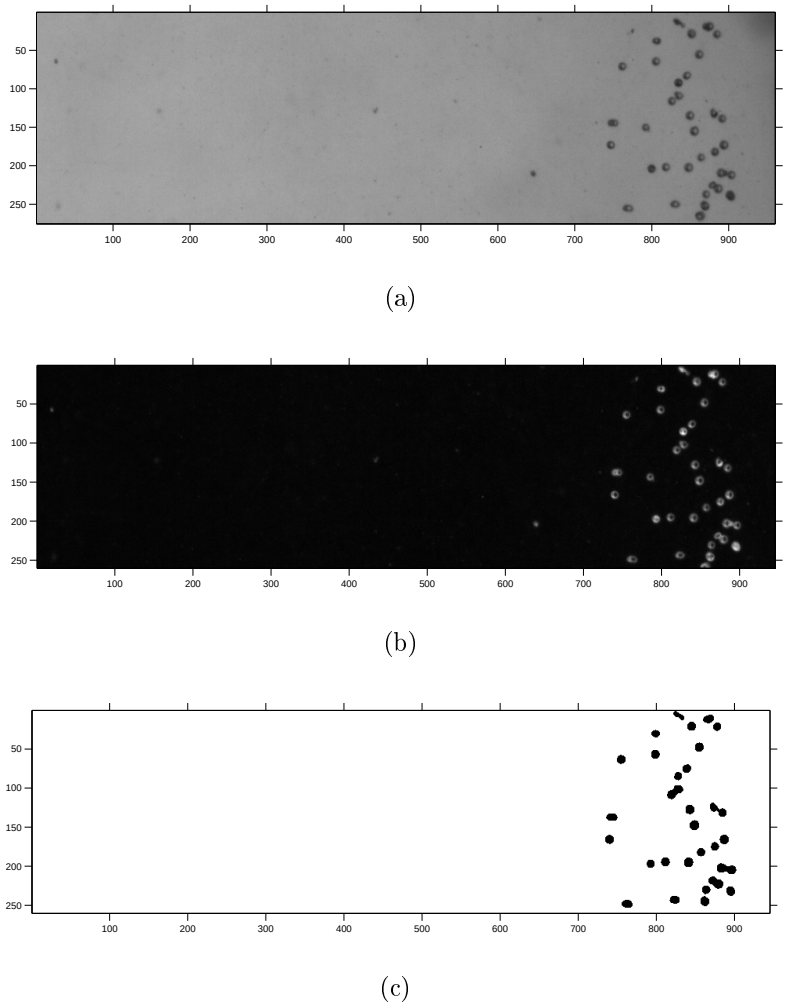

(a)

(b)

(c)

Figure 4.7: Images from an experimental run. 4.7(a): original image in gray-scale obtained from camera acquisition; 4.7(b) enhanced image; 4.7(c) binary image showing shadows from particles.

For each image k taken from the experimental run, each particle p_i^k was identified by means of their position vector $\vec{r}_i^k$ and their diameter D_i^k. Based on particle displacement vector $\Delta\vec{r}_i^k = \vec{r}_i^k - \vec{r}_i^{k-1}$ (Figure 4.8) during a step time Δt, their individual velocity $\vec{v}_i^k$ was calculated as

$$(u_i^k, v_i^k) = \frac{\Delta\vec{r}_i^k}{\Delta t}. \tag{4.14}$$

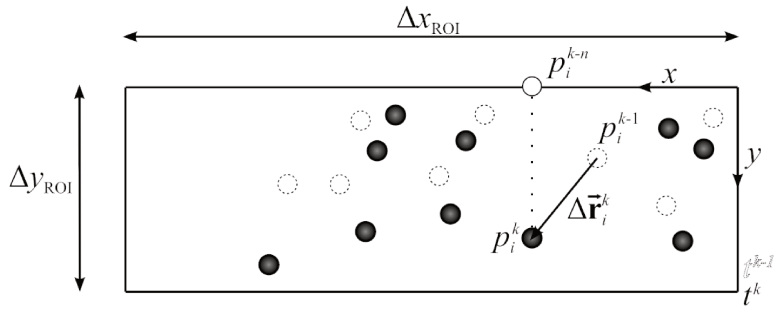

Figure 4.8: Scheme of particle counting inside the ROI. Open circle denotes particles in time step t_{k-1} and black circle denotes particles Δt seconds after, time step $t_k = t_{k-1} + \Delta t$.

Particles mass were calculated based on the measured diameter:

$$m_i^k = \frac{\pi \rho_s}{6} D_i^{k3}. \tag{4.15}$$

Different methods can be employed to calculate the particles discharge and each one of them is somehow related to the other (Heyman, 2014). Two different methods based on particles velocity can be defined: one based on average fall velocity; and another based on individual particle velocity. In this work, only the second one was used due to grain-size distribution.

Mean particles velocity

The basic methodology that can be developed assumes that particles are falling inside the counting chamber at the same constant speed v_s^k for each image. The total mass per image $M(t^k)$ is given by:

$$M(t^k) = \sum_{i}^{N_p} m_i^k, \tag{4.16}$$

where N_p is the total amount of particle on image in time t_k. The discharge is then given by:

$$Q_s(t^k) = \frac{1}{\Delta t_{\mathrm{esc}}^k} M(t^k), \tag{4.17}$$

where $\Delta t_{\mathrm{esc}}^k$ represents the mean time taken by such mass to vertically travel the ROI, which we called particles escape time:

$$\Delta t_{\mathrm{esc}}^k = \Delta y_{\mathrm{ROI}} / \bar{v}_s^k, \tag{4.18}$$

where $\bar{v}_s^k$ is the mean particles fall velocity:

$$\bar{v}_s^k = \frac{1}{N_p} \sum_i^{N_p} v_{s_i}^k. \tag{4.19}$$

Then, the discharge is:

$$Q_s(t^k) = \frac{1}{\Delta y_{\text{ROI}}} M(t^k) \bar{v}_s^k. \tag{4.20}$$

The uncertainties of measures can then be calculated as:

$$e_{q_s} = \sqrt{{e_{m_p}}^2 + {e_{v_s}}^2 + {e_{\Delta y_{ROI}}}^2} \tag{4.21}$$

Weighted-mean particles velocity

Since particles falling velocity depend on the particle mass (proportional to particle diameter, Equation 2.18), a more precise computation of solid discharge can be performed using a weighted-mean velocity as:

$$\bar{v}_s = \frac{1}{M(t^k)} \sum_i^{N_p} m_i^k v_{s_i}^k \tag{4.22}$$

and then the discharge would be

$$Q_s(t^k) = \frac{1}{\Delta y_{\text{ROI}}} M(t^k) \bar{v}_{ss}^k = \frac{M(t^k)}{\Delta y_{\text{ROI}} M(t^k)} \sum_i^{N_p} m_i^k v_{s_i}^k, \tag{4.23}$$

$$Q_s(t^k) = \frac{1}{\Delta y_{\text{ROI}}} \sum_i^{N_p} m_i^k v_{s_i}^k. \tag{4.24}$$

This second method was adopted as the main source of results. The analysis that will be shown on the next section employed this method with a critical analysis of the results.

4.1.5 Wave generator

Upstream the fixed bed, between the nylon grids and cylindrical obstacles, a wave generator system was positioned used to disturb the free surface of the flow at a constant frequency. A detailed side view of the system is shown on Figure 4.9. An electronic function generator was coupled to a power amplifier which then excited a solenoid. This solenoid was assembled

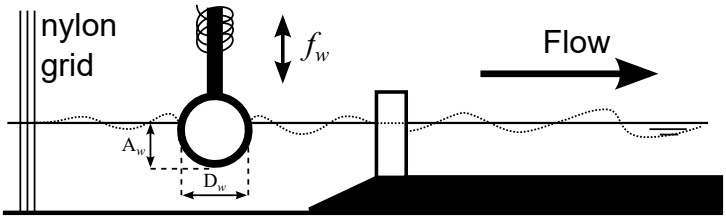

Figure 4.9: Schematics of the side view from the upstream part of the channel where the disturbance system is positioned.

to a rod with diameter D_w that disturbed the free surface of the flow at the selected frequency f_w. The rod enters and exits the flow at a certain depth A_w, kept constant for every experimental run. The disturbance frequency was controlled so it was not a multiple of others acquisition systems frequency. The frequency f_w was also controlled so more than one wavelength is present over the porous bed:

$$f_w > \frac{u_0 + \sqrt{gh_0}}{L_b}. \tag{4.25}$$

4.2 Critical analysis of measurements

4.2.1 Sediment transport test

To evaluate the PTV methodologies described in subsection 4.1.4, a set of binary images was constructed, where the size of "particles" and their velocities were imposed. In those images, as exemplifies Figure 4.10, only two dimensions are considered, so the volume of particles is equal to their surface. For sake of simplicity, for the tests that will follow density is taken as $\rho_s = 1$ (mass = volume).

Influence of Δy_{ROI}

The transformation of discrete sediment discharge to continuous domain would required infinitesimal scales of time step Δt and ROI. Such transformation is limited by sediment itself (discrete particles with finite size). To determine the effect of Δy_{ROI}, a numerical analysis was conducted to see how transport rate would change as this parameter grows as function of particles mean displacement length $v_s \Delta t$.

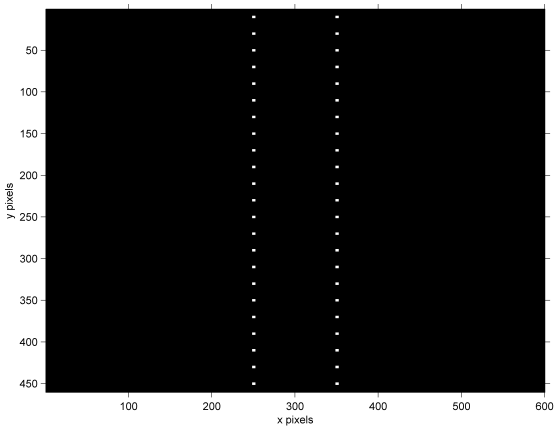

Figure 4.10: Artificial image created to test PTV methodology for solid discharge calculation.

To evaluate how Δy_{ROI} affected the results, time series of constant images were constructed, each series presenting a different size image with the same pattern of particles. Figure 4.11 shows one example of such series at intervals of one second ($\Delta t = 1$ s). Particles had the same size (12 pixels) and velocity (20 pixels/s). The sequence looks like a freeze video, but in fact particles velocity are constant, and their trajectory are vertical and straight. The discharge can then be intuitively calculated as 2 particles per second enter the ROI, then $q = 24$ pixels/s.

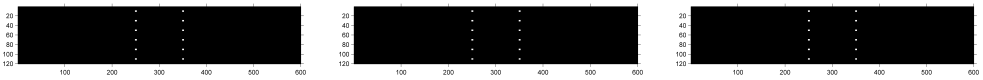

(a) t^k. (b) $t^{k+1} = t^k + \Delta t$. (c) $t^{k+2} = t^k + 2\Delta t$.

Figure 4.11: Artificial sequence type A created to test PTV methodology dependence on ROI size.

Making the Δ_{ROI} vary for a well-behaved event, it can be observed that there is a minimal ROI necessary for computed discharge to be equal to the correct value[2]. We defined then a minimum size for images equal to three times the mean displacement of sediment particles ($\Delta y_{\mathrm{ROI}} > 3 v_s \Delta t$) given the time between each image acquired Δt. Using data from an experimental runs (gb1-3), the same behavior was detected, although fluctuations were

[2]Remark: Δy_{ROI} was employed so that no particles were sliced in the image limits. Such step is automatically taken during the image processing stage.

perceived using the method explained in subsection 4.1.4, thus increasing the minimum size of the images ($\Delta y_{\text{ROI}} > 10 v_s \Delta t$). The results are shown on Figure 4.12.

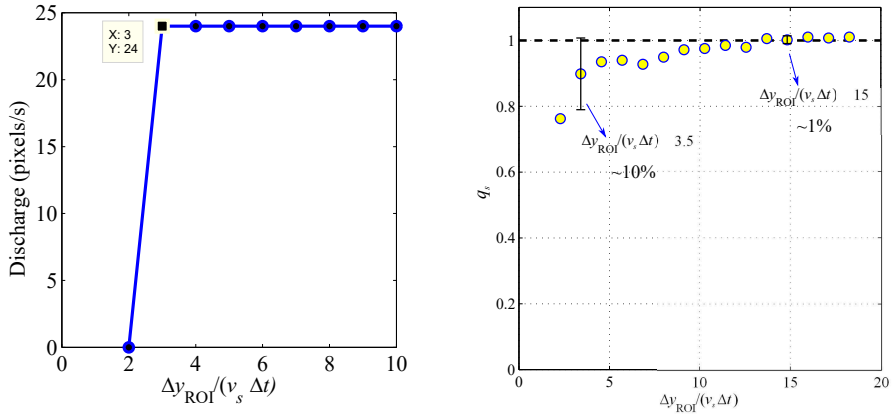

(a) (b)

Figure 4.12: Dependency of sediment discharge on vertical length of ROI Δy_{ROI}. 4.12(a): well-behaved artificial run; 4.12(b): experimental runs gb1-3.

As the ROI size increased, more particles could be counted and the effect that was perceived was a smoother signal of solid transport, as can be observed in Figure 4.13. In this work we chose $\Delta y_{\text{ROI}} \approx 12 v_s \Delta t$.

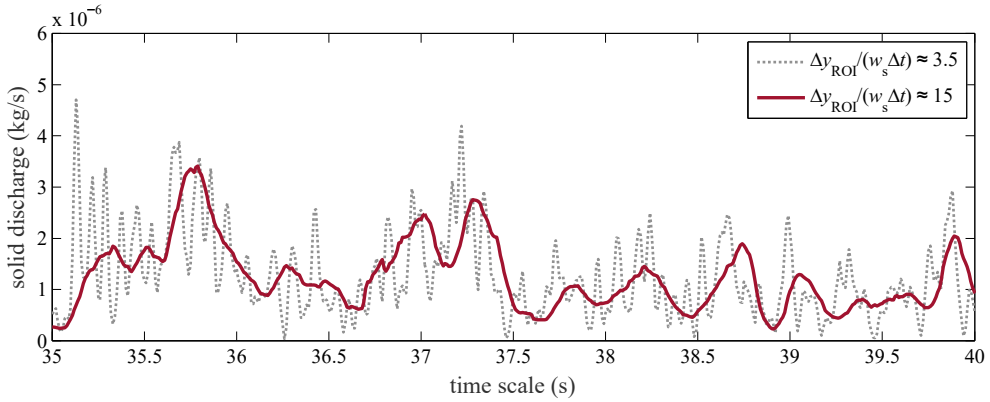

Figure 4.13: Example of solid transport signal from a same experimental run using different ROI.

4.2.2 Grain-size distribution through images

Quality of geometric properties from particles detected through image technique can be evaluated comparing results to the typical grain-size distribution for test-sand. The probability density function of particles diameter was calculated and compared to the one calculated from laser grain-size distribution (Figure 4.14).

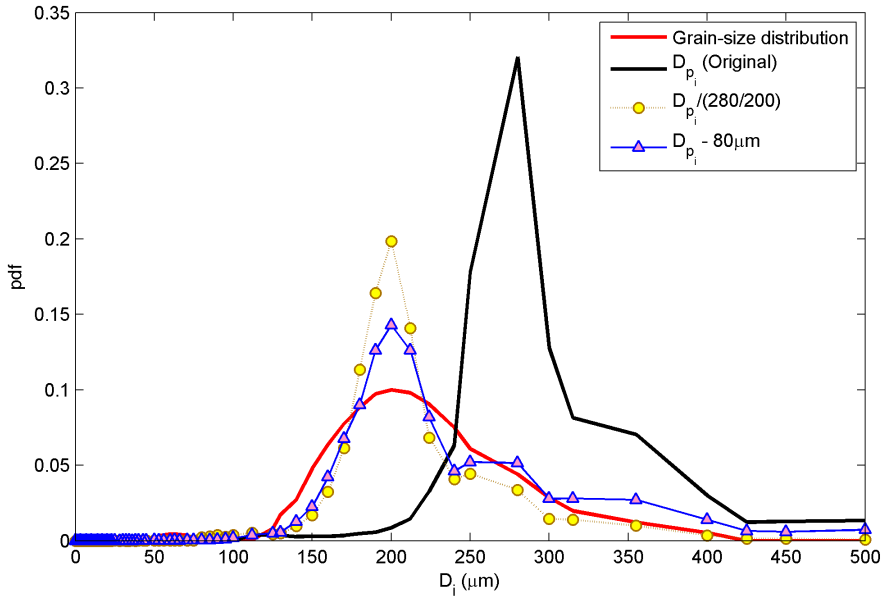

Figure 4.14: Comparison between grain-size distribution of sediment particles obtained from laser grain-size distribution and imagery technique. The red line indicates the probability density function obtained from laser grain-size distribution. Black line represents measurements from image technique employed. Yellow circles and purple triangles show different corrections that can be employed to correct particles diameter.

The image processing techniques may present bias during the process which cannot be easily controlled. Depending on the lightning conditions and on the image processing technique employed, a halo might appear around the contour of a particle, which produce a particle with a greater diameter, as shows Figure 4.15. As a result, this feature produces a PDF[3] which is displaced, as can be observed in Figure 4.14. To correct such bias, we estimated the mean value of particles diameter computed through image

[3]Probability Density Function

processing technique, and subtracted that value from all particles diameter, before calculating the solid discharge, thus displacing the peak observed in the computed PDF to the measured one.

Figure 4.15: Pictures showing different stages of image processing technique where the artificial increase in diameter is observed.

4.2.3 Qualitative analysis and temporal partitioning of signals

A preliminary qualitative analysis have to be done on signals to extract the general aspects of $q(t)$ as shown, for example, in Figure 4.16. Given how the experiments were performed, different parts of the signal present completely different dynamics and thus must be separated accordingly.

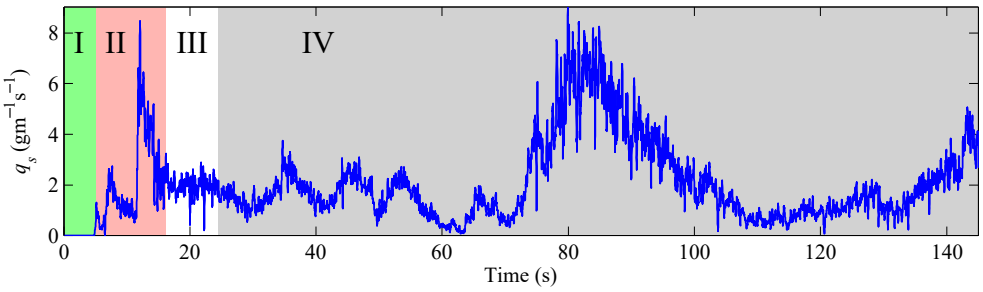

Figure 4.16: Solid discharge for experimental run gb2-2 as function of time. Signal is sectioned following the classification described in subsection 4.2.3.

In every experimental run, up to four stages of solid transport can be identified:

I Experimental initiation (no substantial transport). This stage is present in most of the experimental runs and corresponds to the initialization of the run, where both acquisition system (PIV and PTV) are turned on, and the downstream dam is released. For small discharges and slopes, flow takes time to reach uniform and permanent configuration thus leading to an usually short time where no considerable solid

transport happens.

II Dam-break transport (first surge of sediments). This stages corresponds to the abrupt change in friction induced by the release of the dam. Depending on the flow discharge and channel slope, this wave can be considerably important, as shows Figure 4.16.

III Steady transport - q_s^{III}. Usually, after the first wave, the sediment transport can be assumed "steady". During this part of the signal, we consider that the mobile bed is flat. In this way, the bottom shear stress should be approximately the same to the one found at the fixed bed. Mean and fluctuated values can be calculated at this point. The time duration of this part can vary depending on the Shields number. For high Shields, this part should be smaller in time, and sometimes cannot be identified.

IV Non-stationary transport (bedform) - q_s^{IV}. Flow condition dictate whether bedforms should appear in the mobile bed and how fast they will travel. This will lead dunes and ripples to fall inside the trap, drastically changing the solid discharge measured. For low and moderate Shields number, this stage can be identified after the part III, when bedforms start to reach the trap. For high Shields number, the separation between the parts III and IV is not clear, and then only the part IV is considered after part II.

As it is, the first stage could be detected by simple observation of the given solid discharge signal. The other three stages could be found qualitatively but using a cumulative value for the mean transport can improve the judgment:

$$q_{sc}(t) = \frac{1}{N_t} \sum_{i=1}^{N_t} q_s(t). \tag{4.26}$$

The section was done choosing two time stamps and observing the behavior of two cumulative mean values: one starting from the initial time (positive direction of time); and another from the end time (negative direction of time). The uncertainty of the equipment was plotted as a shade zone around q_{sc}. If both signals q_{sc} cross, this means that initial and end time stamp chosen select a q_s^{III} zone of solid transport. Figure 4.17 shows an example using original initial and end timestamps.

It is possible to inspect the image and identify that between 10 and 30 a constant value was reached. In the remaining signal there would the

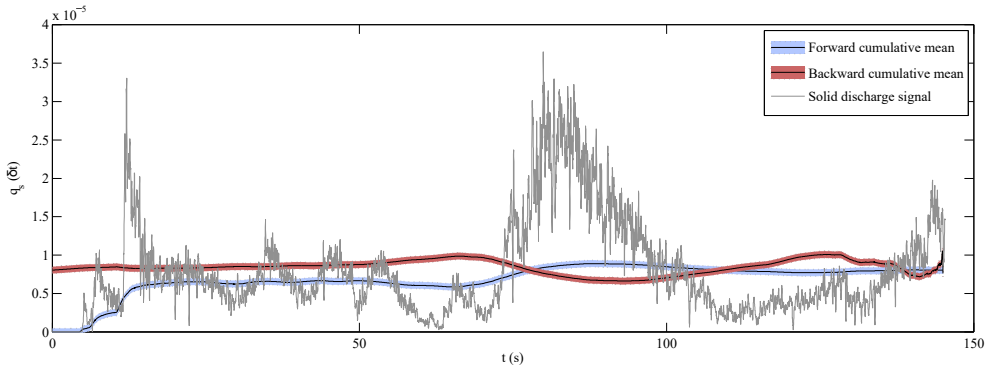

Figure 4.17: Cumulative mean solid discharge for experimental run gb2-2 as function of time window. Gray shaded zone indicate uncertainties for cumulative mean in the positive direction of time, and red shaded zone indicate the same property in negative direction of time.

possible effects of bedforms into the transport. So, changing the initial and end timestamps, q_{sc} could be inspected until satisfactory results were achieved as shows Figure 4.18. Zone II was identified between 15 and 25 seconds, and zone IV from 25 seconds forward. Finally, as time stamps were found, signal was broken apart in the stages mentioned before, as presents Figure 4.16.

4.2.4 Measurements of mean solid discharge

To inspect the quality of solid discharge measurement, we compared the local and global values (from gravimetric and PTV methods), as presented in Figure 4.19. Such relation however depends on the quantity of sediment in the ROI.

To properly explore such information, the limitations of the system (Figure 4.20) must be understood:

A - whenever particles fall side by side, only one shadow is perceived on images. This lack of information leads to a reduced discharge rate by counting less particles, thus smaller mass, and smaller flux;

B - when particles numbers are high, one particle might come across the path of another. This might lead to the computation of a smaller particle velocity, thus a smaller flux.

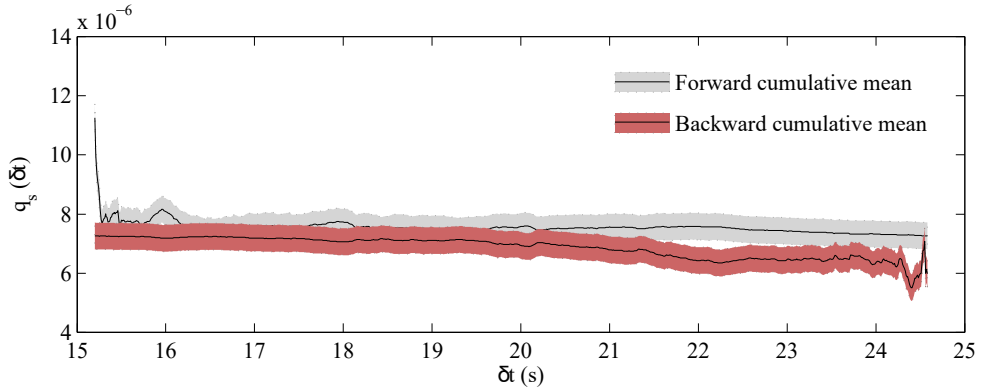

(a) : q_s^{III}

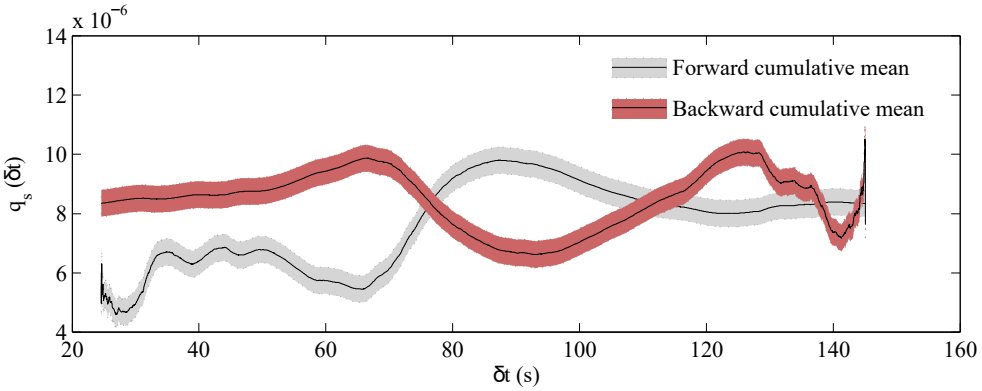

(b) : q_s^{IV}

Figure 4.18: Cumulative mean solid discharge for experimental run gb2-2 sectioned in: 4.18(a) q_s^{III}, between 15 and 25 seconds and 4.18(b) q_s^{IV}, from 2(seconds and forward.

To estimate the number of particles in the image where the effects A and B can affect the measurement, we calculated particles mean displacement,

$$\bar{\Delta r} = \bar{v}_s \Delta t, \tag{4.27}$$

where $\bar{v}_s$ is the mean particle free fall velocity inside the trap ($v_s \approx 4$ cm/s). When in bedload, particles are concentrated in the first 5 mm of the trap ($\Delta x_{\mathrm{ROI}_{sb}} = 5$ mm). Considering an organized distribution of particles in

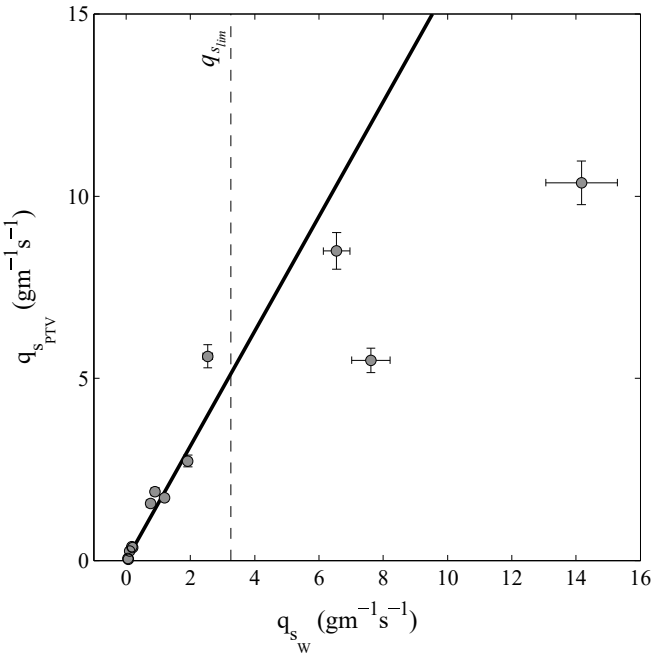

Figure 4.19: Comparison between different transport rate measurements: q_{s_W} represented the total weighted mass of particles displaced during the experimental run; $q_{s_{PTV}}$ represented the measured solid discharge through PTV method. The dashed line represent the solid discharge limit value where particles quantity can start to affect the solid discharge assertiveness. The solid line indicate the relation between both measured solid discharges under the limit of assertiveness.

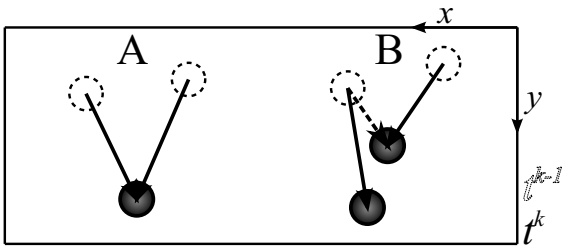

Figure 4.20: Limitations found in the PTV method employed to calculate sediment discharge. Solid arrows illustrate real displacement of particle. Dashed arrow indicate calculated displacement.

the ROI, the limit number of particles in the image should be:

$$N_{p_{lim}} = \frac{\Delta x_{\mathrm{ROI}_{sb}} \Delta y_{\mathrm{ROI}}}{(v_s \Delta t)^2}. \tag{4.28}$$

The limit discharge $Q_{s_{lim}}$ is proportional to that number:

$$Q_{s_{lim}} = \frac{N_{p_{lim}} \bar{m}_p \bar{v}_s}{\Delta y_{\text{ROI}}}. \tag{4.29}$$

For our case, $q_{s_{lim}} \approx 3.26$ gm^{-1}s^{-1}, as indicate the dashed line in Figure 4.19. This value is indicated in Figure 4.19 by the vertical dotted line. Finally, fitting a curve for the solid discharges smaller than $q_{s_{lim}}$, we obtained the function:

$$q_{s_{PTV}} = 1.576 q_{s_W}, \tag{4.30}$$

with correlation coefficient $R^2 = 0.94$. To correct the mean value for time-dependent discharges beyond the limit $q_{s_{lim}}$, one can simply use:

$$q(t)_{\text{corrected}} = 1.576 \left(\frac{q_{s_W}}{q_{s_{PTV}}} \right) q(t). \tag{4.31}$$

This simple methodology allows the correction of mean value, but do not assure proper fluctuation of solid discharge.

Chapter 5

Measurements of unsteady sediment transport

5.1 Flow hydraulics of steady conditions

Experimental runs were set by the flow discharge Q and the slope θ (see table 5.1). For each run $(Q;\theta)$ two sets of data were collected from flow properties: one through contact needle method and another through PIV measurements. Results shown on table 5.1 point out discrepancy between friction velocity calculated by each method. For each run, sediment transport was measured.

5.1.1 Base flow

Each set of measurements was individually studied to evaluate its accuracy and relevancy to our goals. To find the set of data that would better represent flow dynamics, an experimental inspection of critical Shields number Sh_c was performed. Firstly, flow discharge and channel slope were fixed with low Shields number to assure that no sediment transport was observed; slope was then gradually increased until sufficient movement of grains was detected in the counting chamber. These investigation proved that $u_{*\mathrm{CN}}$ was in agreement with u_{*c} calculated through Paphitis (2001) semi-empirical relation. So, despite greater uncertainties, measurement of mean flow properties based on contact needle method better represent the flow global dynamics, so that:

$$h_0 = h_{0\mathrm{CN}}; \tag{5.1}$$

$$u_0 = u_{0\mathrm{CN}}. \tag{5.2}$$

Table 5.1: Data compilation of PIV measurements for experimental tests with fixed bed.

Run	q ($\mathrm{lm^{-1}s^{-1}}$)	θ (rad)	Contact Needle			PIV System			Re	Fr	Sh
			$u_{0\mathrm{CN}}$ ($\mathrm{ms^{-1}}$)	$h_{0\mathrm{CN}}$ (mm)	$u_{*\mathrm{CN}}$ ($\mathrm{ms^{-1}}$)	$u_{0\mathrm{PIV}}$ ($\mathrm{ms^{-1}}$)	$h_{0\mathrm{PIV}}$ (mm)	$u_{*\mathrm{PIV}}$ ($\mathrm{ms^{-1}}$)			
gb1	1.05	0.0025	0.19	5.7	0.012	0.20	5.1	0.018	3940	0.79	0.050
gb2	1.04	0.0126	0.28	3.8	0.022	0.31	3.2	0.024	3870	1.44	0.165
gb3	1.02	0.0226	0.36	2.8	0.025	0.39	2.5	0.028	3670	2.15	0.224
gb4	0.98	0.0326	0.33	3.0	0.031	0.40	2.4	0.034	3600	1.90	0.342
gb5	1.54	0.0025	0.23	6.8	0.013	0.23	6.5	0.018	5625	0.87	0.060
gb6	1.54	0.0126	0.33	4.7	0.024	0.36	4.2	0.026	5640	1.54	0.205
gb7	1.52	0.0226	0.38	4.0	0.030	0.42	3.5	0.030	5530	1.93	0.316
gb8	1.53	0.0326	0.41	3.8	0.035	0.47	3.0	0.033	5670	2.13	0.428

These values are used to obtain dimensionless flow numbers (Fr, Sh and $\mathrm{Re} = 4u_0R_h/\nu$, where $R_h = h_0l_0/(l_0 + 2h_0)$ is the hydraulic radius).

However, since the methodology requires a time-dependent friction velocity $u_*(t)$, data obtained from PIV were still needed. A linear correlation was established between both methods of friction velocity measurement (local and global) (Figure 5.1), which allowed to correct $u*$PIV and to use it to estimate fluctuations of u_* as shows.

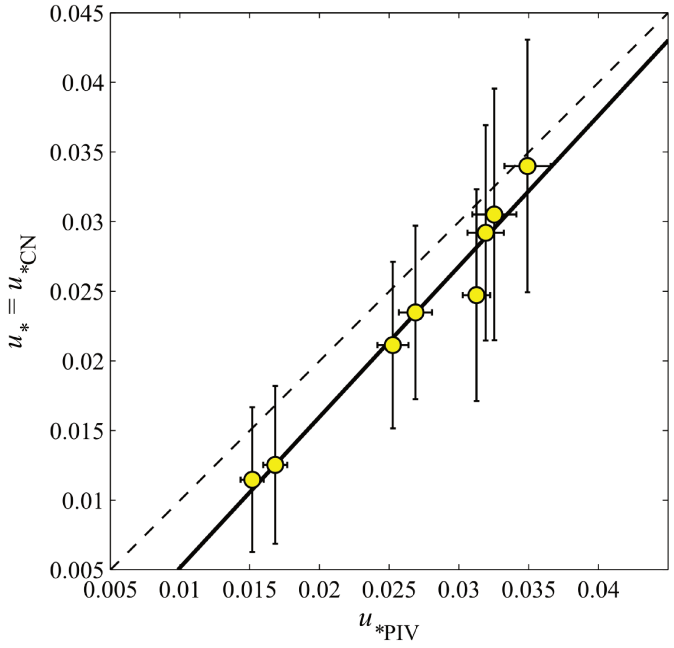

Figure 5.1: Correlation between friction velocity computed through both methods $u_{*\mathrm{CN}}$ and $u_{*\mathrm{PIV}}$. Solid line represent linear relation between both methods for friction velocity calculation. Dashed line represents equality $u_{*\mathrm{PIV}} = u_{*\mathrm{CN}}$.

The linear correlation is represented by the function

$$u_* = u_{*\mathrm{CN}} = 1.08u_{*\mathrm{PIV}} - 0.006, \tag{5.3}$$

with a correlation coefficient $R^2 = 0.96$[1].

[1] R^2 is the coefficient of determination that represents the goodness of the fit. The closer to 1 indicates that the better the function fits the data.

5.1.2 Turbulent properties

PIV Measurements pointed out that mean vertical velocity field can be neglected since $|\langle\bar{v}\rangle(y)| \sim 0.001$ m/s $< e_{\mathrm{PIV}}$ (see subsection 4.1.2), as shows Figure 5.2. So, only longitudinal component $\bar{u}(x, y)$ was considered in this study. However, inspection of fluctuating field consider both components defined by Reynolds separation (Equations 4.5 and 4.6). Profiles for $\langle\bar{u}\rangle(y)$ and $\langle u_{\mathrm{RMS}}\rangle(y)$ are plotted on Figure 5.3 and show expected behavior for turbulent flow profiles. For all tests, we remark that maximum value of $\langle u_{\mathrm{RMS}}\rangle(y)$ is achieved close to bed below 1 mm in accordance with the turbulent production by friction.

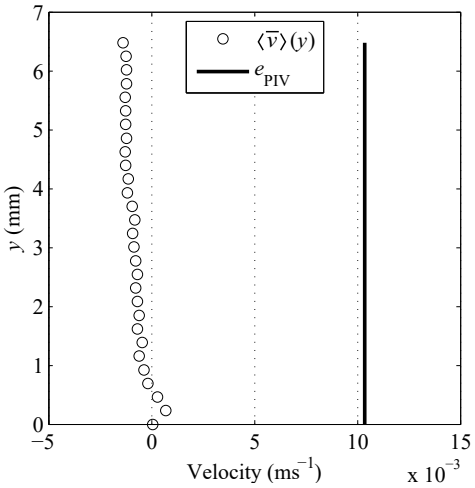

Figure 5.2: Averaged vertical velocity profile $\langle\bar{v}\rangle(y)$ compared to PIV system precision e_{PIV} for experimental run gb5.

Through inner coordinates transformation, it is possible to obtain refined friction velocity and refined vertical position to fit the experimental velocity profile with the universal profile (Schlichting, 1979) (Equation 2.13) as shows Figure 5.4. However, inside the viscous sublayer, precise results from our experiments could not be achieved for distances smaller than sediment particle diameter.

Since experimental runs have moderate Reynolds number ($2000 < \mathrm{Re} < 6000$), the profiles could be affected by modifications on channel relative roughness (ratio between sediments fixed to the bed and mean flow height) and presence of wakes (Bergstrom et al., 2001; Bigillon et al., 2006; Agelinchaab and Tachie, 2008). Turbulent intensities were verified based on An-

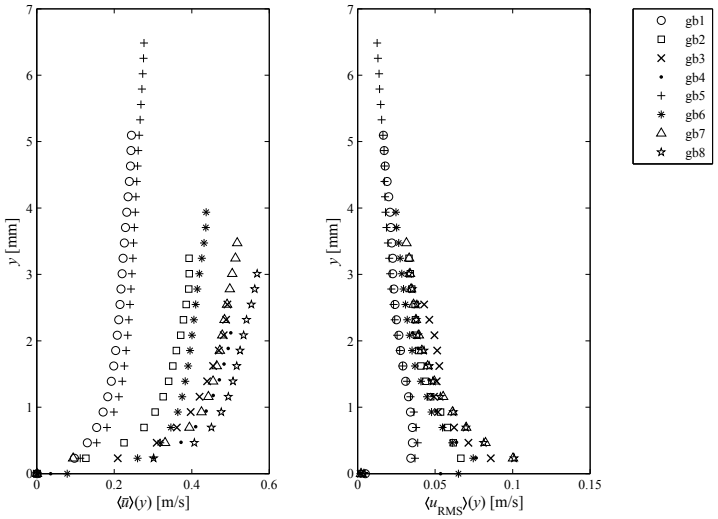

Figure 5.3: Results for average profiles of mean flow velocity $\langle \bar{u} \rangle(y)$ and standard deviation $\langle u_{\mathrm{RMS}} \rangle(y)$ for runs gb1 to gb8. See section 5.1.

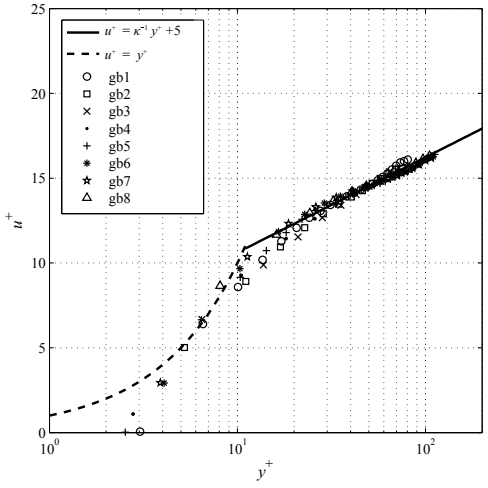

Figure 5.4: Turbulent characteristics of average profile of mean flow velocity. Lines indicate theoretical values: solid line is $u^+ = \kappa^{-1} \log y^+ + 5$ for log region; dashed line is $u^+ = y^+$ for viscous layer.

tonia and Krogstad (2001) work by the following empirical laws:

$$u^+_{\mathrm{RMS}} = A \exp\left(-\frac{y^+}{\mathrm{Re}_*}\right)\left[1 - \exp\left(-\frac{y^+}{B}\right)\right] + C y^+ \exp\left(-\frac{y^+}{B}\right); \qquad (5.4)$$

$$v^+_{\mathrm{RMS}} = 1.14 \exp\left(\frac{-0.76y}{h_0}\right) \tag{5.5}$$

where $A = 2$, $B = 8$, and $C = 0.34$. $\mathrm{Re}_* = u_{*\mathrm{PIV}} h_0/\nu$ is the Reynolds number using friction velocity as reference.

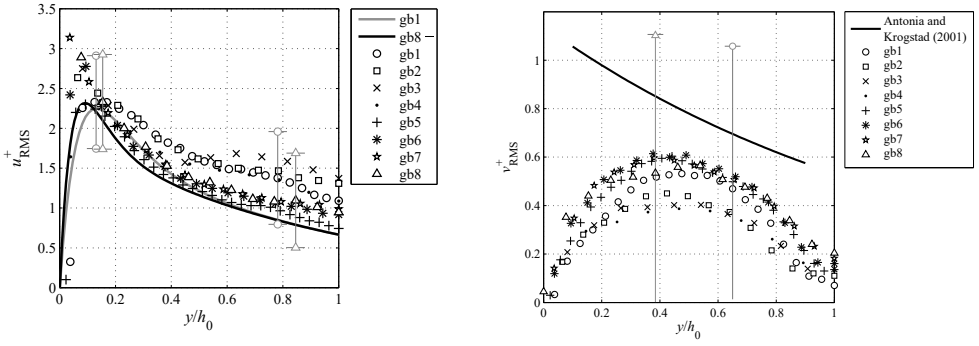

(a) (b)

Figure 5.5: Turbulent intensities for runs gb1 to gb8. Lines indicate computed values following empirical results from Antonia and Krogstad (2001). 5.5(a): longitudinal turbulent intensities u^+_{RMS}; dark line represent run gb1, and gray line, run gb8, following Equation 5.4. 5.5(b): vertical turbulent intensities v^+_{RMS}; dark line represent computed values from Equation 5.5.

As can be seen on Figure 5.5, the profiles for standard deviation in both direction followed the relations given by the referenced work from (Antonia and Krogstad, 2001) with a noticeable discrepancy. For the longitudinal fluctuations (5.5(a)), the shape identified obey to the empirical law used, although the experimental results show greater intensities than those expected. Conversely, the opposite behavior is noticed for the vertical fluctuations (5.5(b)): experimental values are lower than the empirical law here used as reference. Such results allowed us to speculate that even though full agreement was not achieved, the precision on the obtained velocity fields is sufficient to measure the fluctuations of the velocity due to the turbulent vortices, as shows Figure 5.6. It is very likely that the lack of accuracy on vertical velocities is due to the aspect ratio of the ROI.

5.1.3 Friction velocity

Based on the methodology explained on section 4.1.2, the position y_0 was chosen slightly above where the maximum value for $\langle u_{\mathrm{RMS}} \rangle$ is found, far

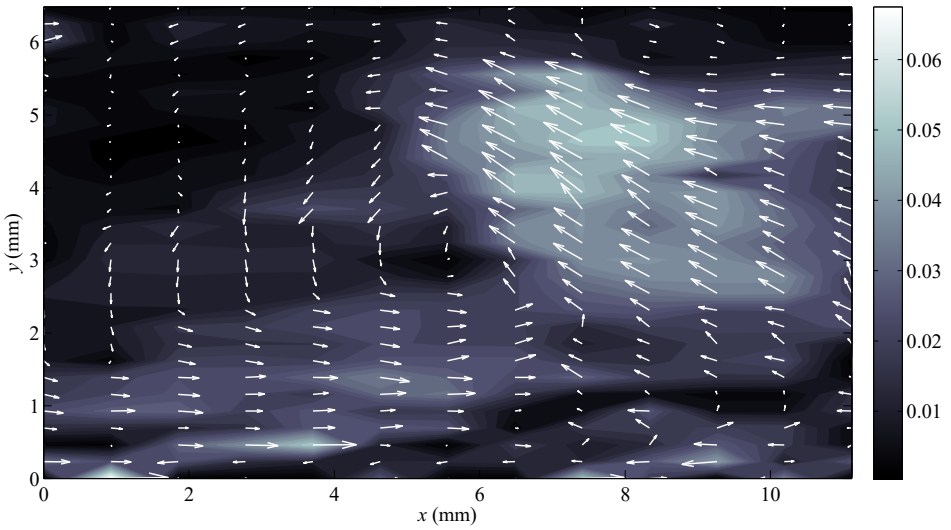

Figure 5.6: Instantaneous fluctuation field (u', v') for experimental run gb5. Shades indicates absolute value for velocity $(\sqrt{u'^2 + v'^2})$;

from the viscous sublayer. From those values, a linear fit is applied between $\langle\bar{u}\rangle(y_0)$ and $u_{*\mathrm{PIV}}$ to obtain the function F between both variables from base flow configuration, as shows 5.7(b). The following linear relation (Equation 5.6):

$$u_{*\mathrm{PIV}} = F\{\langle\bar{u}\rangle(y_0)\} = a\langle\bar{u}\rangle(y_0) + b, \tag{5.6}$$

where $a = 0.0703$ and $b = 0.0048$, shows good representativeness, with a correlation coefficient $R^2 = 0.99$.

To estimate instantaneous friction velocity, we postulated the hypothesis that the function F can be applied in any given instant of time. Then, a time-dependent series for frictional velocity is obtained $u_*(t)$ based on $\langle u\rangle(y_0, t)$:

$$u_*(t) = F\{u(x, y_0, t)\} = a\langle u\rangle(y_0, t) + b. \tag{5.7}$$

Constants a and b follow the lookup Table 5.2.

In order to check the validity of the hypothesis, the mean value for frictional velocity calculated through the function F is derived:

$$u_{*F} = \frac{1}{N_x}\frac{1}{N_t}\sum_x\sum_t u_*(x, t), \tag{5.8}$$

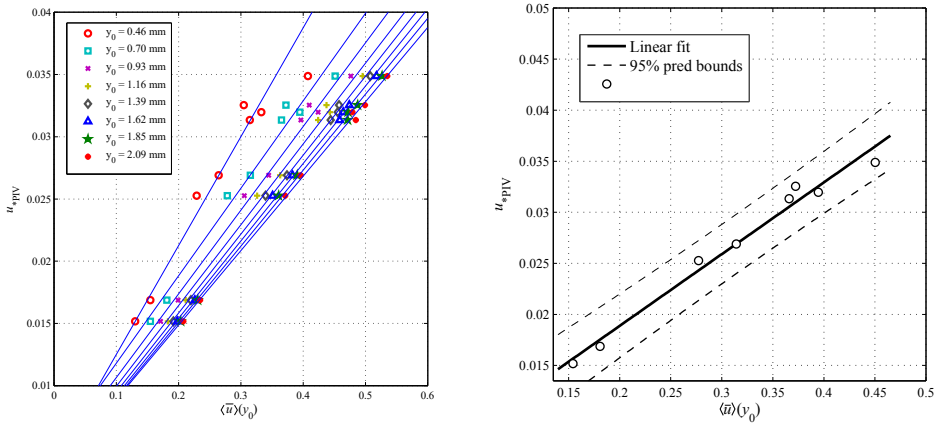

(a) (b)

Figure 5.7: Correlation between $\langle u \rangle(y_0)$ and $u_{*\mathrm{PIV}}$. 5.7(a): Different possible correlation between $u_{*\mathrm{PIV}}$ and $\langle \bar{u} \rangle(y_0)$.5.7(b): Highlight for $y0 = 0.70$ mm in Dark line represents first-order polynomial Equation 5.6. Dashed lines are 95% confidence boundaries.

Table 5.2: Lookup table for constants of function F used to obtain u_{*F}.

y_0 (mm)	y_0/D	a	b
0.46	2.3	0.0873	0.0038
0.70	3.5	0.0702	0.0048
0.93	4.6	0.0672	0.0040
1.16	5.8	0.0649	0.0035
1.39	7.0	0.0634	0.0032
1.62	8.1	0.0621	0.0030
1.85	9.3	0.0609	0.0029
2.09	10.4	0.0596	0.0030

and should be equal to $u_{*\mathrm{PIV}}$. When comparing both results, the hypothesis is consistent with measurements, since $u_{*F} \sim u_{*\mathrm{PIV}}$ with correlation coefficient is practically 1.

So, the function F could be considered as the linear relation between an instantaneous measured velocity at a given vertical coordinate y_0. Then frictional velocity imposed at the bottom could than be calculated as function of time $u_*(t)$. The Figure 5.8 shows an example of the signal obtained for $u_*(t)$ using such relation.

Physically speaking, the assumption made before seemed correct. When turbulent coherent structures passes and velocity varies, forces felt by sedi-

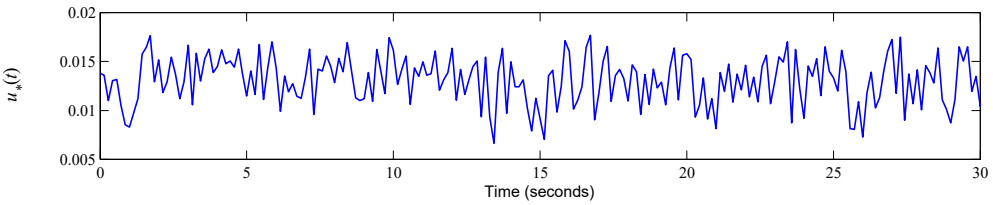

Figure 5.8: Time dependent signal of friction velocity $u_*(t)$ for PIV measurement gb5, using $y_0 = 0.46$.

ments should also vary following the stress applied by those vortices. Obviously this simple linear relation would not represent some of the complexity taking place in the boundary layer, specially for flows with low kinetic energy, where this relation should not stand (since function F isn't zero crossing.).

Having a friction velocity that depended on time, we then explored the power spectral density (PSD) (Oppenheim and Schafer, 2009) of the signal $u_*(t)$ to identify its frequency content[2]. The PSD is a mathematical tool that helps to identify the distribution of energy in the time-scales present in a discrete signal. For turbulent flows, this energy distribution follows a cascade of energy from the larger scale vortices (low frequencies) to small vortices (high frequencies), until reach the molecular scale, where dissipation by viscosity occurs. Applying a dimensional analysis (Chassaing, 2000), this decay of energy with the frequencies would follow a power-law function to the exponent $-5/3$ with the frequencies (wavenumber) of vortices.

From our equipment, the closest position to the wall where we could obtain velocity information without compromising the quality of measurements corresponded to $y_0 = 0.46$ mm. Figure 5.9 shows the PSD for $u_*(t)$ using two different values for y_0: one close to the bottom and another far from it. The energy decay explained before ($-5/3$) is obtained for isotropic turbulence, when flow is fully turbulent and developed. It is known that close to the walls such decay might change to -1 (Radice et al., 2009).

[2]The PSD $P_x(f)$ of a discrete signal $x(i)$ with N_x point is calculated as

$$P_x(f) = \frac{1}{f_s N_x} \left| \sum_{i=1}^{N_x} x(i) e^{-2\pi j f i / N_x} \right|^2 .$$

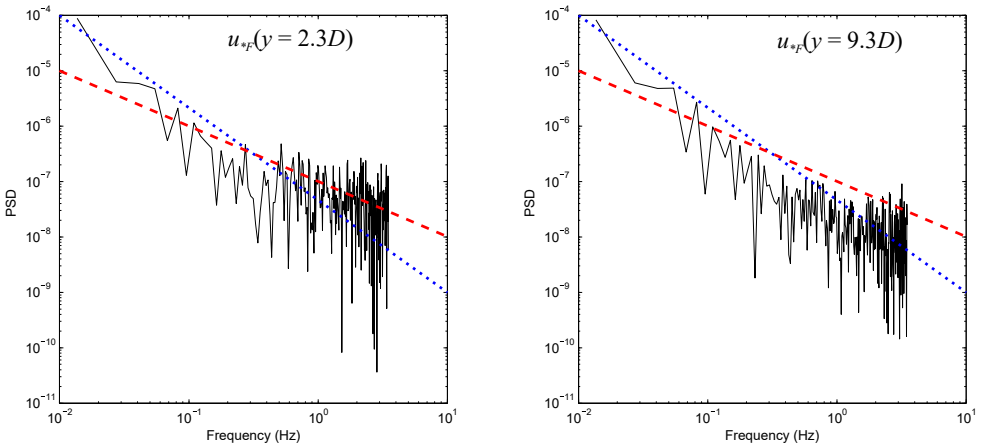

Figure 5.9: Power spectral density of $u{*}F$ for PIV experimental experimental run gb5 for two different flow heights y_0: one close to close $y_0 = 2.25D$ (image to the left); and another far from the bed $y_0 = 9D$ (image to the right). Red line indicates -1 slope; blue line $-5/3$ slope. Re $= 5625$; Fr $= 0.87$; Sh $= 0.060$.

Figure 5.9 shows that in both cases, the most part of the flow energy is transported by large scale vortices, with low frequencies. The energy decay represented by the blue dotted line shows the $-5/3$ decay, thus roughly verifying those scales flow correspond to fully turbulent structures. Due to the equipment precision, frequencies higher than 2 Hz might be considered as noise as a constant level of energy is achieved. However we can observe a slightly different behavior between both PSDs. Around 1 Hz, for $y_0 = 0.46$ mm $(= 2.25D)$, we see that the decay smooths and tends to the -1 decay while for $y_0 = 1.85$ mm $(= 9.3D)$ the decay keeps the $-5/3$ decay until reach noise level. Then, it might be possible to assume that as closer we get to the wall, the energy decay decreases, increasing the energy for larger eddies with low frequency. This observation is important as in the subsection 5.2.2 we explore close to wall flow fluctuations to understand solid discharge fluctuations.

Table 5.3: Data summary for all experimental tests with fixed glass beads bed in steady flow conditions.

Run	Sh	Fr	Ro	Transport Measures ($gm^{-1}s^{-1}$)					
				$\bar{q}_{WP}$ [3]	$\bar{q}_{sW}$	$\bar{q}_{sPTV}^{III}$	$q_{sPTV_{RMS}}^{'III}$	$\bar{q}_{sPTV}^{IV}$	$q_{sPTV_{RMS}}^{'IV}$
gb1-2	0.068	1.16	3.12	0.040	0.065	0.027±4%	0.033	—	—
gb1-3	0.075	1.20	2.99	0.110	0.179	0.372±8%	0.188	—	—
gb1-4	0.079	1.10	2.90	0.188	0.204	0.349±8%	0.232	—	—
gb2-1	0.158	1.55	2.05	2.979	1.187	1.722±6%	0.689	4.869±6%	0.697
gb2-2	0.159	1.54	2.05	3.016	1.896	1.887±6%	0.500	3.354±6%	1.653
gb3-1	0.237	2.02	1.68	7.808	2.537	—	—	8.837±6%	2.830
gb4-1	0.285	2.66	1.53	11.495	6.548	—	—	13.398±6%	4.025

5.2 Turbulence effects on sediment transport

In this chapter we focus on the understanding of general features of the data acquired and correlate them to flow properties. This should give enough information to be able to differentiate the results from those obtained in pulsating flows. The reference case is then the sediment transport by a turbulent runoff flow without superimposed waves.

5.2.1 Mean solid discharge

The first aspect that we explored in this context is how well the solid discharge is represented by the classical empirical formulas that can be found in the literature. First of all, after defining different zones from each experimental run (subsection 4.2.3), some remarks must follow:

- for low and intermediate Shields numbers, up to two mean values of transport $\bar{q}_s$ can be calculated, one for each zone q_s^{III} and q_s^{IV};
- for high Shields numbers, only one zone is identified in the signal partitioning, and then only q_s^{IV} is kept;
- for high Shields number, the solid discharge measured is corrected as explained in subsection 4.2.4, using Equation 4.31.

Seven experimental runs were used and summarized in subsection 5.2.1.

The results from subsection 5.2.1 show that fluctuation intensity of solid transport are greater than the measurement system precision, thus qualifying the measurement of $q'_{sPTV_{RMS}}$. The Figure 5.10 shows the results from subsection 5.2.1 in logarithmic and linear axis. It is possible to identify the uncertainties from the estimation of $\mathrm{Sh} - \mathrm{Sh}_c$ are more relevant than those

for $\bar{q}_{s\mathrm{PTV}}$. The fit represented in the Figure 5.10 by the purple dotted line have the following equation:

$$q_* = 7.93(\mathrm{Sh} - \mathrm{Sh}_c)^{1.8}, \tag{5.9}$$

and shows good agreement with Wong and Parker (2006) empirical relation (represented by the blue line). Nevertheless, uncertainties of Sh_c fits the results in between the empirical law given by Wong and Parker (2006) and the one given by Meyer-Peter and Müller (1948).

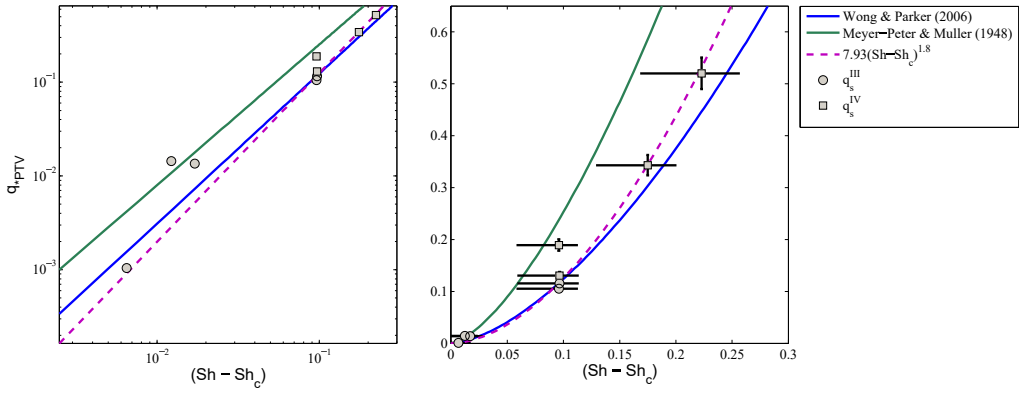

Figure 5.10: Empirical relation between Shields number and dimensionless solid discharge. Gray circles represent solid discharge q_s^{III} and gray squares q_s^{IV}. Dark solid lines represent uncertainties of measurement. Horizontal uses upper and lower limit curves from Paphitis (2001) to estimate the uncertainties on $\mathrm{Sh} - \mathrm{Sh}_c$. Purple dashed line represent fit of values from the present work.

5.2.2 Fluctuations intensities in solid discharge

Following the idea that near bed fluctuations directly affect sediment entrainment, we investigated how fluctuation intensity of friction velocity correlated to the fluctuation intensity of solid discharge. Following the empirical law F (Equation 5.6), we obtained the friction velocity fluctuation intensity $u'_{*\mathrm{RMS}}$. To assure minimum quality of measures, we inspect u_* at the position $y_0 = 0.70$ mm.

A simple reasoning can be developed based on classical empirical formulas to corroborate such observation. Considering the following classical law of transport employed to mean flow and mean transport:

$$q_* = A(\mathrm{Sh} - \mathrm{Sh}_c)^B = A'(u_*^2 - u_{*c}^2)^B; \tag{5.10}$$

then, the expression can be differentiated:

$$\frac{\partial q_*}{\partial u_*} = 2A'Bu_*\frac{(u_*^2 - u_{*c}^2)^B}{u_*^2 - u_{*c}^2}, \tag{5.11}$$

and then rewritten as

$$\frac{dq_*}{q_*} = \frac{2Bu_*}{u_*^2 - u_{*c}^2}du_*, \tag{5.12}$$

$$\frac{dq_*}{q_*} = 2B\frac{u_*^2}{u_*^2 - u_{*c}^2}\frac{du_*}{u_*} = 2B\frac{\mathrm{Sh}}{\mathrm{Sh} - \mathrm{Sh}_c}\frac{du_*}{u_*}. \tag{5.13}$$

In this expression, the term dq_*/q_* indicates the fluctuation intensity of transport and du_*/u_* the turbulence intensity or the fluctuation of friction, assuming that $du_* \propto u'_{\mathrm{RMS}}$ as $u_* \propto u_0$. So:

$$\frac{dq_*}{q_*} \sim \frac{q'_{*\mathrm{RMS}}}{\bar{q}_*}; \tag{5.14a}$$

$$\frac{du_*}{u_*} \sim \frac{u'_{*\mathrm{RMS}}}{u_*}. \tag{5.14b}$$

Consequently,

$$\frac{q'_{*\mathrm{RMS}}}{\bar{q}_*} = 2B\frac{\mathrm{Sh}}{\mathrm{Sh} - \mathrm{Sh}_c}\frac{u'_{*\mathrm{RMS}}}{u_*}. \tag{5.15}$$

This simple expression indicates that close to the imminence of transport ($\mathrm{Sh} \approx \mathrm{Sh}_c$) fluctuations of transport goes to infinity. On the other hand for sufficient high Sh the fluctuations of transport will be proportional to the turbulent intensity of the velocity field. For well-behaved turbulent flows where the fluctuation intensity follows a constant proportion of mean flow properties, $q'_{*\mathrm{RMS}}/\bar{q}_*$ should be a constant:

$$\frac{q'_{*\mathrm{RMS}}}{\bar{q}_*} = 2B\frac{u'_{*\mathrm{RMS}}}{u_*}. \tag{5.16}$$

In our experiments, we measured $14\% < u'_{*\mathrm{RMS}}/u_0 < 22\%$, possibly over estimated by measurement uncertainty as indicated by 5.5(a). So,

$$0.43 < \frac{q'_{*\mathrm{RMS}}}{\bar{q}_*} < 0.65, \tag{5.17}$$

assuming $B = 3/2$.

Figure 5.11 shows the results for $q'_{*\mathrm{RMS}}$ against the Shields number. The shaded zone indicates the region delimited by Equation 5.17, considering high Shields number. The blue solid line represents Equation 5.15 for

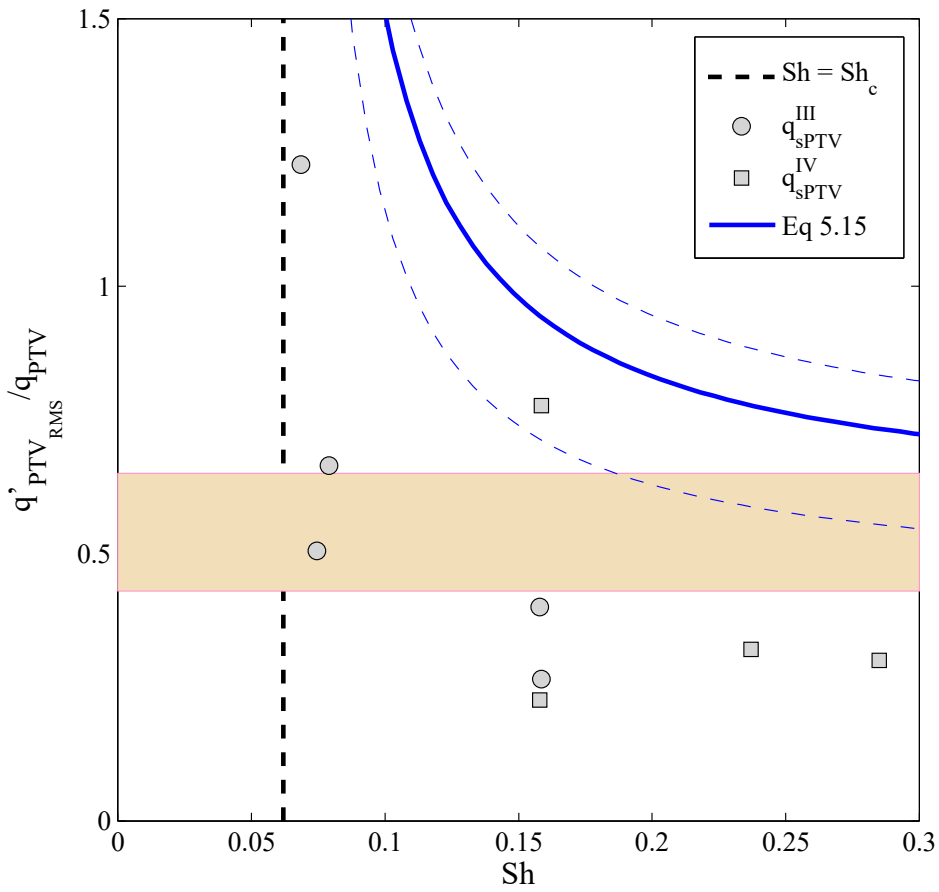

Figure 5.11: Fluctuations intensity of solid transport against Sh. The shaded region indicates the region for high Shields number as indicated by Equation 5.17. The blue solid line represents Equation 5.15 for $u'_{*\mathrm{RMS}}/u_* = 19\%$. Dashed lines uses maximum and minimum for $u'_{*\mathrm{RMS}}/u_*$.

$u'_{*\mathrm{RMS}}/u_* = 19\%$.

The data show that solid discharge fluctuations are relatively greater for flow $\mathrm{Sh} \approx \mathrm{Sh}_c$ than $\mathrm{Sh} \gg \mathrm{Sh}_c$. This observation is in agreement with the Equation 5.15, represented by the blue solid line. Works from the literature for close to threshold bedload transport discuss about the intermittency of solid discharge in those conditions and high fluctuations of the transport (Einstein, 1950; Ancey et al., 2006; Singh et al., 2009; Ma et al., 2014).

For high Sh, Sh > 0.2, fluctuations of transport fall into the shaded zone illustrated in Figure 5.11. From the expression 5.15, we estimated that for Sh $\approx 4\mathrm{Sh}_c$, flow would provide enough shear stress to lead transport fluctuations into the shaded zone.

5.2.3 Spectral properties of time dependent solid discharge

As the intensity of fluctuations have already been discussed in the previous section, here the normalized power spectral density (PSD) of the solid discharge signal $q(t)$ is employed to explore the frequency content of the signal. This analysis should provide information comparable to those obtained for flow friction measurements.

Firstly we established a base test where we could explore the features that we should look for in the other cases. The test that is first explored is the experimental run gb1-4, for q_s^{III} as presents Figure 5.12.

On Figure 5.12, in gray the part of the PSD ($f > 10$ Hz), the level of energy is low, two order of magnitude smaller than the energy present in small frequencies. We than consider that this part of signal would not present any significant information for the work here performed. We perceived that for low frequencies, the decay of energy approximates the -1 slope (red line) and the high levels of energy were present. Around 1 Hz the behavior seems to change, adopting $-5/3$ decay (blue line). These could be an indication that for low Shields number the relevant energy present in solid discharge have the same expected dynamic for the friction velocity fluctuations (see subsection 5.1.3). Two other experimental runs for low Shields number were studied to verify that possibility. Their PSD are shown in Figure 5.13.

The same observations made for experiment gb1-4 were applicable to gb1-2 and gb1-3. For Sh slightly above Sh_c, particles are entrained in contact with the bed. So, near to bed flow turbulent structures would be responsible for particles entrainment. In this way, flow turbulent structures transfer their dynamics to particle, and both have the same energy decay -1. However, looking more closely to experiment gb1-2, 5.13(a) shows that the definition of the $-5/3$ slope is not clear. While low frequency fluctuations still seem to present -1, for frequencies between 0.2 and 3 Hz (yellow shaded region) the decay of energy does not fit any of the expected behaviors, almost presenting a constant level of energy distribution. For frequencies higher than 3 Hz, spectral density seems to adopted the $-5/3$

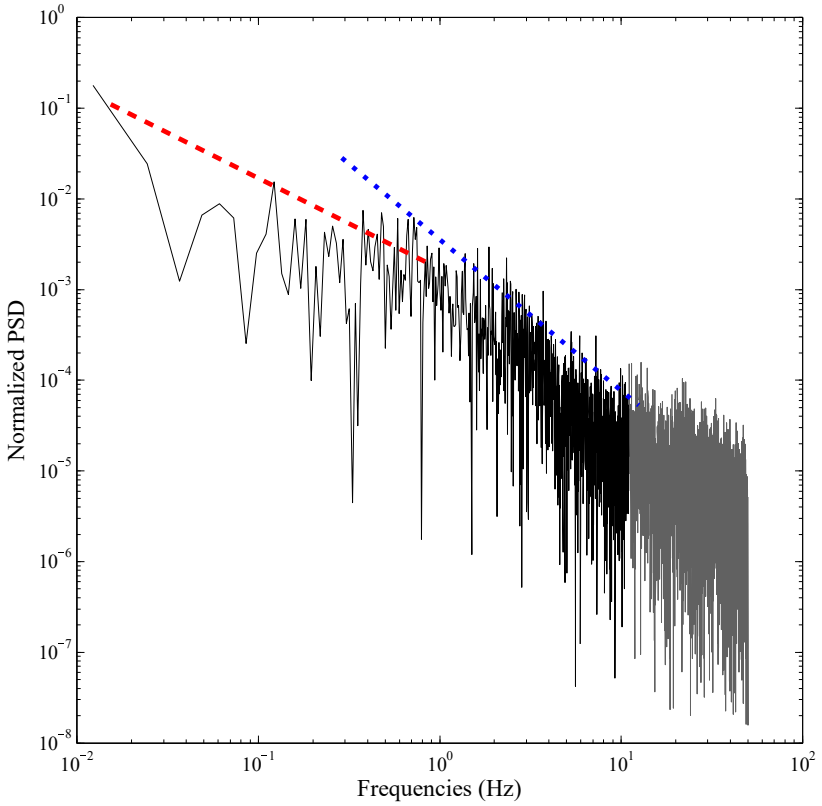

Figure 5.12: Normalized power spectral density for experimental run gb1-4 (q_s^{III}), with $\mathrm{Sh} = 0.079; \mathrm{Fr} = 1.10; \mathrm{Ro} = 2.90$. Dotted blue line represents $-5/3$ slope and red line -1 slope. Gray line indicates negligible information.

decay. For the constant energy level interval (0.2 and 3 Hz), this would correspond to a spectral gap, as mentioned by Singh et al. (2009), that could be used to separate different contributions of turbulence.

For a same experimental run with intermediate Shields number, whenever solid discharge can be sectioned (subsection 4.2.3), two different PSD can be analyzed. From the literature (Guignier, 2014), there are evidences that when bedforms are formed in the mobile bed, they change how the sediment is entrainment. On Figure 5.14 both PSD from q_s^{III} and q_s^{IV} are plotted. However, the signal q_s^{III} is considerably shorter than q_s^{IV}, which does not give the same quality of results for the PSD. Nevertheless, we observe

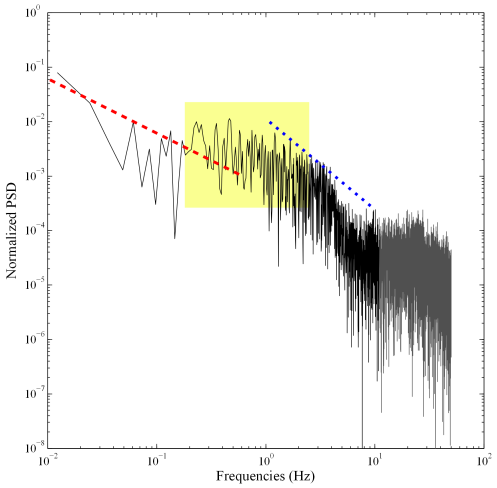

(a) : gb1-2

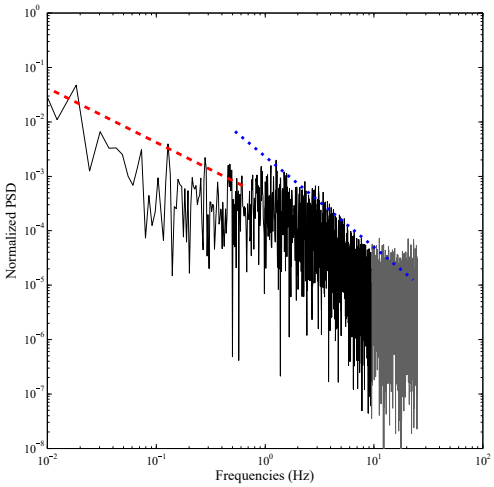

(b) : gb1-3

Figure 5.13: Normalized power spectral density for experimental runs 5.13(a) gb1-2 (q_s^{III}), with $\mathrm{Sh} = 0.068; \mathrm{Fr} = 1.16; \mathrm{Ro} = 3.12$; 5.13(a) gb1-2 ($q_s^{\mathrm{III}}$), with $\mathrm{Sh} = 0.075; \mathrm{Fr} = 1.20; \mathrm{Ro} = 2.99$. Dotted blue line represents $-5/3$ slope and red line -1 slope. Gray line indicates negligible information. Shaded yellow zone highlight possible spectral gap.

as well that the -1 slope is once again present when the solid transport has no influence of bedforms (q_s^{III}). When bedforms (dunes, in this case)

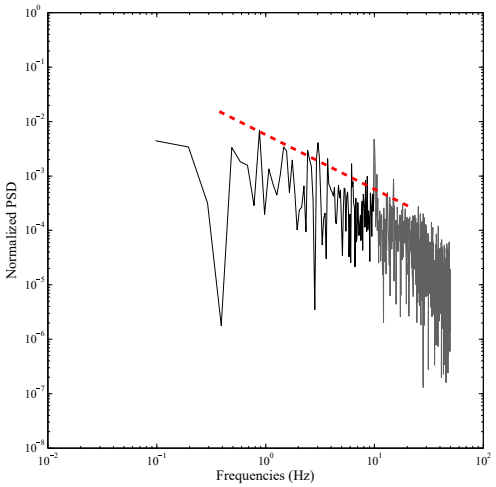

(a) : q_s^{III}

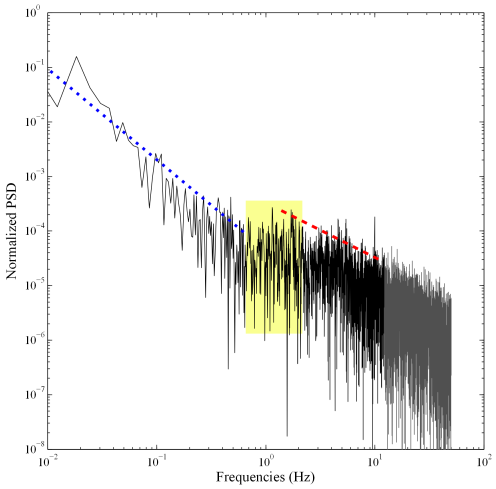

(b) : q_s^{IV}

Figure 5.14: Normalized power spectral density for experimental run gb2-2, with $\mathrm{Sh} = 0.159; \mathrm{Fr} = 1.54; \mathrm{Ro} = 2.05$. 5.14(a): no bedforms captured; 5.14(b); bedforms detected on the signal. Dotted blue line represents $-5/3$ slope and red line -1 slope. Gray line indicates negligible information. Shaded yellow zone highlight possible spectral gap.

reach the counting chamber, they change the shape of the PSD figuring now the $-5/3$ decay for low frequencies and -1 for frequencies higher than 2 Hz.

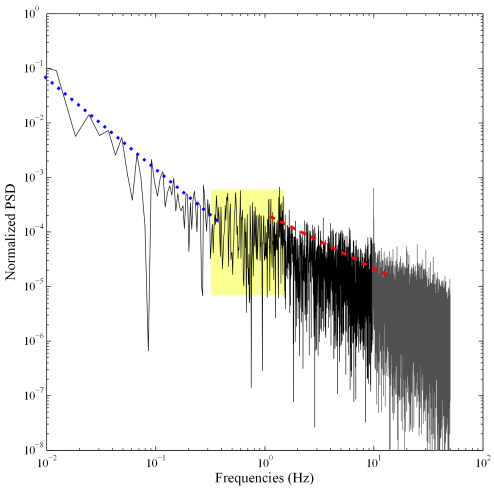

Figure 5.15: Normalized power spectral density for experimental run gb4-1, with $\mathrm{Sh} = 0.285; \mathrm{Fr} = 2.66; \mathrm{Ro} = 1.53$. Dotted blue line represents $-5/3$ slope and red line -1 slope.

Increasing even more the Shields number, now also reaching very high Froude numbers ($Fr > 2$), bedforms in our experiment could not be visualized. This could result of insufficient mobile bed length (bedforms could not develop); or plane-bed configuration was reached. Looking to the PSD of experimental run gb4-1, we observed that the same behavior from intermediate Shields number. Finally, the major conclusion is that the PSD of the transport signal exhibit a cascade of energy with a power law between -1 and $-5/3$ similar to the PSD of the friction velocity presented in subsection 5.1.3.

5.3 Pulsating flow

As mentioned in subsection 4.1.5, the frequencies used to disturb the runoff flow depended on the mean flow velocity, between 2 and 2.5 Hz. Frequencies were chosen so that at least two wavelengths ($\lambda \approx 15$ cm) fit inside the mobile bed length. The same results presented in the chapter before are presented for the pulsating flows, so a direct comparison can be made. The results from solid transport in disturbed flow are summarized in section 5.3.

Table 5.4: Data summary for all experimental tests with fixed glass beads bed in disturbed flow conditions.

Run	Sh	Fr	Ro	Transport Measures ($gm^{-1}s^{-1}$)					
				$\bar{q}_{WP}$ [4]	$\bar{q}_{sW}$	$\bar{q}_{sPTV}^{III}$	$q'^{III}_{sPTV_{RMS}}$	$\bar{q}_{sPTV}^{IV}$	$q'^{IV}_{sPTV_{RMS}}$
gbw1	0.050	0.79	3.64	—	0.111	0.253±7%	0.388	—	—
gbw2	0.158	1.51	2.05	2.979	0.754	—	—	1.568±6%	1.459
gbw4	0.294	2.47	1.50	12.289	7.615	8.662±6%	2.459	—	—
gbw5	0.063	0.79	3.24	0.003	0.046	0.056±7%	0.051	—	—
gbw6	0.198	1.60	1.83	5.229	1.919	—	—	4.304±6%	3.500
gbw8	0.399	2.34	1.29	22.257	14.172	—	—	16.345±6%	5.446

5.3.1 Mean solid discharge

When looking into the results from mean solid discharge obtained, a fit can be seen in results which follows the same exponent as the results shown by the steady flow, as shown by the red dashed line in Figure 5.16. When comparing the results found with those from undisturbed flow, a behavior can be noticed (Figure 5.16), showing that mean solid discharge for pulsating flows is smaller than those in steady flow and the relation between q_* and Sh is now

$$q_* = 4.57(\mathrm{Sh} - \mathrm{Sh}_c)^{1.8}, \tag{5.18}$$

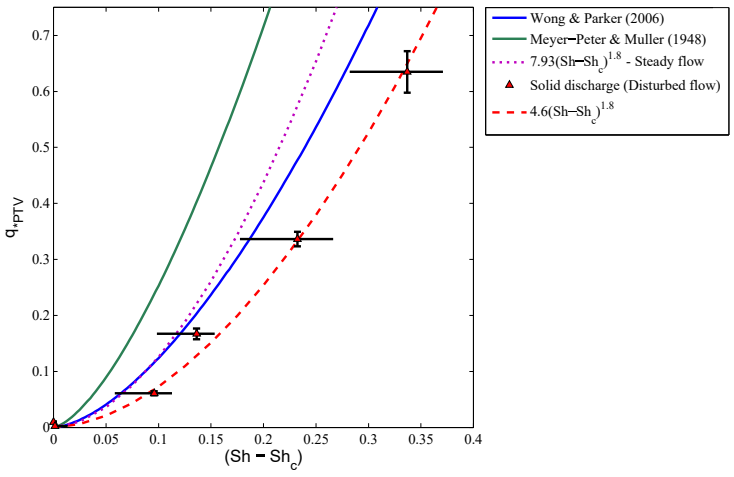

Figure 5.16: Results solid discharge for pulsating flows. Dotted lines indicate empirical relation found for solid discharge in steady flow conditions. Dashed line represent fit from disturbed flow conditions.

In order to understand this transport reduction, velocity fluctuations with or without free surface disturbances are presented on Figure 5.17. On the one hand, PIV results (Figure 5.17) show that fluctuation intensities increase close to the free surface for disturbed flow. On the other hand, close to the bottom, no considerable variations of fluctuation intensity was detected. Another way to verify this is to evaluate u_{*F}, which represents the mean friction velocity calculated based on $u_*(t)$, for disturbed flow. Figure 5.18 shows variations of u_{*F} for disturbed flow in the order of 2% away from the bed, and around 5% when close to the bed.

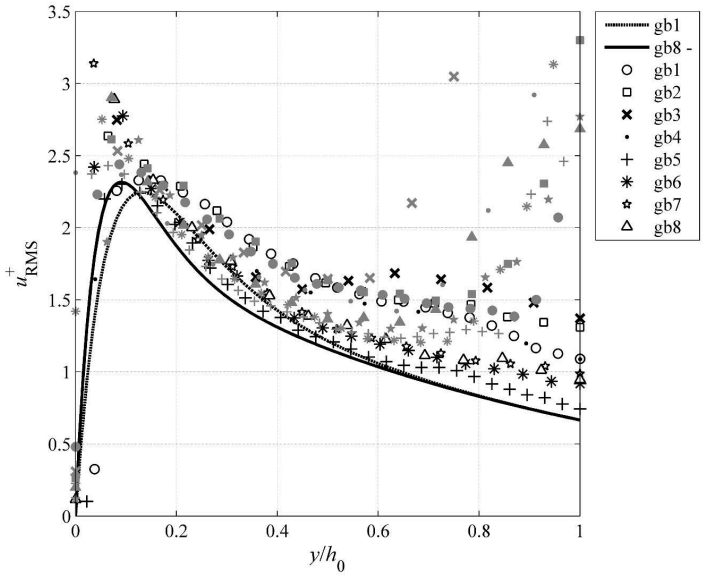

Figure 5.17: Fluctuation intensity of velocity field for steady and pulsating flow. Steady flow experiments are represented by black symbols and disturbed flow by gray ones.

A phenomenon that could explain the decrease in bottom shear stress is the shape of waves propagating on the free surface. Works from the literature (Ng and Mei, 1994; Toniati et al., 2015) present the variation of bottom shear stress for roll waves in laminar flows. Results presented in the figures 2.15 and 5.19 show waves height, mean flow velocity and bottom shear stress over the wavelength. The images are dimensionless and the value 1 in the vertical axis denotes base flow properties. We can then see that waves induce a small period of friction increase and a long period of reduced friction generating a global reduce of the average friction (< 1), a

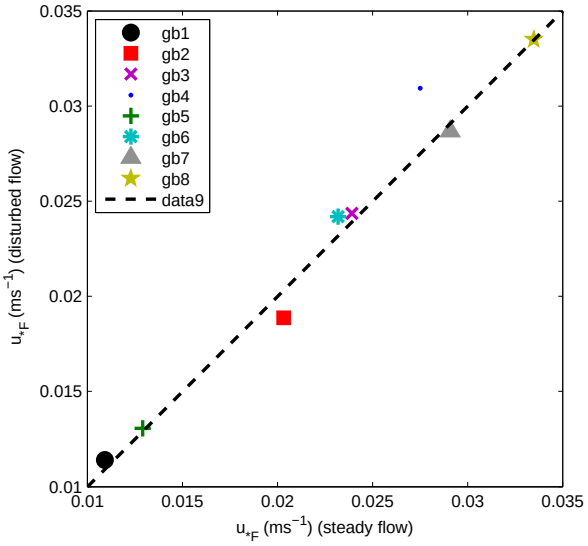

Figure 5.18: Ratio between u_{*F} calculated for disturbed and steady flow conditions for $y_0 = 0.70$ mm.

behavior that is observed for the simulations shown in figures 2.15 and 5.19. Considering a mean value of bottom shear stress in the period of wave, values are below the mean base flow shear stress. In the same way, this effect could also be present in turbulent flows, thus explaining the reduction of solid transport observed when flow is disturbed.

5.3.2 Fluctuations intensities in solid discharge

Following the observations from the fluctuation field Figure 5.17, we know that the disturbances applied to the flow are not capable to modify the fluctuation intensities close to the bed. So, the empirical relation F can be applied. Such hypothesis allow the same analysis from chapter before to be applied, which gives us then the results in Figure 5.20. For sake of comparison, results from steady conditions are also plotted.

In the experiments for disturbed flow, we measured $12\% < u'_{*\mathrm{RMS}}/u_0 < 22\%$ so,

$$0.36 < \frac{q'_{*\mathrm{RMS}}}{\bar{q}_*} < 0.65, \tag{5.19}$$

assuming $B = 3/2$. Figure 5.20 shows that $q'_{*\mathrm{RMS}}$ for disturbed flows pre-

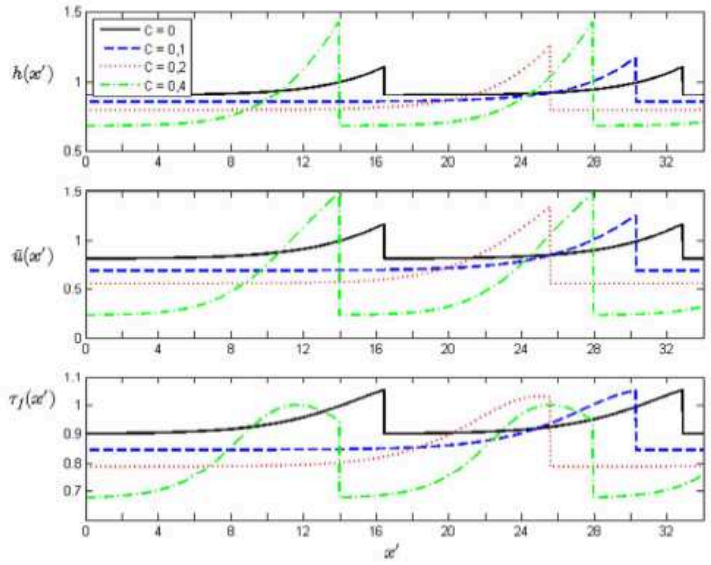

Figure 5.19: Results from the mathematical model for laminar roll waves (Maciel et al., 2013; Toniati et al., 2015) for different fluids.

sented the same behavior. The shaded zone indicates the region delimited by Equation 5.19, considering high Shields number. The red solid line represents Equation 5.15 for $u'_{*\mathrm{RMS}}/u_* = 17\%$. We can see again that the Equation 5.15 represents the behavior observed from solid discharge results but overestimates the fluctuations. This might be an effect of the signal constructed for $u_*(t)$ and the noise from the PIV measurements.

5.3.3 Spectral properties

The PSD from sediment transport signal with a disturbed flow (Figure 5.21) shows again the behavior noticed from steady flows: for low Shields (5.21(a)), energy decay follows the -1 slope for low frequencies; for higher Shields number, energy density follows $-5/3$ slope. In those PSD we detected a frequency range where energy decay is kept constant (yellow shaded zone). The disturbance frequency applied to flow (between 2 and 2.5 Hz) is not noticed in the solid discharge spectrum.

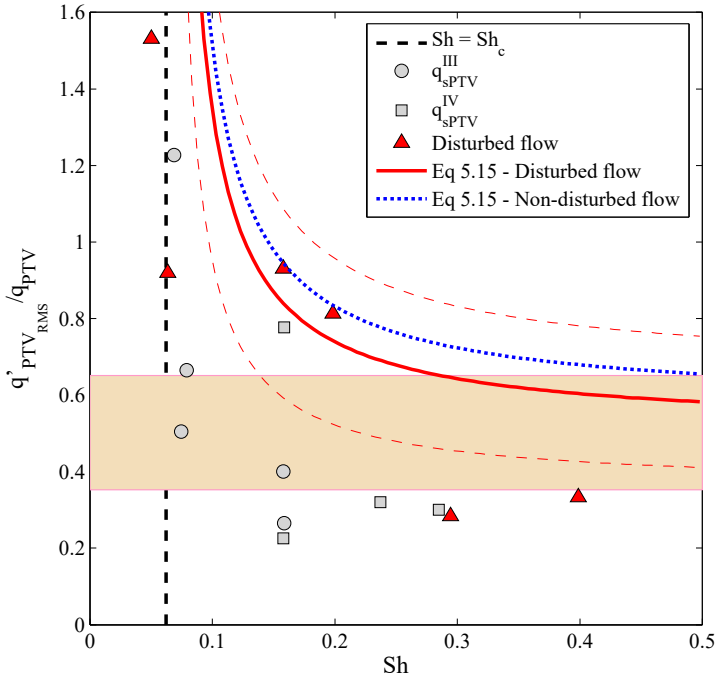

Figure 5.20: Fluctuations intensity of solid transport for steady and disturbed flow conditions against Sh. The shaded region indicates the region for high Shields number as indicated by Equation 5.17. The blue dotted line represents the undisturbed flow conditions. Red lines (solid and dashed) present Equation 5.15 for values for $u'_{*\mathrm{RMS}}/u_*$ in disturbed conditions.

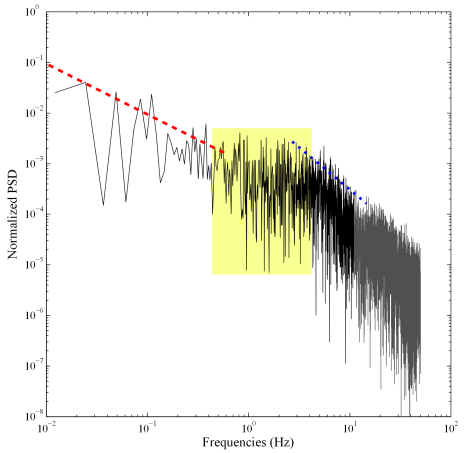

(a) : gbw5

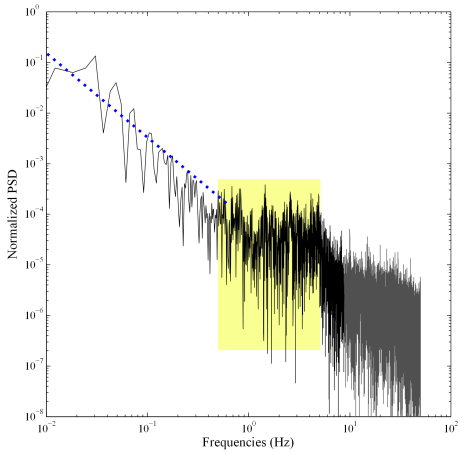

(b) : gbw2

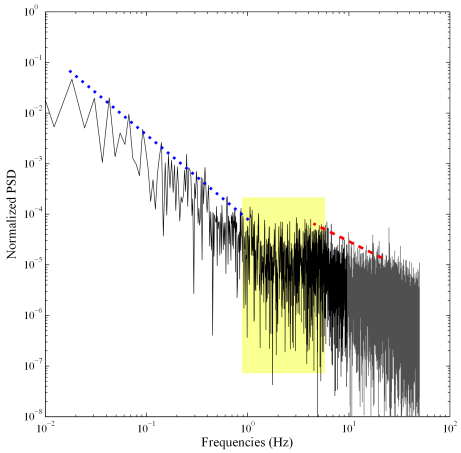

(c) : gbw4

Figure 5.21: Normalized power spectral density for experimental runs 5.21(a) gbw5 (q_s^{III}), with $\mathrm{Sh} = 0.063; \mathrm{Fr} = 0.79; \mathrm{Ro} = 3.24$; 5.21(b) gbw2 ($q_s^{\mathrm{IV}}$), with $\mathrm{Sh} = 0.198; \mathrm{Fr} = 1.60; \mathrm{Ro} = 1.83$; and 5.21(c) gbw4 ($q_s^{\mathrm{IV}}$), with $\mathrm{Sh} = 0.399; \mathrm{Fr} = 2.34; \mathrm{Ro} = 1.29$. Dotted blue line represents $-5/3$ slope and red line -1 slope.

Part II

Non-Newtonian fluid flows over natural environments

Chapter 6

Introduction

From a mechanical point of view, the representation of mass-movement can be done through many physical approaches (Iverson, 1997). Choosing a specific model over another relies on the representativeness of that model to the target phenomenon. Among mass-movements events, mudflows are natural events well represented by hydraulic approaches. From this last perspective, fluids in mudflows are usually modeled as an equivalent non-Newtonian fluid, mixtures of water with high concentration of sediment (Graf and Altinakar, 2000).

It is important to remark that the correct representation of fluids in this kind of phenomena requires attention. The variability found on solid-liquid fraction composing the mixture contribute to the complexity of the fluid which could also present cohesive or noncohesive behavior, depending on the material in suspension. Then, to exactly quantify shear ratio suffered from fluid due to stress applied is not usually possible. Mudflows are mixtures which sediment concentration is high and can be characterized mainly by the presence of a yield stress and viscous interactions. Moreover, when dispersive turbulent stress are remarkably noticed and grain to grain contact is important, those become the main mechanism of energy dispersion, thus characterizing mud floods and granular debris flow events (Coussot and Meunier, 1996). As have been shown on Figure 2.4, the classification of the event depends on the ratio between liquid and solid fraction in the mixture, and also on particles grain size distribution. Such classification is important to properly quantify the boundary dissipation and the friction factor, so flow properties can be determined.
The topography and natural landscape on mountain regions may have favorable conditions for roll waves generation. In the past 10 years, several mathematical models have been developed on mud and debris flows, adding

up complex features such as arbitrary topography, non-Newtonian fluid rheology and assuming unstable conditions of the free surface (van Asch et al., 2007; Balmforth and Mandre, 2004; Zanuttigh and Lamberti, 2007), to optimize the prediction of natural events such as those. the validation and application of such models to practical problems is an important task for scientific and engineering communities which is not easily performed, as illustrated in this thesis. Lack of reliable data of natural events and proper representation of physics involved are some of the factors responsible for such difficulty.

The Acquabona event from 1998 is one the events registered in the literature where the presence of surges in the mud-debris flow event can be observed. It was classified by Berti et al. as a debris flow event, although they have not quantified the dispersive turbulent term. The problem rests open for a different read of the event as a mudflow, accordingly to Coussot and Meunier (1996); Coussot (1992). As shown in Figure 6.1, mud and debris flow present the same behavior, shear-thinning yield stress fluids, which can be represented by Herschel-Bulkley rheological model, for example. Identify the most indicated rheological behavior based on the concentration sometimes is not sufficient. For complex rheological fluid behaviors, not only concentration plays an important role, as well as geometry of particles themselves (Mueller et al., 2009) and their chemical and organic nature.

The objective of the following chapters of this thesis was to evaluate how good an existing model is to predict a natural events, and then to study how adding another control parameter (porosity) would change the model representativeness. The event from August 17th, 1998, at Acquabona creek related by Berti et al. (1999, 2000) was chosen as the case study to analyze the validity of the model proposed by Maciel et al. (2013). The waves presented long period and fast propagation velocity and seemed constitute a wave train at some point, thus inducing us to think that roll waves could have been generated during the event. Then, a more complex analytical model was searched considering that the channel bottom was porous. We found a deterministic solution for the velocity profile of non-Newtonian fluids in an open-channel in presence of a porous bed.

To verify the theoretical solution, numerical simulations on FLUENT were performed. The characteristic present in flows over porous medium is the presence of a slip velocity at the interface between flow and bottom channel, thus reducing bottom shear stress. The problem is summarized in validating the boundary condition adopted for the deterministic solution.

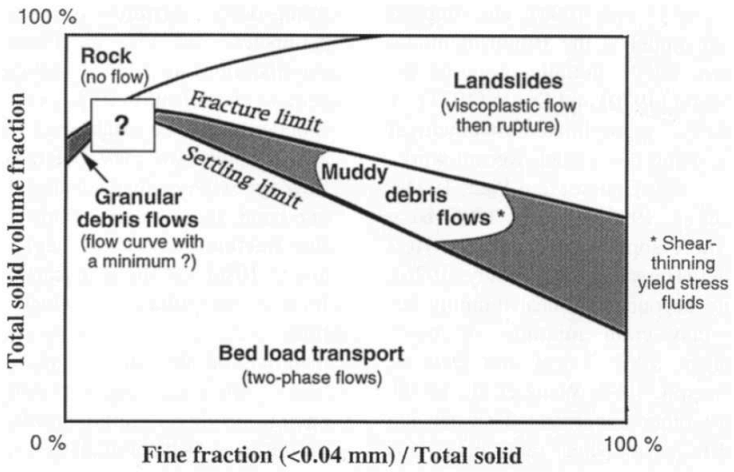

Figure 6.1: Conceptual rheological classification of mass movements as a function of fine content and solid fraction. The exact limits between the different parts of the diagram should be determined for each material and may slightly vary with flow characteristics. (From Coussot (1992).

A parametric study was performed on the mathematical solution to determine how non-Newtonian fluid properties interact with the porosity effect of the bed. It was observed that the influence of bed porosity was smaller the more non-Newtonian the fluid.

Chapter 7

Application of mathematical model to natural events: the Acquabona creek

7.1 Mathematical and numerical modeling of roll waves

The 2D mathematical model for roll waves (Maciel et al., 2013) employed in the present work gives, as result, the free surface profile over the longitudinal coordinate as well as wave properties. To obtain such results, a complete set of dimensionless input parameters must be determined, namely base flow properties and fluid rheology (see Figure 7.1). Usually when dealing with measurements obtained from natural events, the necessary parameters cannot be determined, thus requiring a pre-processing step to be performed before solving the roll wave model.

Figure 7.1 shows the two stages necessary to the successful utilization of the mathematical model. To the left, the preprocessing stage also called parameters gathering: an iterative method performed to solve the constitutive equations of the problem and to find the proper set of input parameters based on available data for a specific event. To the right, the roll waves simulation procedure, where the set of dimensionless parameter is input into the mathematical.

To obtain the roll waves equation, which is a first-order nonlinear differential equation, the conservation equations, mass and *momentum*, are manipulated (Equations 2.23a, 2.23b and 2.23c). Same conditions as mentioned on section 2.3 are considered.

The Herschel-Bulkley rheological model (Equation 2.21) is used in the

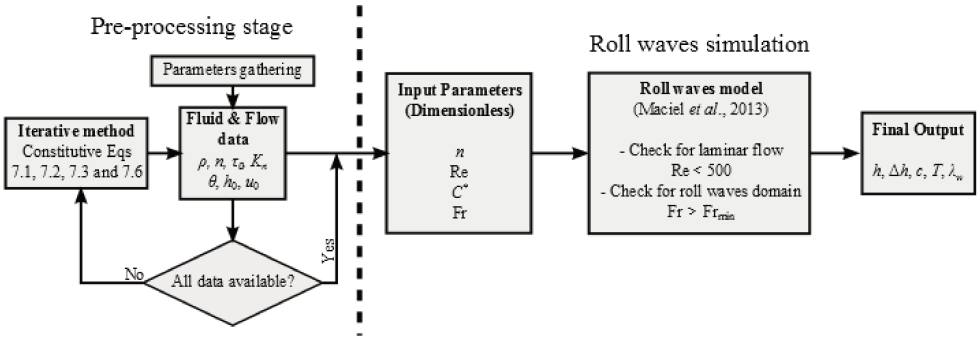

Figure 7.1: Diagram showing methodology employed for roll waves model application Maciel et al. (2013). To the left, parameters gathering finds through iterative solution of constitutive equations the proper set of input parameters whenever necessary. To the right, roll waves model verifies flow regime and stability condition and gives the solution of roll waves as well as wave properties.

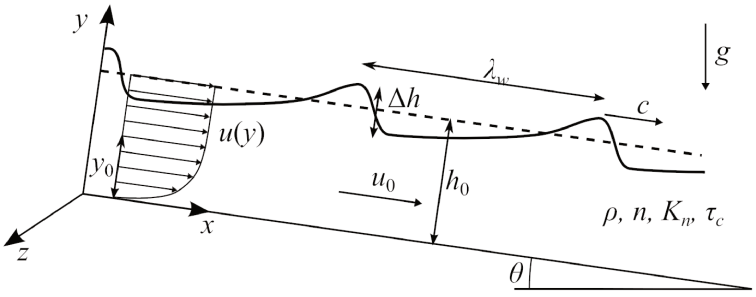

Figure 7.2: Schematics on roll waves properties for permanent flow. Dashed line represent based flow with properties h_0 and u_0, where u_∞ is flow freestream velocity. Solid line represent the same flow when roll waves are present and its main properties: wavelength λ_w, wave celerity c and amplitude Δh.

viscous part of the stress tensor to represent fluid properties. Flow is considered laminar (Re < 2000), in shallow water conditions, steady and uniform, at instance. The velocity profile $u(y)$ is obtained and written as function of mean flow velocity u_0 and rheological properties as shown in Equation 7.1:

$$u(y) = \begin{cases} \left(\frac{2n+1}{n+1+nC^*}\right) u_0 \left[1 - \left(1 - \frac{y}{h_0(1-C^*)}\right)^{\frac{n+1}{n}}\right] & \text{for } 0 < y < y_0 \\ \left(\frac{2n+1}{n+1+nC^*}\right) u_0 & \text{for } y_0 < y \leq h_0 \end{cases}, \quad (7.1)$$

where y_0 is the limit between sheared fluid layer and plug zone ($y_0 = h_0(1 - C^*)$). This profile (Figure 7.2) shows that for such a non-Newtonian fluid, there is a fluid layer that assumes constant maximum velocity (plug zone). Looking to the $y_0 < y < h_0$, we can identify a simple relation between free surface velocity $u_\infty = u(y = h_0)$ and mean velocity which can be useful given by Equation 7.2:

$$u_\infty = \left(\frac{2n+1}{n+1+nC^*}\right) u_0 \quad (7.2)$$

Finally, the velocity profile can also be represented by its vertical distribution through the momentum distribution coefficient α:

$$\alpha = \frac{1}{u_0^2 h_0} \int_0^{h_0} u(y)^2 \, \mathrm{d}y = \left(\frac{2n+1}{3n+2}\right) \left(\frac{n(4n+3)C^* + 2(n+1)^2}{(nC^* + n + 1)^2}\right). \quad (7.3)$$

This dimensionless parameter can assume values between 1 and 1.2. The closer this value is to one, the greater the plug zone; for Newtonian fluids, this parameter assumes the value 1.2, classic value in the literature for a parabolic velocity profile distribution.

The conservation equations are then vertically averaged by mean values for flow height (h_0) and velocity (u_0). Through this methodology, a dimensionless system is reached (see Maciel et al. (2013) for further details), a Saint-Venant alike system:

$$\frac{\partial h^*}{\partial t^*} + \frac{\partial h^* u^*}{\partial x^*} = 0; \quad (7.4a)$$

$$h\left(\frac{\partial u^*}{\partial t^*} + \alpha u^* \frac{\partial u^*}{\partial x^*}\right) + \frac{h^*}{\mathrm{Fr}^2}\frac{\partial h^*}{\partial x^*} + (1-\alpha)u^*\frac{\partial h^*}{\partial t^*} = \\ = h^* - C^* - (1 - C^*)\left[h^* u^* \frac{(1-C^*)(n+1+nC^*)}{(h^* - C^*)(nh^* + h^* + nC^*)}\right]^n, \quad (7.4b)$$

and the superscript * indicates dimensionless variables:

$$x^* = x/L_0; \quad y^* = y/h_0; t^* = tu_0/L_0; \quad u^* = u/u_0.$$

To obtain the roll waves equation, dimensionless conservation equations are manipulated using a mobile coordinate system ($\xi = x - ct$) following the waves at their speed c (Julien and Hartley, 1986) which assumes the form:

$$\frac{c}{u_0} = \alpha + \sqrt{\alpha^2 - \alpha + \frac{1}{\mathrm{Fr}^2}}. \tag{7.5}$$

The system is then manipulated, culminating in the final form of roll waves equation, a first-order differential equation on the flow height h (the superscript that indicate dimensionless system is dropped in this equation for sake of visualization):

$$\frac{\partial h}{\partial \xi} = \frac{h - C^* - (1 - C^*)\left[\frac{(1+c(h-1))(1-C^*)(n+1+nC^*)}{(h-C^*)((n+1)h-C^*)}\right]^n}{(\alpha-1)^2c^2 - \frac{\alpha(1-c)^2}{h^2} + \frac{h}{\mathrm{Fr}^2}}, \tag{7.6}$$

This equation is then numerically solved using Adams-Bashforth-Moulton numerical method. After solved, wave properties are obtained: amplitude Δh; wavelength λ_w; and celerity c.

However, such solution only exists when Froude number is greater than a threshold value $\mathrm{Fr}_{\min}$, found through linear stability analysis (Trowbridge, 1987; Coussot, 1994; Maciel et al., 2013):

$$\mathrm{Fr}_{\min} = \frac{\vartheta}{\sqrt{\varphi^2 - 2\alpha\varphi\vartheta + \alpha\vartheta^2}}, \tag{7.7}$$

where:

$$\vartheta = n(1 - C^*); \tag{7.8a}$$

$$\varphi = \frac{(n+1)(2n+1)}{(n+1+nC^*)}. \tag{7.8b}$$

Note that $\mathrm{Fr}_{\min}$ depends on fluid rheological properties. The roll waves equation does not allow a unique solution to be found. So, a supplementary step must be executed to search for the most indicate solution to the problem. Usually, one parameter between wavelength λ_w or amplitude Δh must be imposed to find the other. Many authors have chosen wavelength imposition as it allows spectral analysis of generated waves (Dressler, 1949;

Ng and Mei, 1994; Liu and Mei, 1994; Pascal, 2006). On this work, we adopt the maximum wave amplitude imposition as it allows a more directed association to hazard intensity at stake. All steps and details of this mathematical model can be found in Maciel et al. (2013).

The model accuracy depends on the correct estimative of input parameters and on rheological properties of fluid, as will be shown. Sometimes not every parameter can be found/measured thus requiring the pre-processing stage (iterative method) to be performed before calculating all dimensionless input parameters. This preliminary iterative method is implemented so that data available is used to calculate all necessary input parameters through constitutive equations (Equations 7.1, 7.2, 7.3 and 7.5, as shown on the left side of Figure 7.1.

7.2 Site description

Berti et al. (1999, 2000); Genevois et al. (2000) did a vast work relating the characteristics of the site and from different mass movement events in the Dolomites region. In this section, we should focus on describing the site where the mass movement event happened following the observations published by those researchers who worked on the event and the site.

The Acquabona channel is localized on the Dolomites mountains, Northeast Italy, Southeast from Cortina d'Ampezzo city, having downstream the Boite river valley. Morphopedologic properties of region are prone to mass-movement natural events that occur almost every year during rainy season. The channel was equipped to allow data acquisition in three different zones, as shows 7.3(a), and for this reason is explored by Italian scientific community. The upstream region (region 1) is composed by a limestone rock basin, presenting 30° steepness. Along the channel (region 2), the superficial soil is composed by rock and gravel presenting mean inclination of 18°. Downstream (region 3), the channel reaches Boite river, crossing road Roma, and presents 7° steepness. The total length of the channel is 1632 meters.

The mixture that formed during the mass movement changed as it flowed down the channel. The fluid behavior is given by the aqueous solution of gravel (with mean diameter between 2 and 20 mm) and fine sediments (sand and clay - diameter less than 2 mm). The flow is capable of dislodge rocks and boulders up to 2 meter in diameter. Fluid fraction of rock with diam-

eter greater than 20 mm can reach 28% of total mixture mass in the body of the event, away from the surges front.

During flow evolution from upstream to downstream, an erosion process is remarked by fluid samples taken from past events (Berti et al., 1999, 2000) which can be explained by soil composition of intermediate part of the channel that is more susceptible to be eroded. Upstream, roughly 60% of fluid mixture was made by gravel while rough sands (from diameter between 65 μm and 2 mm) and fines (silt and clay with diameter smaller than 65 μm) have 35% and 5% of its composition, respectively. At intermediate length, fine sediments quantity are greater, reaching 20% in volume of fluid mixture. Downstream, fine sediments reach 30% of mixture, pointing out channel erodibility, as shows 7.3(b).

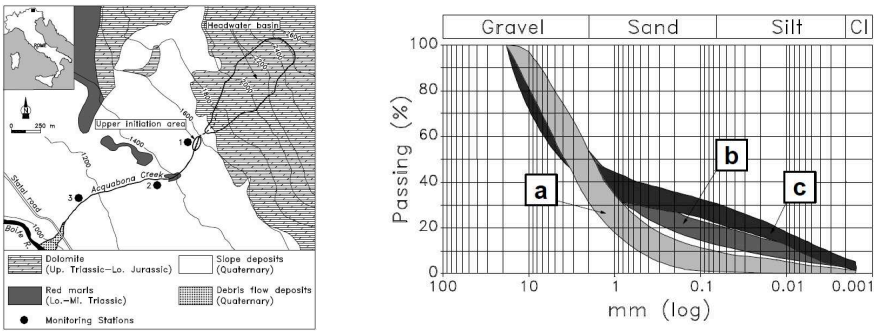

(a) (b)

Figure 7.3: From Genevois et al. (2000). 7.3(a): Location of Acquabona monitoring site. 7.3(b): Grain size distribution envelopes of Acquabona debris flows mixture composition; a - region 1, source area and upstream marls flow channel; b - region 2, downstream marls flow channel; c - region 3, deposition area.

Data collected praised pluviometry, wind speed, waves velocity (geophones), flow height (ultrasonic devices), flow superficial velocity (image processing) and pressure gauges. In the present work, we manipulated these data to estimate fluid rheological properties and flow dynamics (flow discharge). This new information, along with the reported site topography, should constitute all necessary data input for model.

7.3 Event sample

During the summer of 1998, on August 17th, a large debris flow event occurred on Acquabona channel and data were collected and published by (Berti et al., 2000). This data is used here as a test case to verify the representativity of the mathematical model presented before.

Measurements from pluviometer at inlet station showed that the rain that initiated the event reached 25 mm during 30 minutes and that the a first surge happened after 45 minutes of rain, when rainfall reached 20 mm. The total volume displaced estimated was 8000-9000 m^3.

Startup mechanisms of bed mobilization were elucidated and discussed by the authors in details. However, in this work we identified a particular feature in the event of August 17th, 1998: the mass movement registered present a roll waves-like free surface evolution. More than 15 surges (as mentioned by (Berti et al., 2000)) of mud and debris were identified during 35 minutes after the first surge, as shows Figure 7.4. The idea that will be pursued in this work is that the referenced sequence of surges could have formed a roll waves-like pattern.

From a practical point of view, the stage where the wave train is detected seems random and waves with different amplitude, celerity and wavelength are measured. However, roll waves are a permanent free surface instabilities. They are generated by spatial-temporal disturbances (Di Cristo and Vacca, 2005) in the flow which can be regular or random. In this case, we deal with a natural phenomenon where a broad set of frequencies could have disturbed the system. This could explain the variability of wave patterns noticed and the unsteadiness of waves, being more like a transitional regime.

To make an application of a mathematical model possible, we should identify a well-behaved set of waves which could be a good example of a roll waves formation in quasi-steady configuration. In this way, we gathered the results, calculated mean values of them, which allowed us to acquire the necessary input parameters for the simulation of a typical case, which could be representative of the natural waves measured. The waves identified by A, B, C, D and E on Figure 7.4 present a relatively well-behaved amplitude and wavelength when compared to others waves. We identify the end of the wave train at 1308 seconds.

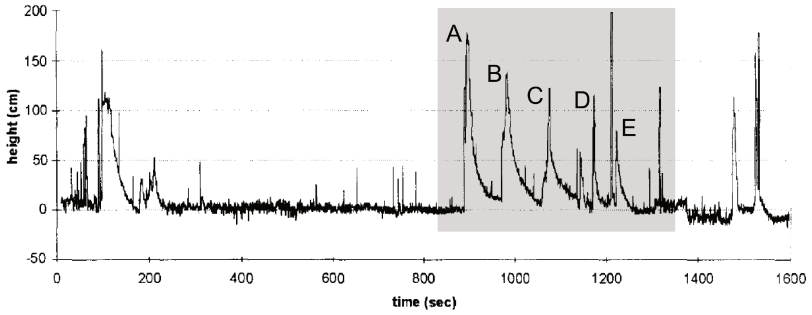

Figure 7.4: Measurements from station 3, downstream channel, collected through ultrasonic equipment on August 17th, 1998, related by Berti et al. (2000). Highlighted wave train identified as possible roll wave formation.

7.4 Parameters gathering

For the specific event of Acquabona creek, some necessary parameters required for roll waves model was missing, namely the mean flow height and velocity (h_0 and u_0 respectively), and also fluid rheological properties. The data shown and analyzed in this section is part of the pre-processing stage, referenced on Figure 7.1. First of all, results collected from pressure transducer showed that fluid pressure was equal to the bottom normal stress, thus leading to the conclusion that hydrostatic conditions is applicable. This observation allows employment of the model presented before.

Qualitative observations and data collected from soil showed that material density (from rocks, gravel and sands) should be around 2000 kgm^{-3}. Then, from mass concentration $\phi_m = 60\%$ (Zanuttigh and Lamberti, 2007), we can compute volume concentration ϕ_v as 43% and mixture density 1430 kgm^{-3}. For the compounded mixture (water + clay or water + fine sand + clay) investigated in this work, rheometric studies from Coussot (1994), Piau (1996), Huang and Garcia (1998), Santos (2003), Maciel et al. (2009) and many others proved that neglecting sedimentation effects, fluid rheology can be described by the Herschel-Bulkley non-linear rheological model, in permanent simple shearing conditions. As explained by Ancey (2007), mixtures mainly composed by clay (colloidal mixtures) have strong non-Newtonian behavior and yield stress exponentially increase with material concentration. Based on experimental rheological studies (Coussot and Piau, 1994; Remaître et al., 2005; Ancey, 2007; Maciel et al., 2009), yield stress (τ_0) is roughly estimated around 200 Pa. Concerning index flow, some results show that it stabilizes around 0.30, which is not far from 1/3

calibrated for French torrential lava by Coussot (1994). Although difficulty to predict rheological parameters, consistency index K_n can be estimated from 50 to 1000 Pas^n by the same works.

Freestream velocity u_∞ was recorded by Berti et al. (2000) through video and image processing. Values obtained after the first surge and before the wave train ($t < 900$ s) suggest that mean freestream velocity was about 3.46 ms^{-1}. Wave celerity and amplitude are related on left side of Table 7.1. Measurements of water depth from ultrasonic device is not completely reliable, since the channel was eroded during the event (channel bottom reference is lost). The iterative method (previously explained on section 7.1) was then applied using the other parameters found (fluid characteristics, free surface velocity and wave celerities) to calculate such information. Using the available data, the iterative method was performed using equations 7.2, 7.3 and 7.5. Values for u_0 and h_0 were found for each wave, as shown in the right side of Table 7.1. Mean values were also calculated, as shown in the last line of Table 7.1, using mean values for waves celerities and amplitudes. The method was initialized assuming $u_0 = u_\infty$ and $\alpha = 1$. Calculations follow in loop until all parameters have values that have converged.

Table 7.1: Waves properties collected from Berti et al. (1999) and flow properties calculated using Maciel et al. (2013) model. *: mean value calculate for column; $^+$: calculated using model, based on mean values.

Wave	Time (s)	From Berti et al. (1999)		Using Maciel et al. (2013)			
		c (ms^{-1})	Δh (m)	h_0 (m)	u_0 (ms^{-1})	K_n (Pas^n)	α
A	895	6.67	1.58	1.19	2.88	808	1.09
B	982	5.80	1.28	0.62	2.93	303	1.08
C	1075	7.69	1.07	2.05	2.85	1736	1.10
D	1142	5.88	1.06	0.67	2.93	342	1.09
E	1175	5.56	0.75	0.49	2.97	206	1.08
Mean		6.32*	1.15*	0.94$^+$	2.89$^+$	572$^+$	1.09$^+$

To assume a typical or expected roll waves pattern to travel along Acquabona creek, the mean values from Table 7.1 should be taken as reference to perform one single simulation which was here called "expected" wave. As explained in section 7.1, this analysis gives the maximum expected wave properties for a given scenario. All input parameters for expected waves

are summarized in Table 7.2.

Table 7.2: Input parameters for 1D model simulation for expected wave based on mean value for wave velocity propagation.

Input Parameters		Dimensionless Parameters	
u_0 (ms^{-1})	2.89		
h_0 (m)	0.94	n	0.30
c (ms^{-1})	6.32	Fr	0.95
θ (°)	7	C^*	0.12
ϕ_v (%)	43	$\mathrm{Fr}_{\mathrm{min}}$	0.21
τ_0 (Pa)	200	$36 < \mathrm{Re} < 740$	

7.5 Prediction results

Results from roll waves properties are shown on Table 7.3. Expected wave amplitude Δh_e was compared to the mean amplitude from event measurements and also to each wave amplitude, showing overall capability of model to represent a series waves originated from an unknown disturbance source. The discrepancy/uncertainty of model was used to evaluate the quality of the results where: $e_{\Delta h} = (\Delta h_e - \Delta h)/\Delta h$.

Table 7.3: Output data from mathematical/numerical simulation from 1D model to respect of Acquabona case-scenario from August 17th, 1998. Results are presented for each wave (from A to E) and for the expected wave based on mean flow properties.

Wave	c (ms^{-1})	Δh (m)	$e_{\Delta h}$%
Expected	6.32	1.05	
A	6.67	1.58	-24
B	5.80	1.28	-36
C	7.69	1.07	48
D	5.88	1.06	-19
E	5.60	0.75	-6
Mean	6.32	1.15	-8

The first evidence is that simulations do not present satisfactory amplitudes for each wave separately. However, when comparing to mean amplitude of wave train selected, the model would be rather capable to identify the proper scale of waves amplitude presenting difference of 8%. To understand the variability of results and a possible source of discrepancies, we evaluated the effects of non-Newtonian properties on results in the following section 7.6.

7.6 Non-Newtonian effect on maximum wave prediction

Rheological properties of fluid play an important role on waves properties. Based on typical results given by the model, we evaluated how would wave's amplitude change with rheological parameters. The assumption that sediment concentration would change along the channel as bed erosion advanced is plausible and verified by (Berti et al., 1999, 2000).

As can be observed in Figure 7.5, for weak non-Newtonian effects (smaller yield stress and greater index flow), waves amplitude decrease. Conversely, for strong non-Newtonian effects (greater yield stress, and smaller index flow), the opposite is noticed.

Choosing two extreme cases, as discriminates Table 7.4, waves amplitude can vary depending on non-Newtonian effects, yield stress and index flow. Given the set of parameters, a less non-Newtonian fluid would generate roll waves amplitudes 20% smaller than the expected case, . The opposite happens for more non-Newtonian fluids, as they increase roll waves amplitudes in 6% in comparison to expected waves amplitude, as illustrates Figure 7.6. Then, the variation in time of fluid composition could explain the observed scattering of wave height data reported by Berti et al. (2000). Qualitatively, we noticed that fluid rheological properties can also affect wavelength/period, as shows Figure 7.6.

7.7 Roll waves modeling as a risk assessment tool

From an Engineering point of view, relation between specific discharge and the mean flow height allows further identification of risks at stake during an event. The employment of a proper friction law is, most of the time,

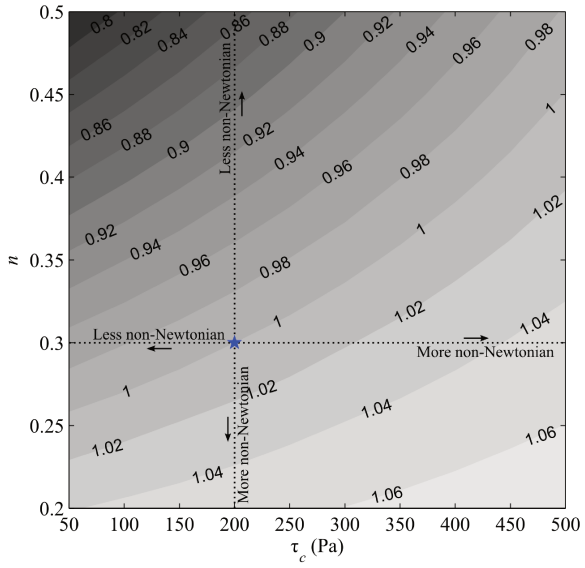

Figure 7.5: Influence of rheological properties on waves amplitudes Δh normalized by expected wave amplitude $\Delta h_e = 1.05$ m. The star indicates properties chosen for expected roll waves prediction.

Table 7.4: Output data from mathematical/numerical simulation for expected wave when varying rheological properties of mud. The range of rheological properties is in agreement with research from the literature (Ancey et al., 1999; Maciel et al., 1997).

	n	τ_0 (Pa)	α	C^*	Δh (m)
Less non-Newt.	0.5	50	1.14	0.03	0.82
Expected	0.3	200	1.09	0.12	1.05
More non-Newt.	0.2	500	1.05	0.33	1.13

an important matter, since they interfere on correction coefficients that can help guarantee safety of a structure, for example. An analysis based on different friction laws is then proposed to illustrate the representativity of each model. Considering the following:

- Turbulent - Chézy-Manning-Strickler friction law:

$$q_{0Ch} = K_s h_{0Ch}^{\frac{5}{3}} \tan\theta^{\frac{1}{2}} \tag{7.9}$$

where $K_s = 21.1/D_{84}^{1/6}$ ($\mathrm{m}^{1/3}\mathrm{s}^{-1}$) is the Strickler coefficient for a bed roughness of D_{84} (Chaudhry, 2008). D_{84} is estimated based on grain

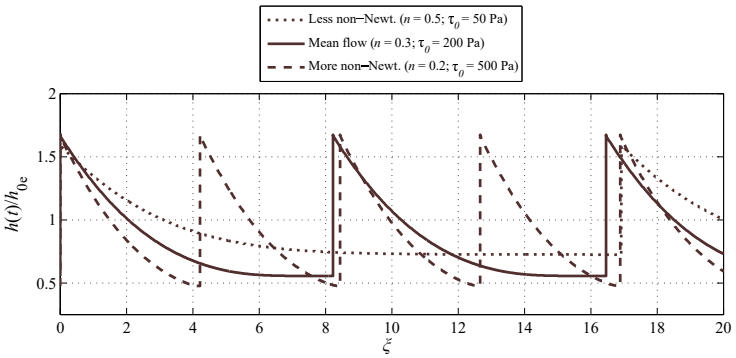

Figure 7.6: Influence of yield stress τ_0 on waves profiles $h(t)$. Profiles are scaled to each mean flow height h_0 and showed as function of dimensionless longitudinal coordinate ξ.

size distribution (Berti et al., 2000);

- Laminar, Newtonian flow

$$q_{0N} = \frac{\rho g \sin\theta}{3\mu} h_{0N}^3 \tag{7.10}$$

for μ being the Newtonian absolute viscosity of the mixture, $\mu = 200$ Pas, estimated from apparent viscosity reported by Genevois et al. (2000).

- Laminar, non-Newtonian flow

$$q_{0NN} = \left(\frac{n}{n+1}\right)\left(\frac{nC^* + n + 1}{2n+1}\right)\left[\frac{\rho g \sin\theta}{K_n}\left(h_{0NN} - \frac{\tau_0}{\rho g \sin\theta}\right)^{n+1}\right]^{\frac{1}{n}} h_{0NN}; \tag{7.11}$$

from Maciel et al. (2013) model. Parameters used for this simulations follow data from section 7.6;

Figure 7.7 shows the dependency of mean flow height on specific discharge, for all the friction laws enumerated before, where turbulent (Chézy-Manning-Strickler) model is generally taken as the reference. For a fixed discharge q_0, h_0 can reach considerable higher values depending on fluid properties. For discharges lower than discharge in Acquabona event estimated based on Equation 7.11 ($q_{acqua} = 2.72$ m^{2}s^{-1}), flow height can reach values three times higher considering a simple Newtonian model, and

four times greater when consider non-Newtonian rheology as shown in Figure 7.7. Non-Newtonian parameters uncertainties can considerably affected the prediction of mean flow height, as shows the vertical bar. Thus, for the event here studied, a turbulent inviscid approach would not be able to safely estimate flow height, given the discharge.

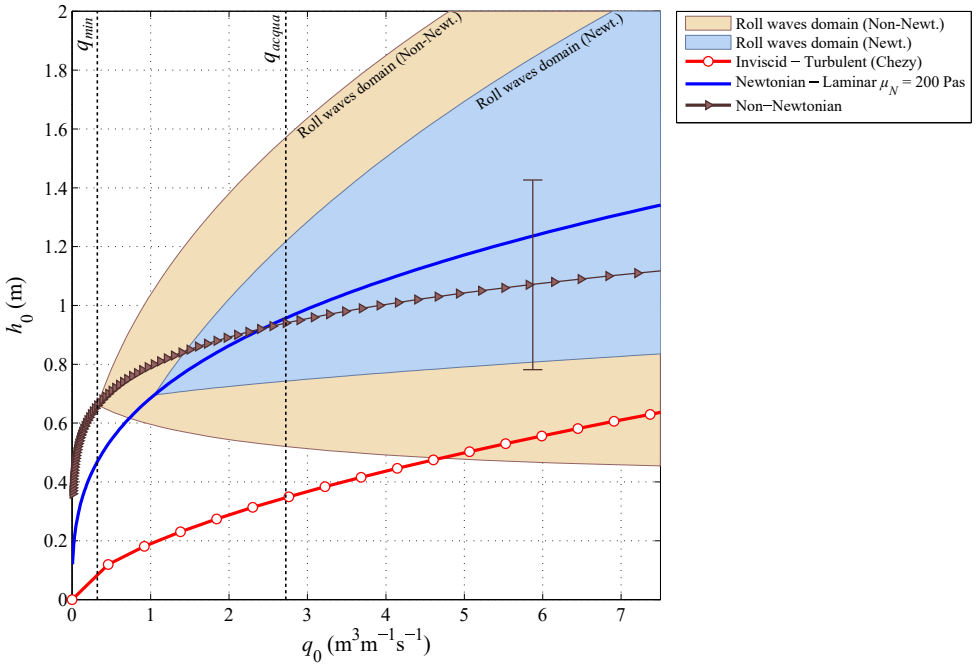

Figure 7.7: Mean flow height h_0 as function of the specific discharge q_0 for different friction laws. Curves represent different frictions laws. Shaded zone shows amplitudes of roll waves for the respective friction law. q_{acqua} represents specific discharge in the Acquabona creek for the event here studied based on Equation 7.11. q_{min} is the minimum specific discharge required for roll waves to appear in Acquabona creek given the non-Newtonian rheology. Vertical bar indicates prediction of mean flow height using cases from Table 7.4, for less and more non-Newtonian fluids.

One important feature to notice is the minimum discharge for roll waves to be prone to be generated. For turbulent inviscid flows, low discharge would be required, since the channel have high slope. For Fr > 2, $q_{\mathrm{RW}_{Ch}} > 0.002$ m^{2}s^{-1}, then most of the inviscid-turbulent curve shown in Figure 7.7 represent a favorable domain for roll waves appearance. Such value would

increase for laminar flows: $q_{\mathrm{RW}_N} > 1.07$; and $q_{\mathrm{RW}_{NN}} > q_{min} = 0.35$ m^{2}s^{-1}. This fact indicates that roll waves could have appeared for specific discharge much lower than q_{acqua}. Since turbulent inviscid approach would fail to properly predict the mean flow height, we evaluated roll waves for the two other cases. The roll waves domain for viscous laminar flows present waves that have smaller amplitudes than those for the non-Newtonian domain. This results points out that, in any case scenario, in addition to the non-Newtonian rheology, roll waves model should be considered to predict the event of Acquabona creek in 1998.

Chapter 8

Search for a more complex model

8.1 Introduction

One problem in fluid mechanics that recently has been more addressed is the dynamics of Herschel-Bulkley fluids in presence of a porous medium. Even though non-Newtonian fluids have been largely studied on that matter (Sabiri and Comiti, 1995; Sochi, 2010), the presence of yield is not easily assigned. The kernel of the problem resides in the interaction between the nature of the fluid (mixture, suspension, etc.) and the void geometry that constitutes the porous medium. When dealing with suspensions, for example, particles can be clogged inside the voids by many capture processes, which then would change the porosity of the medium over time (Herzig et al., 1970), thus completely changing the problem itself. However, when dealing with oil industry problems and polymers, yield non-Newtonian fluids can sometimes interact with porous boundaries.

The problem that is undertaken in this chapter is how dynamics of a non-Newtonian fluid flow presenting Herschel-Bulkley rheology would change due the presence of a permeable medium as boundary condition. Open-channel flow was considered, so that the permeable medium, or porous medium, was found in the bottom of the channel. The porous medium is composed by fixed particles of diameter D, arranged randomly. This problem could somehow not only be related to technical and industrial issues but also be related to natural flows, where conditions allow.

Here again, the conditions announced on section 2.3 are valid. The conservation equations are represented by the system of equations 2.23a, 2.23b and 2.23c. The difference that is present in this problem is that fluid is

allowed to flow inside the medium that composes the bed, which now is fixed[1]. The bed have a porosity p, i.e. void space in bed material sufficient permeable for flow fluid to fill them in. At this point, we should have what is called a Darcian-like flow, as illustrates Figure 8.1. For the steady and uniform case, velocity and free surface height are both constant values u_0 and h_0, respectively. Inside the porous medium a flow is also established with velocities u_p and v_p.

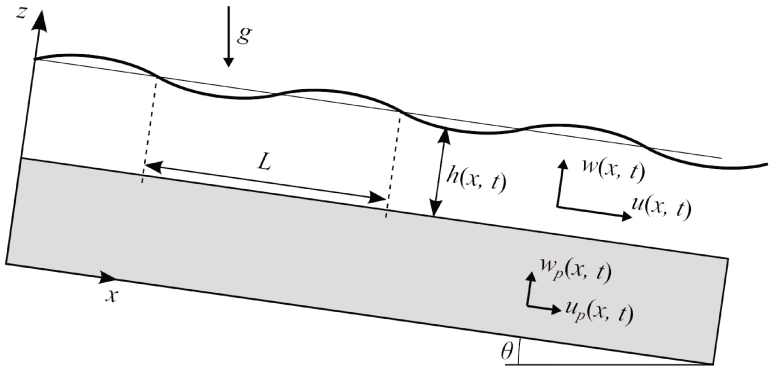

Figure 8.1: Schematic representation of flow. The non-Newtonian fluid is now flowing inside the porous bed.

8.2 Mathematical development

8.2.1 Boundary Condition

It is required to find the relationship between pressure drop on porous medium and Darcian velocity (u_p, v_p) to properly assume the boundary conditions on the interface bed-fluid. A large review on the subject is presented on Chhabra et al. (2001) where dynamics of non-Newtonian fluids (power-law fluids) on different porous media are related. In that work, the authors made clear that fluid properties greatly change its dynamics inside tortuous paths affecting the macro behavior, which is summarized by a Darcy's Law type relation. Following previous works from Beavers and Joseph (1967) and Rao and Mishra (2004), we assumed continuity of shear

[1]In this case, either flow is saturated and there is a balance between erosion and deposition, and bed is plane; or flow erosional capacity is no longer sufficient to entrain bed material

rate on the interface through the following boundary condition:

$$\left.\frac{\partial u}{\partial y}\right|_{y=0} = \frac{\chi}{k^{\frac{1}{n+1}}}(u - u_p). \tag{8.1}$$

where ξ is a form factor of voids inside the porous medium and k is the permeability of the porous medium.

The shearing conditions exhibited by equation 8.1 can be assumed as the non-Newtonian effect from yield stress is comprised by means of longitudinal Darcian velocity u_p. The other boundary condition is related to the normal velocity in the porous medium which, on the interface, should not vary once it is inside the boundary layer. So:

$$v_p = v, \quad \text{for } y = 0. \tag{8.2}$$

Recalling the recent work from Chevalier et al. (2013), those authors present an adaptation of Darcy's Law to Herschel-Bulkley fluids based on experimental data for a polymeric solution of Carbopol flowing through a porous medium. Chevalier et al. advised that the relation between pressure drop and Darcian velocity should have the form

$$-\frac{\partial p_p}{\partial x} = \frac{\tau_0}{k_I} + \frac{K_n}{k_K}u_p^n, \tag{8.3}$$

where k_I and k_K, defined in this thesis, are porous medium parameters relating shape, dispersion of material inside the pores and voids of porous medium. Both parameters correspond to the permeability used to define properties of porous medium. The first parameter k_I we call here inertial permeability. It represents how the structure of the porous medium coupled to the non-Newtonian rheology opposes the movement of the fluid. The second one we call kinematic permeability: its understand as the classical permeability coefficient, and it measures the ability of the porous material to allow fluids to flow through it. Following the work previously mentioned (Chevalier et al., 2013), both variables should be function of the shape of the porous medium, although the second one also depends on the fluid rheology, as shows Equations 8.4 and 8.5 for a fixed porosity:

$$k_I = \frac{D}{4}; \tag{8.4}$$

$$k_K = \frac{D^{n+1}}{4(6 + 2/n)^n}, \tag{8.5}$$

which is called in the present work as inertial and kinetic permeability, respectively. For a variable porosity, Equation 8.5 could be represented as

points Christopher and Middleman (1965) through Equation 8.6:

$$k_K = \frac{6}{25}\left(\frac{np}{3n+1}\right)^n \left[\frac{pD}{3(1-p)}\right]^{n+1}. \tag{8.6}$$

The concepts here presented, adapted from Darcy's Law for Newtonian fluids, can only be guaranteed for non-Newtonian fluids as long as fluids do not present special interactions with the medium. Filtration and clogging, for example, which have been taken into account during experiments from Chevalier et al. (2013) do not properly fit when solid particles with considerable size are in suspension. Particles in suspensions must have mean diameter much smaller than pore space, so that no clogging of microchannels happens, and porosity is kept constant. Then, adapting Darcy's law for a Herschel-Bulkley fluid,

$$u_p = -\left(\frac{k_K}{K_n}\right)^{1/n}\left[\left(\frac{\partial P_p}{\partial x} + \frac{\tau_0}{k_I}\right)^{1/n} - \rho g \sin\theta\right]; \tag{8.7}$$

$$\frac{\partial u_p}{\partial x} + \frac{\partial v_p}{\partial y} = 0; \tag{8.8}$$

$$\frac{\partial P_p}{\partial y} = -\rho g \cos\theta, \tag{8.9}$$

where P_p represent total pressure in the porous medium and $P_p = P$ for $y = 0$. Hydrostatic pressure is assumed, and scales between flow over and inside the bed are estimated. Then, pressure gradient inside porous medium is the same as in the flow thus leading to the pressure scale

$$P_0 \sim K_n \left(\frac{u_0}{h_0}\right)^n \frac{L_0}{h_0}. \tag{8.10}$$

From equation 8.8, we reached a scale to the longitudinal velocity in the porous medium to be:

$$U_p \sim \left(k_K \frac{u_0^n}{h_0^{n+1}} - \Omega_f\right)^{\frac{1}{n}}, \tag{8.11}$$

where $\Omega_f = \frac{k_K}{k_I}\frac{\tau_0}{K_n}$ is the ratio between the inertial threshold and the kinematic resistance of porous medium to fluid flow.

For matter of simplification, consider a fluid that have no yield stress, so $\tau_0 = 0$. Then $\Omega_f = 0$ and U_p becomes:

$$U_p \sim \left(k_K \frac{u_0^n}{h_0^{n+1}}\right)^{\frac{1}{n}} = \frac{k_K^{1/n}}{h_0^{1+1/n}} u_0. \tag{8.12}$$

As pore scale is much smaller than flow scale ($h_0^{n+1} \gg k_K$), then $k_K/h_0^{n+1} \ll 1$, and:

$$U_p \ll u_0. \tag{8.13}$$

Then, the boundary conditions for porous medium (on the interface between fluid flow and porous bed) are simplified into

$$\left.\frac{\partial u}{\partial y}\right|_{y=0} = \frac{\chi}{k_K^{\frac{1}{n+1}}} u; \qquad v|_{y=0} = 0. \tag{8.14}$$

The boundary condition can also be found in dimensionless form, which allow the understanding of properties that rule over the boundary law. The upper asterisk indicate dimensionless variable scaled to mean flow properties. The following Equation 8.15:

$$\left.\frac{u_0}{h_0}\frac{\partial u^*}{\partial y^*}\right|_{y^*=0} = u_0 \frac{\chi}{k_K^{\frac{1}{n+1}}} u^*|_{y^*=0} \rightarrow$$

$$\left.\frac{\partial u^*}{\partial y^*}\right|_{y^*=0} = \frac{1}{(1-C^*)\gamma} u^*|_{y^*=0}. \tag{8.15}$$

where $u^* = u/u_0$, $y^* = y/h_0$, $\gamma = k_K^{\frac{1}{1+n}}/(\chi y_0)$ and $(1-C^*) = y_0/h_0$.

8.2.2 The velocity profile $u(y)$

For hydrostatic pressure distribution, one can reach that shear rate is given as shows Equation 8.16.

$$\frac{\partial u}{\partial y} = \left(\frac{\rho g (h_0 - y)\sin\theta - \tau_0}{K_n}\right)^{\frac{1}{n}}. \tag{8.16}$$

Then, solving Equation 8.16 for u, the velocity is finally written as:

$$u(y) = \left(\frac{n}{n+1}\right)\left[1 - \left(1 - \frac{y}{y_0}\right)^{\frac{n+1}{n}} + \left(\frac{n+1}{n}\right)\gamma\right]\left(\frac{\rho g \sin\theta}{K_n} y_0^{n+1}\right)^{\frac{1}{n}}, \tag{8.17}$$

where

$$\gamma = k_K^{\frac{1}{1+n}}/\chi y_0. \tag{8.18}$$

On the plug region ($y_0 < y < h_0$), the velocity is constant equal to $u_{y_0} = u(y = y_0)$ namely plug flow velocity (equation 8.19):

$$u_{y_0} = u(y = y_0) = \left(\frac{n}{n+1}\right)\left[1 + \left(\frac{n+1}{n}\right)\gamma\right]\left(\frac{\rho g \sin\theta}{K_n} y_0^{n+1}\right)^{\frac{1}{n}}, \tag{8.19}$$

where $y_0 = h_0 - \tau_0/(\rho g \sin\theta)$ is the plug flow height which can be rewritten as $y_0 = h_0(1 - C^*)$.

An important feature introduced by a porous bottom is that the interface allows flow to "slip" on the interface (Chen and Zhu, 2008). At the bottom ($z = 0$),

$$u_B = u(y = 0) = \gamma \left(\frac{\rho g \sin\theta}{K_n} y_0^{n+1} \right)^{\frac{1}{n}}, \tag{8.20}$$

where u_B is the bottom velocity, on the interface between the porous medium and the open-channel flow.

8.2.3 Mean flow velocity u_0

The mean flow velocity is calculated by vertically averaging the velocity profile:

$$u_0 = \frac{1}{h_0} \int_0^{h_0} u(y)\,\mathrm{d}\,y = \frac{1}{h} \left[\int_0^{y_0} u(y)\,\mathrm{d}\,y + \int_{y_0}^{h_0} u(y)\,\mathrm{d}\,y \right]. \tag{8.21}$$

Solving the integrals, we find that mean flow velocity is:

$$u_0 = \left(\frac{n}{n+1} \right) \left[\frac{1 + n + nC^*}{2n+1} + \left(\frac{n+1}{n} \right) \gamma \right] \left(\frac{\rho g \sin\theta}{K_n} y_0^{n+1} \right)^{\frac{1}{n}}. \tag{8.22}$$

8.3 Verification of solution for less complex conditions

The solution can be verified for fixed beds (non-porous) by making $\gamma = 0$. Also, for less complex rheologies simple substitution of parameters can be used to reach less complex solutions.

8.3.1 Bingham rheology

For a Bingham-type rheology, fluid presents yield but there is a linear relationship between shear rate and shear stress. In simple shearing conditions the rheological model is:

$$\tau = \tau_0 + \mu_B \left(\frac{\partial u}{\partial y} \right), \quad \text{for} \quad \tau > \tau_0, \tag{8.23}$$

where μ_B is the Bingham plastic viscosity and τ_0 the yield stress, as we know. Comparing Equation 8.23 with Equation 2.21, we see that $n = 1$.

Mean flow velocity will then be:

$$u_0 = \left(\frac{2 - C^*}{6} + \gamma\right)\left(\frac{\rho g \sin\theta}{\mu_B}\right) y_0^2. \tag{8.24}$$

and $\gamma = k_K^{\frac{1}{2}}/(\chi h_0)$.

For a non-porous bed, the solution is:

$$u_0 = \left(\frac{2 - C^*}{6}\right)\left(\frac{\rho g \sin\theta}{\mu_B}\right) y_0^2. \tag{8.25}$$

8.3.2 Power law rheology

For a power law-type rheology, no yield exists however a non linear relationship is observed between shear rate and shear stress. In simple shearing conditions the rheological model is:

$$\tau = \mu_n \left(\frac{\partial u}{\partial y}\right)^n, \tag{8.26}$$

where μ_n is the plastic viscosity and $n$is the power law flow index. Comparing Equation 8.26 with Equation 2.21, we see that $\tau_0 = 0$.

Mean flow velocity will then be:

$$u_0 = \left(\frac{n}{2n+1} + \gamma\right)\left(\frac{\rho g \sin\theta}{\mu_n} h_0^{n+1}\right)^{\frac{1}{n}}, \tag{8.27}$$

and $\gamma = k_K^{\frac{1}{1+n}}/(\chi h_0)$.

For a non-porous bed, the solution is:

$$u_0 = \left(\frac{n}{2n+1}\right)\left(\frac{\rho g \sin\theta}{\mu_n} h_0^{n+1}\right)^{\frac{1}{n}}. \tag{8.28}$$

8.3.3 Newtonian rheology

For a Newtonian-type rheology, no yield exists and a linear relationship is found between shear rate and shear stress. In simple shearing conditions the rheological model is:

$$\tau = \mu \left(\frac{\partial u}{\partial y}\right), \tag{8.29}$$

where μ is the dynamic viscosity. Comparing Equation 8.29 with Equation 2.21, we see that $\tau_0 = 0$ and $n = 1$.

Mean flow velocity will then be:

$$u_0 = \left(\frac{1}{3} + \gamma\right)\left(\frac{\rho g \sin\theta}{\mu}\right) h_0^2, \tag{8.30}$$

and $\gamma = k_K^{\frac{1}{2}}/(\chi h_0)$.

For a non-porous bed, the solution is:

$$u_0 = \frac{\rho g \sin\theta}{3\mu} h_0^2. \tag{8.31}$$

Chapter 9

Numerical simulations

To verify the mathematical solution proposed in chapter 8, numerical simulations were carried in FLUENT©[1] using experimental data of carbopol solutions from the literature. Numerical schemes used to solve equations were based on finite volume method for steady laminar flow (Patankar and Spalding, 1972; Versteg and Malalasekera, 1995). For the pressure-velocity coupling, semi-implicit method for pressure-linked equations-consistent (SIMPLEC) method was applied (VanDoormal and Raithby, 1984). Pressure interpolation was conducted using the pressure staggering option (PRESTO) routine. For the convective terms, a second order user-defined scalar was used and for the free surface computation, the implicit volume of fluid high resolution interface capturing (HRIC) scheme was chosen (Ubbink and Issa, 1999). Two-dimensional domain was meshed using non-uniform trilateral polygons. The refinement level of the meshing depended on the proximity to the objects composing the bed. The mesh was dense ($\approx 10^{-4}$m cross-sectional length for cell grids) for the carbopol phase (inside the porous medium and in free flow) and sparse for the air phase (($\approx 10^{-2}$m).

The non-Newtonian rheology is implemented in the software using Papanastasiou (1987) Herschel-Bulkley rheological model:

$$\tau = \tau_0 \left(1 - e^{-m\dot{\gamma}}\right) + K_n \dot{\gamma}^n \tag{9.1}$$

where the exponent m is responsible for the growth rate of stress to respect the shear rate $\dot{\gamma} = \frac{\partial u}{\partial y}$. Such exponent is set given mesh conditions.

[1] FLUENT 6.3., User's Guide, Fluent Incorporate, 2008.

9.1 Numerical modeling

The model test chosen was based on previous studies from Prinos et al. (2003) and Chan et al. (2007). The porous bed was modeled as a macroscopic porous medium composed by 2D disk of diameter D, uniformly spaced in the domain between impermeable wall at $y = 0$ and $y = h_p$, as shows Figure 9.1. l_1 is the vertical distance between first disk and impermeable wall and l_2 is vertical distance between disks. The porous bed element shown has length L_p and is periodic along channel length. The porosity is then calculated by total porous bed element domain ($S_p = h_p L_p$) and wall disks surface (S_w) as $p = 1 - S_p/S_w$.

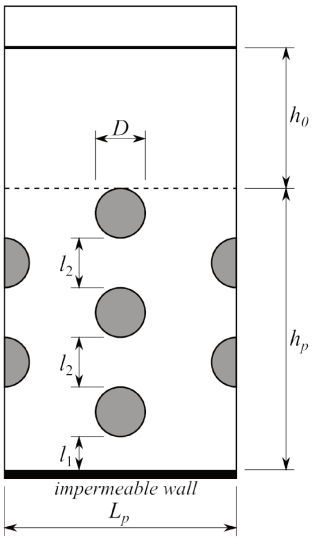

Figure 9.1: Schematic illustration of computational element of the porous bed. The element repeats its pattern along the total length of computational domain where the bottom impermeable wall is the lower boundary of the domain.

Geometry of bed and test-fluid properties were fixed constant following parameters shown on tables 9.1 and 9.2, respectively. The fluid chosen for simulations was based on Leite (2009) and Roberts and Barnes (2001)'s experiments. Carbopol solutions are versatile fluids that have been largely employed on non-Newtonian fluid experiments. Gravity and inlet discharge were then controlled to obtain different experimental runs described Table 9.3. The index Q on test run identifies the inlet discharge, I the slope and F the fluid.

Table 9.1: Geometrical characteristics of the porous bed element.

Geometry	
h_p	5.5 cm
L_p	3.0 cm
D	1.0 cm
ϕ	0.7715

Table 9.2: Rheological properties of employed fluids. The fluids were carbopol solutions made in laboratory by Leite (2009) and Roberts and Barnes (2001).

Fluid properties			
	Leite (2009)	Roberts and Barnes (2001)	
Test fluid (F)	1	2	3
Carbopol sol. at	0.13%	0.08%	0.10%
ρ (kg/m^3)	1016	1016	1016
n	0.44	0.50	0.45
K_n (Pas^n)	3.36	1.40	3.75
τ_0 (Pa)	4.26	3.00	10.00

9.2 Numerical results

Flow height is detected where the isocontour for 0.5 was observed. Velocity field was then analyzed and used to compute a mean flow velocity profile and mean flow velocity. These results were then used to compute dimensionless numbers that help understand flow regime (Reynolds number - Equation 2.22; Froude number - Equation 2.29; and C^* - Equation 2.24).

An example of the solution obtained for flow can be observed on Figure 9.2 for the numerical run Q1I3F3. Expected behavior of the solution is observed. In the Figure 9.2, the flow inside the porous bed is negligible as velocity is approximately zero. On the interface between porous bed and open-channel flow (channel bottom line), a non-zero velocity is obtained. Plug flow is observed in the upper region of the profile, characteristic of yield fluids.

9.2.1 Flow inside the porous medium

Numerical results point out that Darcian velocity measured inside the porous medium ($u_{p_{\text{num}}}$) had relatively greater scale than the one predicted by the-

h

Table 9.3: Summary of numerical runs performed. Uniform flow parameters obtained are shown and characteristic dimensionless numbers. Note: experimental runs for different carbopol solutions are represented by: F1, Leite (2009) carbopol solution at 0.13%; F2, Roberts and Barnes (2001), at 0.08%; and F3, Roberts and Barnes (2001) at 0.10%.

Numerical run	u_{in} (m/s)	h_{in} (m)	θ (°)	k_K (m^{n+1})	k_I (m)	u_0 (ms^{-1})	h_0 (cm)	$u_{p_{num}}$	U_p	Re	Fr	C_*
Q1I3F1	0.20	0.11	3	$1.6{\cdot}10^{-4}$	$2.5{\cdot}10^{-3}$	0.51	4.35	$1.7{\cdot}10^{-4}$	$3.3{\cdot}10^{-5}$	26	0.77	0.19
Q1I2F2	0.20	0.11	2	$1.1{\cdot}10^{-4}$	$2.5{\cdot}10^{-3}$	0.56	3.91	$2.0{\cdot}10^{-4}$	$1.2{\cdot}10^{-4}$	60	0.92	0.22
Q1I3F3	0.20	0.11	3	$1.5{\cdot}10^{-4}$	$2.5{\cdot}10^{-3}$	0.40	5.53	$8.9{\cdot}10^{-5}$	$1.5{\cdot}10^{-5}$	18	0.54	0.35
Q1I4F3	0.20	0.11	4	$1.5{\cdot}10^{-4}$	$2.5{\cdot}10^{-3}$	0.48	4.57	$1.2{\cdot}10^{-4}$	$3.3{\cdot}10^{-5}$	22	0.72	0.32
Q1I5F3	0.20	0.11	5	$1.5{\cdot}10^{-4}$	$2.5{\cdot}10^{-3}$	0.55	3.96	$1.5{\cdot}10^{-4}$	$6.0{\cdot}10^{-5}$	25	0.89	0.29
Q1I6F3	0.20	0.11	6	$1.5{\cdot}10^{-4}$	$2.5{\cdot}10^{-3}$	0.62	3.52	$1.9{\cdot}10^{-4}$	$9.8{\cdot}10^{-5}$	29	1.06	0.27
Q1I7F3	0.20	0.11	7	$1.5{\cdot}10^{-4}$	$2.5{\cdot}10^{-3}$	0.69	3.19	$2.2{\cdot}10^{-4}$	$1.5{\cdot}10^{-4}$	32	1.23	0.26
Q2I3F3	0.25	0.11	3	$1.5{\cdot}10^{-4}$	$2.5{\cdot}10^{-3}$	0.48	5.78	$8.8{\cdot}10^{-5}$	$1.5{\cdot}10^{-5}$	24	0.64	0.33
Q2I4F3	0.25	0.11	4	$1.5{\cdot}10^{-4}$	$2.5{\cdot}10^{-3}$	0.58	4.79	$1.2{\cdot}10^{-4}$	$3.4{\cdot}10^{-5}$	29	0.84	0.30
Q2I5F3	0.25	0.11	5	$1.5{\cdot}10^{-4}$	$2.5{\cdot}10^{-3}$	0.66	4.13	$1.5{\cdot}10^{-4}$	$6.3{\cdot}10^{-5}$	34	1.05	0.28
Q2I6F3	0.25	0.11	6	$1.5{\cdot}10^{-4}$	$2.5{\cdot}10^{-3}$	0.74	3.69	$1.8{\cdot}10^{-4}$	$1.0{\cdot}10^{-4}$	39	1.24	0.26
Q2I7F3	0.25	0.11	7	$1.5{\cdot}10^{-4}$	$2.5{\cdot}10^{-3}$	0.82	3.33	$2.2{\cdot}10^{-4}$	$1.5{\cdot}10^{-4}$	43	1.44	0.25

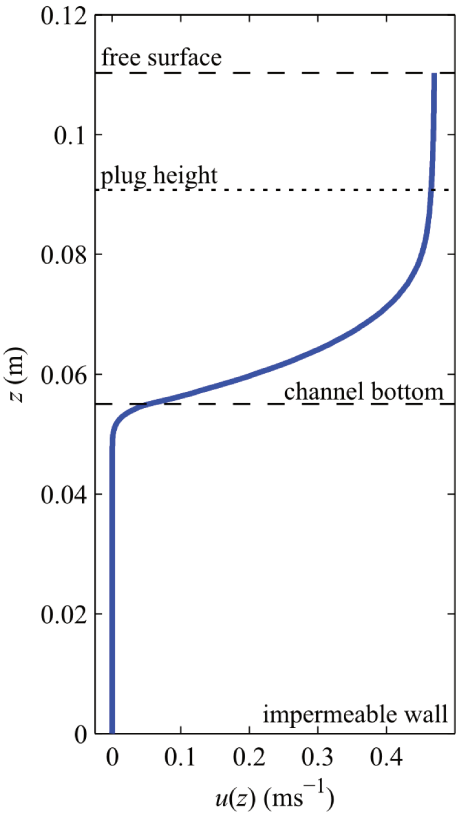

Figure 9.2: Velocity profile for numerical run Q1I3F3. Impermeable wall is located at $y = 0$. The channel bottom line ($y = h_p$) represent the interface between porous bed and open-channel flow. The plug height ($y = y_0$) identifies limit between sheared and plug zone.

ory. Figure 9.3 shows the correlation between numerical results $u_{p_{\text{num}}}$ and theoretical scale estimation U_p.

There is a linear correlation between both velocities, but displaced in the horizontal axis. The linear correlation is given by the equation:

$$U_p = 1.097 u_{p_{\text{num}}} - 9.71 \cdot 10^{-5}. \tag{9.2}$$

9.2.2 Open-channel flow

Averaged velocity field gives the velocity profile $u(y)$ representative of the numerical test. Such profile was then compared to the theoretical solution from Equations 8.17 and 8.19. Such comparison can only be done if param-

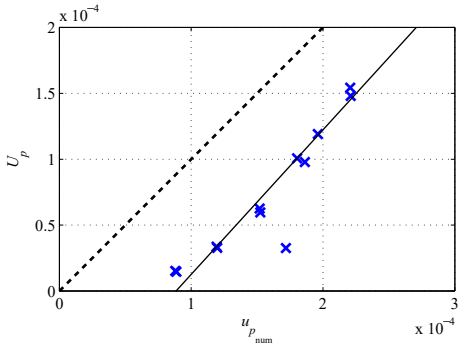

Figure 9.3: Comparison between numerical results for Darcian velocity $u_{p_{\text{num}}}$ and theoretical scale of the same velocity U_p. Dotted line indicates perfect correlation. Solid line represents interpolation of measured points.

eter χ from Equation 8.18 is properly estimated. For a internal flow (no atmospheric pressure), such value can be estimated based on the geometry of porous medium, in our case, the disposition of rods in our porosity computational element. As well for on open-channel flows, this value should vary depending on the complex interaction between flow and porous geometry. To obtain such value, the maximum correlation between discharges from both results was sought, varying χ parameter on Equation 8.18. A mean value $\chi = 0.191$ was found, which seems in agreement with previous works ($0.1 < \chi < 4$) (Beavers and Joseph, 1967; Pascal, 2006).

Then, the velocity profile can be compared, as shows 9.4 numerical runs Q1I3 and Q1I4. When comparing velocity profiles between tests with the same discharge (Figure 9.5), it is possible to identify that the behavior of curves is similar thus pointing out that theoretical relation represent those results. These results clearly show that the slip velocity, or bottom velocity $u_B = u(y = 0)$ should depend on flow and/or fluid and/or porous medium parameters, as expected (Equation 8.20).

Apart from mean flow velocity, two other characteristics velocities can be used to evaluate agreement between results and mathematical model: bottom slip velocity u_B; and plug flow velocity u_{y_0}. The first one presents a 4.8% standard deviation around 1, towards equivalence. For the second one, a standard deviation is found to be 0.3% around 0.99, thus presenting a tendency of underestimating plug flow velocity. For bottom velocity, no systematic evidence was found that could relate standard deviation and flow/porous parameters (as shows Figure 9.6). The source of such variations

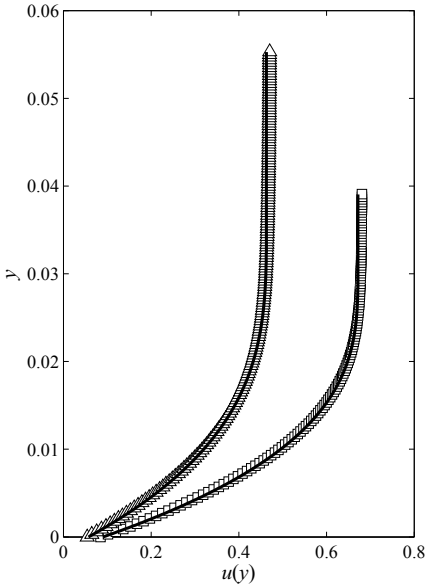

Figure 9.4: Comparison between numerical and theoretical solutions of velocity profile for tests cases Q1I3 and Q1I4.

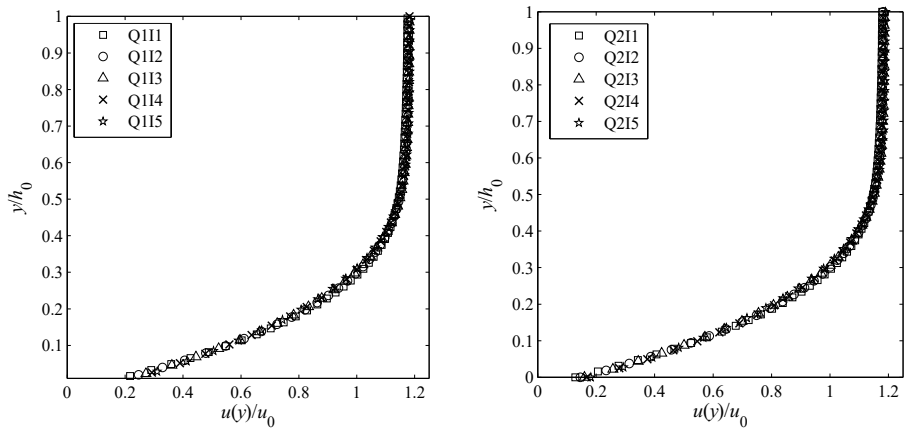

Figure 9.5: Velocity profiles for all numerical runs. Velocity $u(y)$ is scaled to mean flow velocity u_0 and vertical coordinate to mean flow height h_0.

should be locally related (flow and macro porosity structures interaction) or the boundary condition adopted would present a flaw. Flow dynamics around the objects that constitute the medium could have contributed to shape flow macro behavior, thus altering the exact value at the interface.

For the plug flow velocity, results were biased, indicating that a fundamental problem was present.

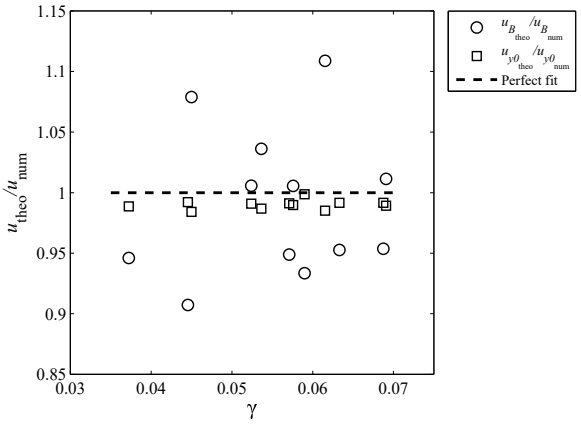

Figure 9.6: Theoretical characteristics velocities u_B and u_{y_0} scaled by numerical results as function of γ parameter.

9.2.3 Boundary conditions verification

To understand the discrepancy observed between theoretical and numerical values for the bottom velocity u_B, we looked upon the dimensionless form of the boundary condition obtained in the mathematical modeling in subsection 8.2.1, given by Equation 8.15.

As can be seen on Figure 9.7, for the numerical runs performed, great values for $(1 - C^*)^{-1}\gamma^{-1}$ point out a less representative boundary condition. For small yield stress (small C^*) considerable effect of porosity (great γ), the curve fits the boundary condition. This could indicate that the boundary conditions adopted would require further improvement to better fit the characteristics of the flow here explored. Other effects might as well contribute to the discrepancy observed as the geometry of the flow, for example, which is not explored in the present work.

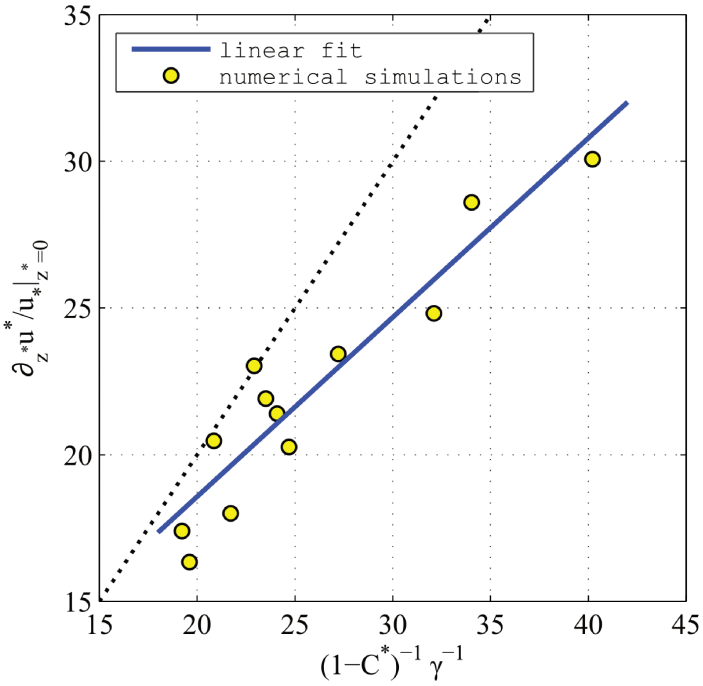

Figure 9.7: Verification of boundary condition validity. Dotted line indicate perfect correlation between theory and numerical results.

9.3 Mathematical analysis

The velocity profile $u(y)$ was studied to respect the plug velocity $u(y_0)$ which corresponds to the freestream velocity (free surface velocity), and the vertical coordinate y to respect y_0 thus scaling the problem, as shows equation 9.3.

$$U(Y) = \frac{u(y)}{u(y_0)} = \left[1 - \frac{(1-Y)^{\frac{n+1}{n}}}{1+\gamma\left(\frac{n+1}{n}\right)}\right], \tag{9.3}$$

where $Y = y/y_0$. It's also valuable to define the free surface height which should be equal to $H_0 = h_0/y_0 = 1/(1-C^*)$. Mean flow velocity U_m is then calculated as

$$\bar{U} = \frac{1}{H_0}\left[\int_0^1 U(Y)DY + \int_1^{H_0} DY\right]. \tag{9.4}$$

The effect of the porous bed over the velocity can be summarized as the promotion of a slip velocity on the interface between the bed and the flow. Figure 9.8 shows that for a solid bed ($\gamma = 0$), interface velocity $U|_{Y=0} = 0$.

However, the smallest increase in bed porosity leads to a non-zero velocity at the interface. For shear thinning fluids ($n < 1$), the interface velocity increases more rapidly with porosity.

When in presence of a yield stress, the same behavior is noticed. This effect lead to a mean flow velocity U_m which is closer to freestream velocity the higher the yield stress parameter C^*, as shows figure 9.8. This observation is in agreement with the plug zone which is greater as the yield stress increases, thus leading to a quasi-constant velocity distribution over the vertical coordinate. Numerical and, most importantly, experimental validation of the velocity profile should be employed to assure hypothesis adopted in this work. When dealing with fluid composed by sediment particles, percolation effect can hardly be avoided, thus obstructing the proper use of such mathematical development. However, for homogeneous fluids such as emulsions and gels, these assumptions should be reasonable and could be verified experimentally.

Supposing the same discharge ($q = u_0 h_0$) entering a non-porous bed ($\gamma = 0$), Equation 9.4 can be used to calculate the mean flow velocity in these conditions $\bar{U}|_{\gamma=0}$, and compared to the one when a porous bed is present. Figure 9.9 shows that a significant increase in mean flow velocity is obtained when fluid have low yield stress level. However, high level of yield indicates that a great plug zone is formed, thus diminishing the influence of the slip velocity, therefore the influence of porosity, as we can see in the last picture from Figure 9.9. These observations, especially concerning the increase of velocity, corroborate the influence of the porous bed.

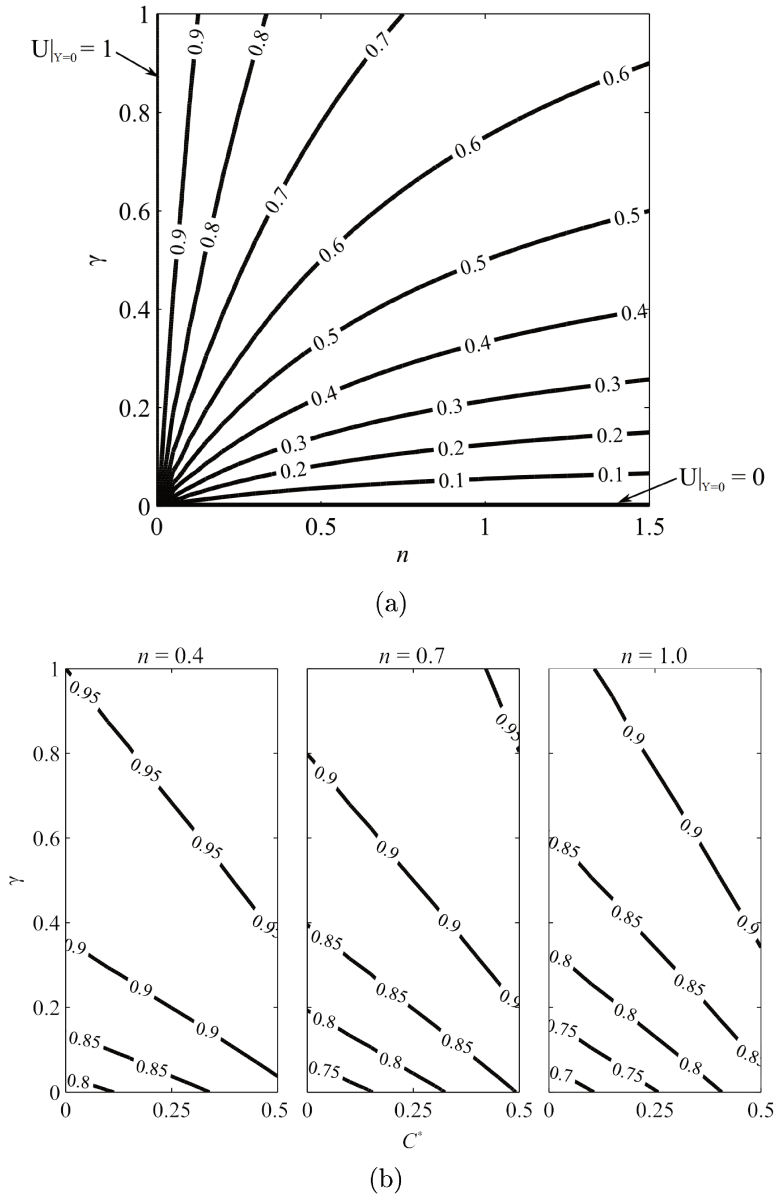

Figure 9.8: Analysis of rheological properties and porous medium on flow velocity. 9.8(a): contour of velocity at the interface $U|_{Y=0}$ as function n and γ, for $C^* = 0$; 9.8(b): contour of mean flow velocity $\bar{U}$ as function C^* and γ for different values of n.

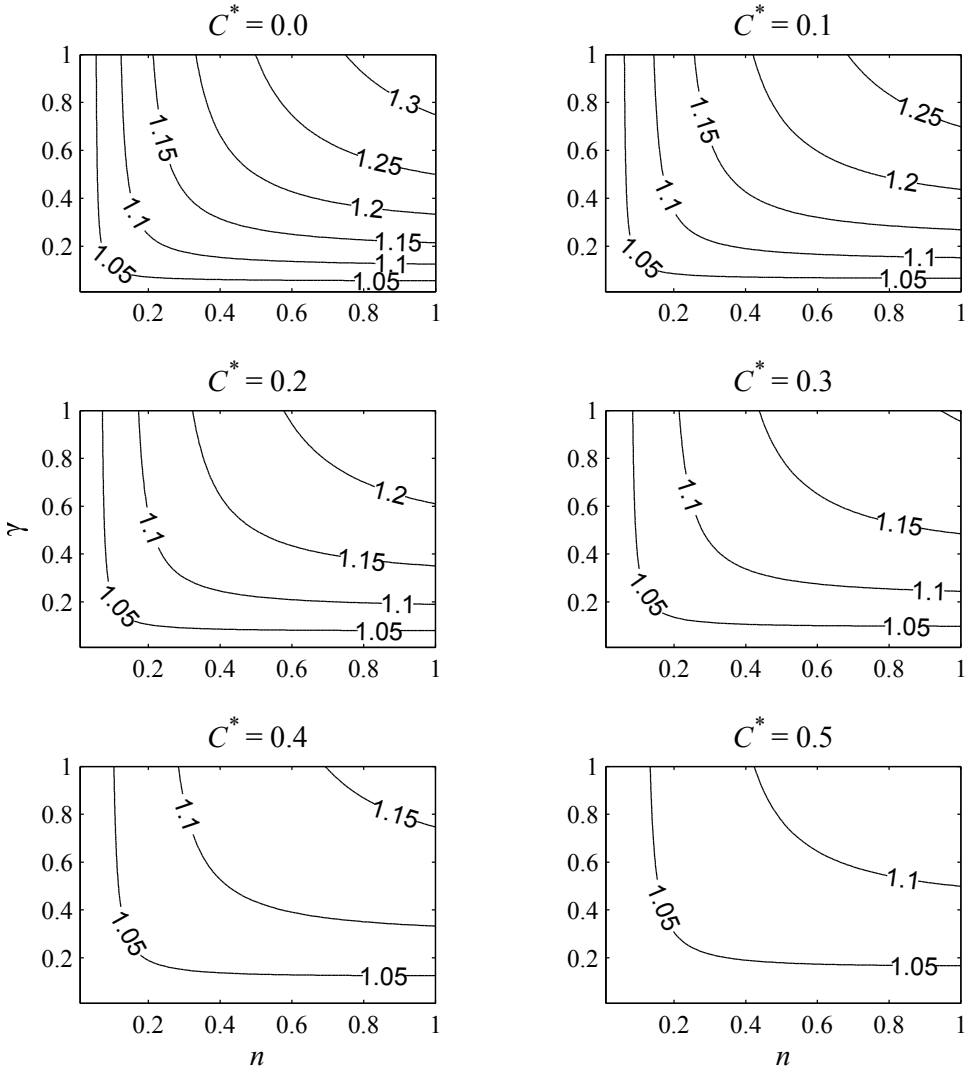

Figure 9.9: Dimensionless comparison of mean flow velocity profile for Herschel-Bulkley open-channel flows over porous bed with the ones over flat fixed beds: contours for $\bar{U}/\bar{U}|_{\gamma=0}$ for different values of C^*, as functions of n and γ.

Chapter 10

Revisiting Acquabona

Based on the model presented on the chapter before, the Acquabona test case presented on chapter 7 can be revisited. The relation found between the mean flow velocity and flow height can give a new insight of the Acquabona event of 1998.

10.1 Parameter gathering

In order to correctly employ the mathematical model proposed in chapter 8, the proper input parameters should be found. When considering the porous bed, some properties are needed: porosity of the bed p; mean particles diameter that compose the bed D_{50}; a form factor χ for the voids that would have been formed in between the sediment material in the Acquabona region.

As elucidated in Kasenow (2001), the porosity found in the dolomites are between 0.191 and 0.327. However, as the event takes place in a slope deposit region downstream the dolomite region, we considered that the soil was mainly composed by gravels and sedimentary material. We arbitrarily chose $p = 0.4$, and evaluated how the same parameter could affect the prediction of the results.

It is understood that the natural channel formed in the Acquabona region was carved by successive mass movements. In this way, we can consider that the bottom of that channel is composed by past events. Then, events reported before the event or even later events can inform the mean sediment size of particles diameter. (Gregoretti and Fontana, 2008) related

many events in the Acquabona region and a particular measure was done in August 2000 (after the event here studied). The measures point out that the mean particle size as $D_{50} = 0.137$ meter.

The void shape factor χ is the most uncertain parameter among all. Its value is often fixed between 0.1 and 4 in the literature, but no precise method to determine its value have been developed yet. The assessment of χ influence will be a part of the evaluation of the results presented. For the first simulation that is shown, we adopted $\chi = 0.25$.

10.2 Recalculating Acquabona event

Using the parameters gathered before and solving the equations, a comparison can be made using the last figure from chapter 7 and now using also a curve for the non-Newtonian rheology fluid flow when in presence of a porous bed (Figure 10.1).

It is observed that given the same specific discharge q_0, for a same fluid type, flow height is smaller when in presence of the porous bed. This is due to the reduced friction on the bottom (smaller sheared zone) induced by the slip velocity in the boundary between the bed and the flow. Close to the specific discharge q_{acqua} where $\gamma = 0.03$, the difference measured for mean flow height is about 5% from porous to fixed bed. Since less resistance is felt by flow, the velocity should be greater when in presence of a porous bed. Such reasoning was explored in chapter 10. We can construct the same kind of figure for the mean flow velocity as shows Figure 10.2, where the variation of velocity is around 5%.

Both figures presented before can be summarized by means of the parameter γ (Equation 8.18). As bed porous properties are kept constant and specific discharge is increased, h_0 increases leading to a small γ parameter. Figure 10.3 presents the same results from Figures 10.1 and 10.2 now using the ratio between mean flow properties for non-Newtonian fluids flowing over a porous bed and those for fixed bed ($\gamma = 0$).

The dimensionless parameter of porosity γ would vary from 0.02 to 0.2 depending on the flow discharge rate which promoted variations on mean flow properties of approximately 7%, as shows Figure 10.3. Such variations could be in the same order of magnitude as measurements uncertainties, thus rendering their effects unnoticeable. As elucidated on chapter 10, the

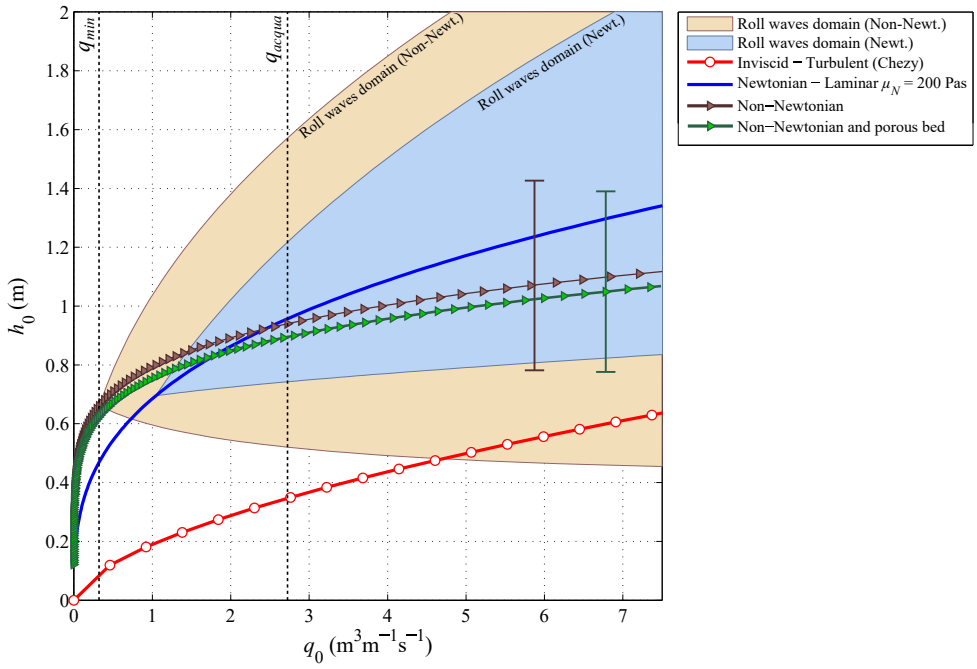

Figure 10.1: Mean flow height h_0 as function of the specific discharge q_0 for different friction laws and considering porous bed for non-Newtonian fluid. Curves represent different frictions laws. Shaded zone shows amplitudes of roll waves for the respective friction law. q_{acqua} represents specific discharge in the Acquabona creek for the event here studied based on Equation 7.11. q_{min} is the minimum specific discharge required for roll waves to appear in Acquabona creek given the non-Newtonian rheology. Vertical bar indicates prediction of mean flow height using cases from Table 7.4, for less and more non-Newtonian fluids.

porosity dimensionless parameter γ would only present significant effect (considering the scale we are currently dealing with) for great values. Since that parameter is a function of the soil properties χ, p and D_{50}, we should understand how it could change the values, consequently changing mean flow properties.

Observing now only u_0, we explored the influence of parameters χ and p on the mean flow velocity as presents Figure 10.4. From both graphics, we note that varying values from those parameters inside an acceptable range, the effect of γ can be somehow increased for highly porous media (high p, than high k_K) and for low form factor, reaching higher velocities, up to 16%

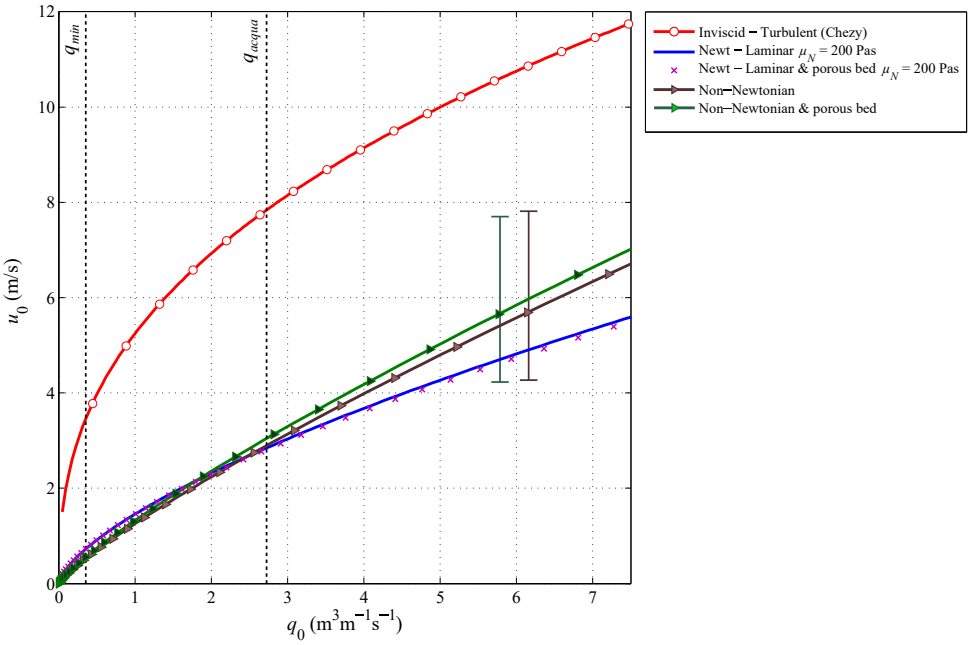

Figure 10.2: Mean flow velocity u_0 as function of the specific discharge q_0 for different friction laws and considering porous bed for non-Newtonian fluid. Curves represent different frictions laws. Shaded zone shows amplitudes of roll waves for the respective friction law. q_{acqua} represents specific discharge in the Acquabona creek for the event here studied based on Equation 7.11. q_{min} is the minimum specific discharge required for roll waves to appear in Acquabona creek given the non-Newtonian rheology. Vertical bar indicated prediction of mean flow height using cases from Table 7.4, for less and more non-Newtonian fluids.

greater than those for fixed bed.

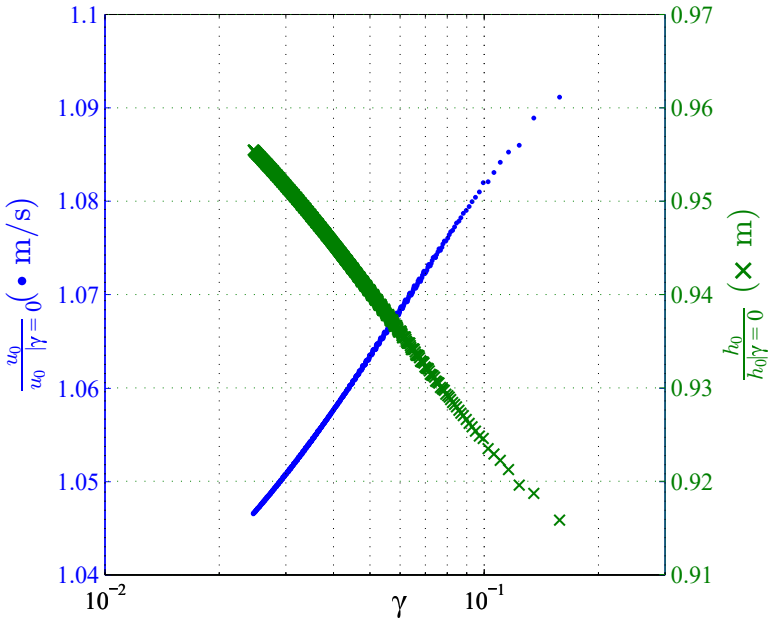

Figure 10.3: Ratio between mean flow properties (u_0 and h_0) from flow with and without porous effect as function of γ.

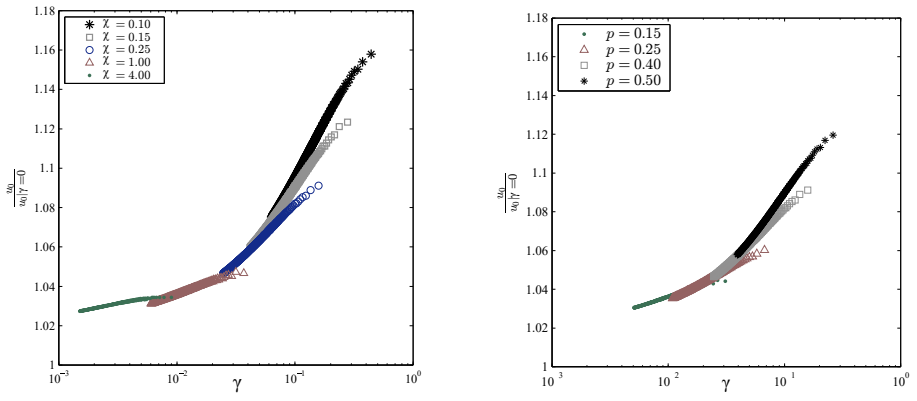

(a) (b)

Figure 10.4: Influence of 10.4(a): form factor χ; and 10.4(b): porosity p, in the relation between velocity ratio ($u_0/u_0|_{\gamma=0}$) and dimensionless of porosity γ.

Part III

Final remarks

Chapter 11

Discussion and conclusions

In this work we have investigated unsteady phenomena on open-channels flows that are related to the natural hazards named as mudflows. We have focused the research on two main stages of the development of a potential mudflow: the surface runoff and the mudflow itself.

For the first stage, an experimental approach was considered and the main idea was to inspect the time properties of the solid transport, composed by a mean value and fluctuations. The methodology here employed was developed and tested for some test cases and seems to be a powerful tool for sediment discharge study in time. A simple method for flow friction measurements was adapted from aeolian transport experiments and proved to be a reasonable method to understand the energy distribution in flow friction due to turbulent structures.

Experimental runs were performed and their results were studied regarding mean, fluctuation and spectral behaviors. It was shown that fluctuations of solid transport depend almost instantaneously on flow fluctuations following the relation between averaged transport and averaged friction. As free-surface instabilities were applied to the flow, it seems that the mean solid discharge is reduced. Conversely the fluctuations intensities of solid transport increase. This would constitute a result that could give directions for practical Engineering purpose, pointing out that instabilities presence actually diminish erosion and sediment entrainment.

For the second stage, a first-order mathematical model for roll-waves free surface instabilities was used to simulate a natural mass movement event registered in the literature. The properties of the fluid were found to greatly influence the predictability of the model, an observation greatly

mentioned in the literature. Despite that fact, the model seems to work well and to give coherent insight on the waves properties, even for a natural event. We highlight that such use of the model would have practical applications in Engineering for risk assessment and control of risk zones, although it might be required more validation based on in situ measurements.

In order to understand how the complexity of the problem would change as porosity effect was added to the problem, a mathematical model was proposed for non-Newtonian fluids flow over a porous medium. For that analytical solution, numerical simulations were performed to explore the compatibility with the mathematical results. Good agreement was found between both, although it seems that the boundary condition used would require further investigation. The test-case used to analyze the roll waves mathematical model was then reevaluated to check whether the porosity effect would change the overall prediction of a natural event.

11.1 Runoff flows and time-variable transport

11.1.1 Experimental method

The experimental method employed to assess a time-variable value for friction velocity, rather intuitive, have proven its capacity to understand the flow energy distribution in the spectral domain. The drawback in our case comes from the fact that flow and transport measurements were performed in two separate set of experiments. The method allowed a statistical analysis of the relations between mean and fluctuating quantities but not a real time relation between simultaneous values of them. Nevertheless, since the fluctuations of the velocity field showed good agreement with results from the literature, conclusions on instantaneous relation could be postulated.

The methodology employed to measure the solid discharge has proven its usefulness and allowed some analysis to be performed. One main technical issue found during experiments was that the light source used in experiments influence the results: light source should be as uniform as possible and fluid should be clean. If those conditions are respected, grayscale images have good contrast level, facilitating the distinction between fluid and shadow from particles. If no good contrast is found, images require further image processing, which might induce noise and error in particles detection. At this point, the enhancing technique developed works in most of

the times, and only results that were proven to be generated from properly detection have been studied.

Some corrections must be applied to the signals depending on the morphological characteristics of particles detected since the model uses the individual mass and velocity of each particle to calculate the solid discharge. Those corrections are explained and are corroborated by the results presented.

11.1.2 Time-dependent solid discharge in turbulent permanent flow

We developed three main analysis in the solid discharge signals: mean solid discharge against Shields number; fluctuation intensities of solid discharge; and spectral properties of non-stationary solid discharge.

The first analysis based on the mean sediment transport allowed to evaluate the quality of the results when comparing to classical empirical laws from the literature. For the experimental runs presented in steady solid discharge, results were congruent with the empirical laws of (Meyer-Peter and Müller, 1948) and (Wong and Parker, 2006).

To understand the role of fluctuations of friction velocity to the sediment transport, we derived an expression from the averaged transport, that relates both of them. This relation present a strong non-linearity when close to threshold flows ($\mathrm{Sh} \approx \mathrm{Sh}_c$). Scaling the fluctuation intensities of transport with its mean value, we observed that fluctuations are high when close to the imminence of transport ($\mathrm{Sh} \approx \mathrm{Sh}_c$) and they reach a constant value for $\mathrm{Sh} > 4\mathrm{Sh}_c$. We showed then that fluctuations of transport are related to fluctuations of flow. The constant value reached for sufficient high Shields number is related to the intensity of turbulence in flow, which should be constant given fixed geometry and flow discharge. The increase in fluctuations when close to threshold is related to the non-linearity of transport behavior due to the threshold of movement. Both effects are captured by the empirical law derived in the present work.

The power spectral density allows the observation on how sediment transport energy distribution is made. We detected that two factors can affect the way sediment transport happens in time:

- bedforms;
- turbulent fluctuations;

The PSDs show that sediment transport energy is distributed accordingly to a turbulent flow: low frequencies have high energy and high frequencies have low energy. Whenever only turbulence seems to affect the bedload transport, close to bed turbulent structures are responsible for the fluctuations found in the solid discharge. Low frequencies (thus large time scale structures) presented an energy decay in high frequencies equals to -1. This slope would correspond to the decay of energy of turbulent structures close toe bed. However, when bedforms appear, they seem to homogenize flow turbulence and the energy decay assumed the $-5/3$ exponent. This decay of energy would rather represent isotropic turbulent flow, which could only be present away from the walls (Radice et al., 2009). This fact could be an evidence on how the bedforms can alter the kind of transport mode, making turbulent structures have more influence on particles dynamics. Such observations have also been made by Guignier (2014) in experiments in closed channel flow, where they observed that mean solid discharge increase whenever bedforms starts to develop.

11.1.3 Time-dependent solid discharge in pulsating flows

For the unsteady transport when flow disturbances were applied, the first analysis shows a decrease in solid transport. Given the same flow conditions (Re, Fr and Sh), disturbing the system clearly decreases the mean solid discharge, i.e. flow capacity of transporting sediments. However, the empirical correlation keeps its power law form, conserving the exponent between 1.5 or 1.8, as presented the results.

The first logical assumption is that flow mean friction velocity has been reduced. Since the friction velocity is related to the turbulence level of the flow, we have observed the intensities of fluctuation field. Horizontal fluctuation intensities showed greater values close to the free surface, but not fluctuations close to the bed where they kept the same magnitude, and did not presented any significant reduction that could explain the decrease observed in solid transport. The explanation could lie in the waveform of the free instabilities. As observed for roll waves mathematical solutions (Noble, 2004; Ng and Mei, 1994; Toniati et al., 2015), the bottom shear stress follows the shape of the free surface, sometimes presenting a lag. The shape, like a wave train, have a trough period greater than the peak period. Such effect would make the mean bottom shear stress to be reduced when compared to the uniform and steady flow. Another possible explanation relates the elements of energy dissipation for a given averaged flow discharge allegedly

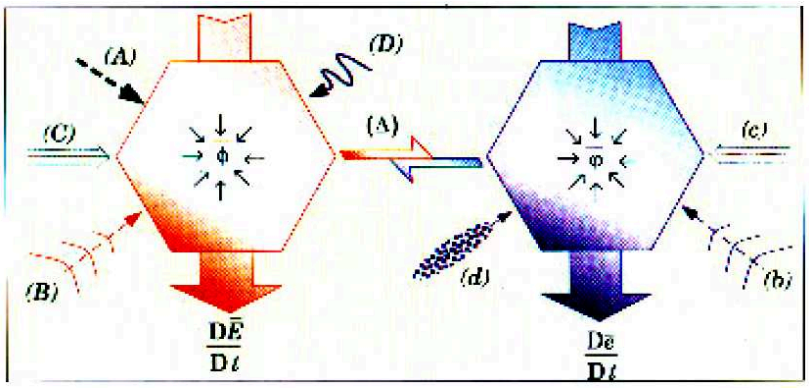

Figure 11.1: Energy budget for a turbulent volume of a flow. Total energy of flow $= \bar{E} + \bar{e}$. To the left, mean flow energy from different nature (A) volumetric (gravity in our case); (B) pressure; (C) viscous; (D) turbulence. To the right, fluctuating flow energy and their nature: (b) pressure; (c) viscosity. (d) represents the turbulent diffusion. Dissipation are noted by $\bar{\phi}$ and $\bar{\varphi}$. Δ represent the energy transfer between mean and fluctuating field. Extracted from Chassaing (2000), with authorization from Cépaduès-Editions for this specific thesis. Reproduction not authorized.

kept constant (Figure 11.1). If energy dissipation is partitioned between mean and fluctuating dissipations, the presence of waves increases the fluctuating component (which do not change mean values). This would indicate that mean flow would have less dissipation, thus inducing a reduced wall friction (related to D on Figure 11.1) responsible for the sediment transport.

The fluctuation intensities of solid discharge show an interesting aspect. Based on the results shown in Figure 5.20, we see that applying a disturbance into the free surface of the flow induces an increase in solid discharge fluctuations. As we proved, solid particles in movement follow the flow characteristics in the same way: mean solid transport are related to mean flow properties; fluctuation of solid transport are related to fluctuation intensities of flow. Free-surface instabilities do not seem to change the influence that $u'_{*\mathrm{RMS}}$ have on the flow as shown Equation 5.15 and Figure 5.20.

The power spectral density of the signals of solid transport do not bring any new information and instead corroborate what have been already discussed: for low Shields number, the -1 decay of energy is noticed; for intermediary and strong Shields number, the $-5/3$ decay takes place. Some spectral gap zones can sometimes be perceived (Singh et al., 2010), but since we are not able to direct correlate them with flow velocity fluctuations, it is not possible to confirm its origin. No evidence was found in the PSD that

the disturbance applied had direct influence on the solid discharge since no peak on waves frequency was observed. Such conclusion seems plausible as we look into flow fluctuation intensities: the effects of the disturbance on the flow appear only close to the free surface away from particles trajectories (close to bottom). Then, no direct influence should be perceived.

11.2 Mathematical models for free surface instabilities in mudflows

11.2.1 Acquabona test-case

One of the greatest issues in the geophysical scientific community is the definition of limits for characterization of different mass movement phenomena (Hungr et al., 2001). As the citation used in the first chapter of this thesis shows, even the USGS (United States Geological Survey), one of the greatest institutions in this field, does not define so straightforwardly a mass movement event. The fundamental characteristic that differentiate mass movements is the ratio water/solid sediment and their velocity propagation. Such ratio for the Acquabona creek event (chapter 6) is not well defined by researchers that collected the samples. So, the proper and correct definition of the event is compromised. Nevertheless, debris and mud flows are not distant from a rheological point of view and then allowed this research to happen and to test the mathematical model. Quantify the turbulent dissipation contribution during the event would possibly increase the uncertainties within the input parameters set to the model, rendering it less reliable.

The model used for Acquabona creek simulations has proven its usefulness when predicting mean wave properties. A relatively small discrepancy of 8% is found between predicted and mean value from measurements for waves amplitudes. The origin of such discrepancy could be explained in different ways. One possible explanation could be the difficulty to precisely quantify the rheological properties of the flowing material. The representation of such complex mixture by a rheological model implies intrinsically a limitation as rheology models average mixture behavior. As size of particles in fluid matrix may vary from dust and clay ($\approx 1\,\mu$m) to rock and boulders (≈ 1 m), their dynamics in fluid matrix are completely averaged into simplified shearing laws. Even though, assuming the Herschel-Bulkley rheological model, we were able to evaluate the effect of fluid rheological

parameters. Such matter was discussed in section 7.6 where variations of rheological properties led to a variation range of possible roll waves amplitudes of 30% for the Acquabona event.

11.2.2 More complex model for non-Newtonian flows in natural environment

One of the possible reasons for the approximative results of roll waves model when compared to field studies is that the model does not yet represent all the complexity and variability of the natural environment which could mislead the results. Then, one approximation that could enhance the results is the assumption of a porous fixed bed in the bottom of the channel. At this time, fluid is allowed to flow in between the voids present in the bed, created by the rocks and sediments. In this way, the flow would change and present a bottom slip velocity. No bedforms are considered, so bed is flat.

In this work it was presented a mathematical solution for velocity profile of laminar free surface flows of non-Newtonian fluids presenting Herschel-Bulkley rheology over a porous bed. Additional numerical simulation showed that the mathematical solution is in agreement with the simulated one. A discrepancy was found between the boundary condition imposed in the mathematical model and numerical results, which led to errors in the order of 10% on the bottom velocity u_B. The identification of form factor χ still rests empirical as no consistent methodology is able to determine how properly estimate such parameter.

The mathematical solution proved that general flow properties (h_0 and u_0) are affected by the bed. It is noticed that the flow index n is an important parameter for proper estimation of the bottom slip velocity, and this flow index can significantly change flow dynamics close to the bottom. Nevertheless, yield stress τ_0 acts in a different way reducing the overall influence of bottom on the mean flow velocity. An interesting observation is the effect of bottom velocity (non-zero due the presence of a porous flow) with rheological parameters. The presence of such velocity at the interface between channel bottom and flow decreases proportionally the size of the sheared region, thus increasing the proportion of plug zone and the mean flow velocity. This seems a rather typical behavior and influence of porous medium walls to the general flow dynamics. However, the importance of porous bed decreases as fluid become more and more non-Newtonian (in-

creasing yield or decreasing index flow). Such observation is rather direct, but since the flow discharge is considered constant, some changes in the flow height should be noticed when comparing the non-porous bed when dealing with open-channel flows.

When using the new proposed model to establish the relation flow discharge and flow height for the Acquabona test-case, we verified that for a natural environment, with a highly non-Newtonian fluid flow, the porosity does not have a significant importance in terms of flow height prediction. Since the non-Newtonian parameters play a role much more important than the porosity (when both are combined), engineering projects would be much more safe predicting with accurate values of the rheological parameters (thus decreasing their uncertainties) than considering the additional effect of porosity. What still rests unknown is how roll waves domain of generation would be altered. Following the literature (Pascal, 2006), we expect that the domain of roll waves generation would increase, i.e. roll waves would be capable to appear for lower Froude numbers. This might as well be an important factor for predicting the flow height, as it has been already discussed during the thesis.

Finally, all these observations should be verified experimentally as they would change, for example, the correct interpretation or prediction of flows by dimensionless number such as Reynolds and Froude numbers, which depend on characteristic flow variables. More numerical simulation should also be performed to better verify the boundary conditions employed in the mathematical problem. The comprehension of this kind of flow dynamics is crucial when dealing with industrial and civil structures dimensioning which relies upon such informations.

Chapter 12

Perspectives

This work gives some perspectives on how further investigations would help to understand the phenomena here studied and to improve the research on the domain.

12.1 Part I - Sediment transport in runoff flows

From the experimental point of view, even though the method employed proved its efficiency for studying sediment transport, further improvements should be sought to improve quality of results and further data analysis.

12.1.1 Technical improvements

A PIV system coupled with the PTV and with higher acquisition rate (in the same order of magnitude of the solid transport) would help further analysis and to precisely detect how flow and sediment entrainment are related to each other. In this way, small scales might be understood, and further explanation on fluctuation of transport better explained based on flow characteristics. Simultaneous measurements of friction and transport would allow cross-correlation analysis and a better understanding on the validity of the transport law in timescale description.

Concerning the solid discharge method, different image processing techniques might give different results which would have to be treated differently before the calculations of the information required. A parallel method was tested during this PhD and shown that quality of results should depend

on the quality of signal treatment (images), and not only on the images themselves.

12.1.2 Statistical analysis of particle counting events

PTV method proved to be a reasonable method for calculating the solid discharge. However, other methods should from literature could be employed to same data obtained to obtain different information. The data available from this work should have, for example, an statistical exploration from the counting signals, ignoring particles mass and velocities, in order to understand the dynamics of particles arrival events. Preliminary results were performed during this thesis and showed promising results. The method could be employed using different statistical approaches (following renewal or renewal-reward theories, for example) to explore different information from the signals.

12.1.3 Mathematical model bottom shear stress on roll waves regime

A proper mathematical approach of the effects of roll waves into the bottom shear in presence of a mobile bed seems still missing in the literature. The development of a simple formulation capable to describe how the friction is modified depending on flow parameters and bed characteristics would be useful to compare with the experimental results here presented. This project is already under development in the Brazilian research group.

12.2 Part II - Non-Newtonian fluid flows over natural environments

12.2.1 Mathematical modeling and validation

The mathematical model employed in this work to study a natural event is yet to be completely reliable. It was shown that for the Acquabona test case it has been able to give the order of magnitude of the problem. To guarantee its utility from an engineering perspective, others test cases have to be employed to satisfactorily prove its functionality. Mass movements events all across the globe have been registered in the literature and must be carefully explored to verify the robustness of the results given by the mathematical approach.

Turbulent dissipation should be also inserted inside the stress tensor of the mathematical system so its representativity range would increase. Not only on the mathematical approach but also numerical and experimentally non-Newtonian fluids with turbulent dissipation should be explored. This would assist the evaluation of the preponderant effects in a natural event like the one here studied.

12.2.2 Non-Newtonian fluid flow over porous medium

In this work, the analytical solution found for the velocity profile of a non-Newtonian fluid flow over a porous medium was tested against some numerical simulations where the fluid and flow conditions (discharge and slope) were varied. However, the effect of the geometry was not tested, thus demanding further work.

Numerical simulations would allow a better verification of the boundary condition adopted for the analytical model. Experimental runs on this would also be an important work in this matter so the boundary condition for yield fluids flowing over a porous bed could be completely validate or discarded, if so.

The next stage on the mathematical modeling would be insert the velocity profile into the shallow water equations for a Herschel-Bulkley fluid flow and obtain the roll waves equation for this problem. This would culminate on a more complex model for roll waves and verification of validity of waves parameters and domain of stability.

Bibliography

M. Agelinchaab and M. F. Tachie. PIV Study of Separated and Reattached Open Channel Flow Over Surface Mounted Blocks. *Journal of Fluids Engineering*, 130(6):061206, 2008.

M. Amir, V. I. Nikora, and M. T. Stewart. Pressure forces on sediment particles in turbulent open-channel flow: a laboratory study. *Journal of Fluid Mechanics*, 757:458–497, 2014. ISSN 0022-1120. doi: 10.1017/jfm.2014.498. URL `http://www.journals.cambridge.org/abstract_S0022112014004984`.

C. Ancey. Plasticity and geophysical flows: A review. *Journal of Non-Newtonian Fluid Mechanics*, 142(1-3):4–35, Mar. 2007. ISSN 03770257.

C. Ancey, P. Coussot, and P. Evesque. A theoretical framework for very concentrated granular suspensions in a steady simple shear flow. *Journal of Rheology*, 43:1673–1699, 1999.

C. Ancey, T. Böhm, M. Jodeau, and P. Frey. Statistical description of sediment transport experiments. *Physical Review E*, 74(1):011302, July 2006. ISSN 1539-3755.

C. Ancey, a. C. Davison, T. Böhm, M. Jodeau, and P. Frey. Entrainment and motion of coarse particles in a shallow water stream down a steep slope. *Journal of Fluid Mechanics*, 595(August), 2008. ISSN 0022-1120. doi: 10.1017/S0022112007008774.

R. A. Antonia and P.-r. Krogstad. Turbulence structure in boundary layers over different types of surface roughness. *Fluid Dynamics Research*, 28(2): 139, 2001. URL `http://stacks.iop.org/1873-7005/28/i=2/a=A06`.

A. Armanini and C. Gregoretti. Incipient sediment motion at high slopes in uniform flow condition. *Water Resources Research*, 41(12):1–8, 2005. ISSN 00431397. doi: 10.1029/2005WR004001.

A. Armanini and N. Recchia. Experimental analysis of roll waves in over-concentrated flow. In *Proceedings of: INTERPRAEVENT 2006: disaster mitigation of debris flows, slope failures and landslides*, Niigata, Japan, 2006. Universal Academy Press, Inc. Frontiers science series.

E. Audusse, C. Chalons, O. Delestre, N. Goutal, M. Jodeau, J. Sainte-marie, J. Giesselmann, and G. Sadaka. Sediment transport modelling: Saint-Venant–Exner and three layer models. In *ESAIM*, pages 1–10, 2012.

R. A. Bagnold. An Approach to the sediment transport problem from general physics. In *Physiographic and Hydraulic Studies of River*, page 42. Washingtion DC, 1966.

R. A. Bagnold. Bed load transport by natural rivers. *Water Resources Research*, 13(2):303–312, 1977.

N. J. Balmforth and C. Mandre. Dynamics of roll waves. *Journal of Fluid Mechanics*, 514:1–33, 2004.

N. J. Balmforth and A. Vakil. Cyclic steps and roll waves in shallow water flow over an erodible bed. *Journal of Fluid Mechanics*, 695:35–62, 2012.

N. J. Balmforth, I. a. Frigaard, and G. Ovarlez. Yielding to Stress: Recent Developments in Viscoplastic Fluid Mechanics. *Annual Review of Fluid Mechanics*, 46(1):121–146, 2014. ISSN 0066-4189. doi: 10.1146/annurev-fluid-010313-141424.

H. A. Barnes. The yield stress — a review or "$\pi\alpha\nu\tau\alpha\ \rho\epsilon\iota$" — everything flows? *Journal of Non-Newtonian Fluid Mechanics*, 81:133–178, 1999.

G. S. Beavers and D. D. Joseph. Boundary conditions at a naturally permeable wall. *Journal of Fluid Mechanics*, 30(1):197–207, 1967.

A. A. Beheshti and B. Ataie-Ashtiani. Analysis of threshold and incipient conditions for sediment movement. *Coastal Engineering*, 55(5): 423–430, may 2008. doi: 10.1016/j.coastaleng.2008.01.003. URL `http://linkinghub.elsevier.com/retrieve/pii/S0378383908000021`.

D. J. Bergstrom, M. F. Tachie, and R. Balachandar. Application of power laws to low Reynolds number boundary layers on smooth and rough surfaces. *Physics of Fluids*, 13(11):3277–3284, 2001.

M. Berti, R. Genevois, A. Simoni, and P. R. Tecca. Field observations of a debris flow event in the Dolomites. *Geomorphology*, 29(3-4):265–274, 1999.

M. Berti, R. Genevois, R. LaHusen, A. Simoni, and P. R. Tecca. Debris flow monitoring in the acquabona watershed on the dolomites (italian alps). *Physics and Chemistry of the Earth (B)*, 25:707–715, 2000.

D. Berzi and L. Fraccarollo. Inclined, collisional sediment transport. *Physics of Fluids*, 25(10):106601, 2013. ISSN 10706631. doi: 10.1063/1.4823857. URL `http://link.aip.org/link/PHFLE6/v25/i10/p106601/s1{&}Agg=doi`.

F. Bigillon, Y. Niño, and M. H. Garcia. Measurements of turbulence characteristics in an open-channel flow over a transitionally-rough bed using particle image velocimetry. *Experiments in Fluids*, 41(6):857–867, Sept. 2006.

R. R. Brock. *Development of roll waves in open channels*. PhD thesis, Division of Engineering and Applied Science - California Institute of Technology, Pasadena, 1967.

J. Burger, R. Haldenwang, and N. Alderman. Friction factor-Reynolds number relationship for laminar flow of non-Newtonian fluids in open channels of different cross-sectional shapes. *Chemical Engineering Science*, 65(11): 3549–3556, 2010. ISSN 00092509. doi: 10.1016/j.ces.2010.02.040. URL `http://dx.doi.org/10.1016/j.ces.2010.02.040`.

J. Burger, R. Haldenwang, R. Chhabra, and N. Alderman. Power law and composite power law friction factor correlations for laminar and turbulent non-newtonian open channel flow. *Journal of the Brazilian Society of Mechanical Sciences and Engineering*, 37(2):601–612, 2015. ISSN 1678-5878. doi: 10.1007/s40430-014-0188-1. URL `http://dx.doi.org/10.1007/s40430-014-0188-1`.

I. Burton. The social construction of natural disasters: an evolutionary perspective. In T. Jeggle, editor, *Know Risk*, pages 35–36. United Nations and Tudor Rose Publishing, Geneva, 2005.

J. Canny. A computational approach to edge detection. *IEEE Transactions on Pattern Analysis and Machine Intelligence*, 8:679–698, 1986.

I. Celik and W. Rodi. Suspended sediment-transport capacity for open channel flow. *Journal of Hydraulic Engineering*, 117(2):191–204, 1991.

G. Chambon, D. Richard, and V. Segel. Diagnostic du fonctionnement d'un bassin versant générateur de laves torrentielles et estimation de l'aléa : le cas du Réal (Alpes-Maritimes, France). *Revue Risques naturels*

en montagne, (2):140–151, 2010. URL http://www.set-revue.fr/diagnostic-du-fonctionnement-dun-bassin-versant-generateur-de-laves-torren

H. Chan, W. Huang, J. Leu, and C. Lai. Macroscopic modeling of turbulent flow over a porous medium. *International Journal of Heat and Fluid Flow*, 28(5):1157–1166, Oct. 2007.

H. Chanson, S. Jarny, and P. Coussot. Dam Break Wave of Thixotropic Fluid. *Journal of Hydraulic Engineering*, 132(3):280–293, mar 2006. ISSN 0733-9429. doi: 10.1061/(ASCE)0733-9429(2006)132:3(280).

H. Chanson, P. Lubin, and S. Glockner. Unsteady turbulence in a shock: physical and numerical modelling in tidal bores and hydraulic jumps. In R. J. Marcuso, editor, *Turbulence: theory, types and simulation*, chapter 3, pages 113–148. Nova Science Publishers, Hauppauge NY, USA, 2012.

P. Chassaing. *Turbulence en mécanique des fluides: analyse du phénomène en vue de sa modélisation à l'usage de l'ingénieur*. Collection Polytech. Cépaduès-Editions, 2000. ISBN 9782854284836. URL https://books.google.fr/books?id=l_09AAAACAAJ.

P. Chassaing. *Mécanique des Fluides*. Cépaduès, 3 edition, 2010. ISBN 978.2.85428.929.9.

M. H. Chaudhry. *Open-Channel Flow*. Springer US, Boston, MA, 2008. ISBN 978-0-387-30174-7. doi: 10.1007/978-0-387-68648-6.

Y. L. Chen and K. Q. Zhu. Couette-Poiseuille flow of Bingham fluids between two porous parallel plates with slip conditions. *Journal of Non-Newtonian Fluid Mechanics*, 153(1):1–11, 2008. ISSN 03770257. doi: 10.1016/j.jnnfm.2007.11.004.

T. Chevalier, C. Chevalier, X. Clain, J. Dupla, J. Canou, S. Rodts, and P. Coussot. Darcy's law for yield stress fluid flowing through a porous medium. *Journal of Non-Newtonian Fluid Mechanics*, 195:57–66, 2013.

R. P. Chhabra, J. Comiti, and I. Machac. Flow of non-Newtonian Fluids in fixed and fluidised beds. *Chemical Engineering Science*, 56:1–27, 2001.

V. T. Chow. Open-channel hydraulics, 1959. ISSN 0096-3941.

R. H. Christopher and S. Middleman. Power-Law Flow through a Packed Tube. *Industrial & Engineering Chemistry Fundamentals*, 4(4):422–426,

nov 1965. ISSN 0196-4313. doi: 10.1021/i160016a011. URL http://pubs.acs.org/doi/abs/10.1021/i160016a011.

M. Colombini and A. Stocchino. Coupling or decoupling bed and flow dynamics: Fast and slow sediment waves at high froude numbers. *Physics of Fluids*, 17:036602(1–19), 2005.

V. Cornish. *Ocean waves and Kindred Geophysical phenomena*. Cambridge University Press, 1934.

P. Coussot. *Rheology of Debris Flows - Study of Concentrated Dispersions and Suspensions*. PhD thesis, INPG Grenoble, 1992.

P. Coussot. Steady, laminar, flow of concentrated mud suspensions in open channel. *Journal of Hydraulic Engineering*, 32(4):535–559, 1994.

P. Coussot and C. Ancey. Rheophysical classification of concentrated suspensions and granular pastes. *Physical Review E*, 59(4):4445–4457, 1999.

P. Coussot and M. Meunier. Recognition, classification and mechanical description of debris flows. *Earth-Science Reviews*, 40(3-4):209–227, 1996. ISSN 00128252. doi: 10.1016/0012-8252(95)00065-8.

P. Coussot and J. M. Piau. On the behavior of mud suspensions. *Rheologica Acta*, 33(3):175–184, 1994.

T. R. H. Davies. Debris-flow surges - Experimental Simulation. *Journal of Hydrology*, 29(1):18–46, 1990.

C. Di Cristo and A. Vacca. On the convective nature of roll waves instability. *Journal of Applied Mathematics*, 2005(3):259–271, 2005. ISSN 1110-757X. doi: 10.1155/JAM.2005.259. URL http://www.hindawi.com/journals/jam/2005/914047/abs/.

R. F. Dressler. Mathematical solution of the problem of roll waves in inclined open channels. *Communs Pure Applied Mathematics*, 2:149–194, 1949.

H. A. Einstein. The Bed-Load Function for Sediment Transportation in Open Channel Flows. Technical report, 1950.

M. Fang, G. Yue, and Q. Yu. The study on an application of otsu method in canny operator. In *Proceedings of 2009 International Symposium on Information Processing*, volume 2, pages 109–112, 2009. ISBN 9789525726022. URL http://scholar.google.com/scholar?hl=

en{&}btnG=Search{&}q=intitle:The+Study+on+An+Application+of+Otsu+Method+in+Canny+Operator{#}0.

G. Fiorot, G. Maciel, E. Cunha, and C. Kitano. Experimental setup for measuring roll waves on laminar open channel flows. *Flow Measurement and Instrumentation*, 41:149–157, Mar. 2015.

G. H. Fiorot. Mitigação de riscos e catástrofes naturais: análise numérico-experimental de roll waves evoluindo em canais inclinados. Master's thesis, Faculdade de Engenharia de Ilha Solteira, Universidade Estadual Paulista, UNESP, Ilha Solteira, São Paulo, Brasil, 2012.

A. Fourrière, P. Claudin, and B. Andreotti. Bedforms in a turbulent stream: formation of ripples by primary linear instability and of dunes by nonlinear pattern coarsening. *Journal of Fluid Mechanics*, 649:287–328, Apr. 2010. ISSN 0022-1120. doi: 10.1017/S0022112009993466. URL http://www.journals.cambridge.org/abstract_S0022112009993466.

L. Fraccarollo and H. Capart. Riemann wave description of erosional dam-break flows. *Journal of Fluid Mechanics*, 461:183–228, July 2002. ISSN 0022-1120. doi: 10.1017/S0022112002008455.

P. Frey, C. Ducottet, and J. Jay. Fluctuations of bed load solid discharge and grain size distribution on steep slopes with image analysis. *Experiments in Fluids*, 35(6):589–597, 2003. ISSN 07234864. doi: 10.1007/s00348-003-0707-9.

R. Genevois, P. R. Tecca, M. Berti, and A. Simoni. Debris flows in Dolomites : experimental data from a monitoring system. In *2nd International Conference on Debris-Flow Hazard Mitigation*, Taipei, 2000.

R. A. T. Gomes, R. F. Guimarães, O. A. Carvalho, N. F. Fernandes, E. A. Vargas, and E. S. Martins. Identification of the affected areas by mass movement through a physically based model of landslide hazard combined with an empirical model of debris flow. *Natural Hazards*, 45(2):197–209, Feb. 2008. ISSN 0921-030X. doi: 10.1007/s11069-007-9160-z.

W. Graf and S. Altinakar. *Hydraulique fluviale: écoulement et phénomènes de transport dans les canaux à géométrie simple.* Traité de Génie Civil. Presses polytechniques et universitaires romandes, 2000. ISBN 9782880744427.

C. Gregoretti and G. D. Fontana. The triggering of debris flow due to channel-bed failure in some alpine headwater basins of the Dolomites:

analyses of critical runoff. *Hydrological Processes*, 22(13):2248–2263, jun 2008.

G. Guidicini and C. M. Nieble. *Estabilidade de taludes naturais e de escavação*. Edgar Blücher, São Paulo, 1984.

R. B. Guidugli, M. Cândido, R. S. Camargo, S. Simonsen, and C. Perioli. Manejo de corpos em desastres de massa. In *Anais do Congresso Brasileiro de Desastres Naturais*, volume 1, page 9, Rio Claro, 2012.

L. Guignier. *Analyse Physique du Transport Sedimentaire et Morphodynamique des Dunes*. PhD thesis, Institut de Physique de Rennes, Université de Rennes 1, 2014.

R. Haldenwang, P. Slatter, and R. Chhabra. Laminar and transitional flow in open channels for non-newtonian fluids. In *Proceedings of Hydrotransport 15: Fifteenth International Conference on the Hydraulic Transport of Solids in Pipes*, pages 755–768, Bannf, Canada, 2002. BHR Group.

J. P. Herzig, D. M. Leclerc, and P. L. Goff. Flow of suspensions through porous media — application to deep filtration. *Industrial & Engineering Chemistry*, 62(5):8–35, 1970. ISSN 0019-7866. doi: 10.1021/ie50725a003. URL `http://pubs.acs.org/doi/abs/10.1021/ie50725a003`.

J. Heyman. *A study of the spatio-temporal behaviour of bed load transport rate fluctuations*. PhD thesis, Ecole Polytechnique Fédérale de Lausanne, 2014.

T. D. Ho, P. Dupont, A. Ould El Moctar, and A. Valance. Particle velocity distribution in saltation transport. *Phys. Rev. E*, 85:052301, 2012. doi: 10.1103/PhysRevE.85.052301. URL `http://link.aps.org/doi/10.1103/PhysRevE.85.052301`.

X. Huang and M. H. Garcia. A herschel-bulkley model for mud flow down a slope. *Journal of Fluid Mechanics*, 374:305–333, 1998.

O. Hungr, S. G. Evans, M. J. Bovis, and J. N. Hutchinson. A review of the classification of landslides of the flow type. *Environmental & Engineering Geoscience*, 7(3):221–238, 2001.

S.-H. Hwang and H.-C. Chang. Turbulent and inertial roll waves in inclined film flow. *Physics of Fluids*, 30(5):1259–1268, 1987.

T. Ishihara, Y. Iwagaki, and Y. Iwasa. Theory of the roll wave train in laminar water flow on a steep slope surface. *Trans. of Japane Society of Civil Engineers*, 19:46–57, 1954.

R. M. Iverson. The physics of debris flows. *Reviews of Geophysics*, 35(3): 245, 1997. ISSN 8755-1209.

R. M. Iverson, M. E. Reid, M. Logan, R. G. LaHusen, J. W. Godt, and J. P. Griswold. Positive feedback and momentum growth during debris-flow entrainment of wet bed sediment. *Nature Geoscience*, 4(2):116–121, Feb. 2011. ISSN 1752-0894. doi: 10.1038/ngeo1040. URL `http://www.nature.com/doifinder/10.1038/ngeo1040`.

H. Jeffreys. The flow of water in an inclined channel of rectangular section. *Philosophical Magazine*, 49(6):793–807, 1925.

P. Y. Julien and D. M. Hartley. Formation of roll waves in laminar sheet flow. *Journal of Hydraulic Research*, 24(1):5–17, 1986.

M. Kasenow. *Applied groundwater hydrology and well hydraulics*. Water Resources Publication, 2 edition, 2001.

R. Keane and R. Adrian. Theory of cross-correlation analysis of piv images. In F. Nieuwstadt, editor, *Flow Visualization and Image Analysis*, volume 14 of *Fluid Mechanics and Its Applications*, pages 1–25. Springer Netherlands, 1993. ISBN 978-94-010-5191-0. doi: 10.1007/978-94-011-2690-8_1.

W. M. Kranenburg, J. S. Ribberink, J. J. L. M. Schretlen, and R. E. Uittenbogaard. Sand transport beneath waves: The role of progressive wave streaming and other free surface effects. *Journal of Geophysical Research: Earth Surface*, 118(1):122–139, Mar. 2013.

R. A. Kuhnle and J. B. Southard. Bed load transport fluctuations in a gravel bed laboratory channel. *Water Resources Research*, 24(2):247–260, Feb. 1988. ISSN 00431397. doi: 10.1029/WR024i002p00247. URL `http://doi.wiley.com/10.1029/WR024i002p00247`.

E. Lazar, B. DeBlauw, N. Glumac, C. Dutton, and G. Elliott. A practical approach to piv uncertainty analysis. In *27th AIAA Aerodynamic Measurement Technology and Ground Testing Conference*, volume AIAA Paper 2010-4355, 2010.

L. d. O. B. Leite. Determinação fisica e numerica de corridas de lama resultantes de ruptura de barreira retendo material viscoplastico. Master's thesis, Universidade Estadual Paulista "Julio de Mesquita Filho" - UNESP, 2009.

K. Liu and C. C. Mei. Roll waves on a layer of muddy fluid flowing down a gentle slope - a bingham model. *Physics of Fluids*, 6:2577–2590, 1994.

B. Q. Luna, A. Remaître, T. van Asch, J.-P. Malet, and C. van Westen. Analysis of debris flow behavior with a one dimensional run-out model incorporating entrainment. *Engineering Geology*, Apr. 2011. ISSN 00137952. doi: 10.1016/j.enggeo.2011.04.007.

H. Ma, J. Heyman, X. Fu, F. Mettra, C. Ancey, and G. Parker. Bed load transport over a broad range of timescales: Determination of three regimes of fluctuations. *Journal of Geophysical Research F: Earth Surface*, 119(12):2653–2673, 2014.

G. d. F. Maciel, J.-P. Vila, and G. Martinet. Roll wave formation in the non-newtonian flows. In *Anais do Congresso Brasileiro de Engenharia Mecânica - COBEM*, volume 14, Bauru, 1997.

G. d. F. Maciel, H. K. Santos, and F. O. Ferreira. Rheological analysis of water clay compositions in order to investigate mudflows developing in canals. *Journal of the Brazilian Society of Mechanical Sciences and Engineering*, 31:64–74, 2009.

G. d. F. Maciel, F. O. Ferreira, and G. H. Fiorot. Control of instabilities in non-newtonian free surface fluid flows. *Journal of the Brazilian Society of Mechanical Sciences and Engineering*, 35:217–229, 2013. ISSN 1678-5878. doi: 10.1007/s40430-013-0025-y.

J.-P. Malet, A. Remaître, O. Maquaire, C. Ancey, and J. Locat. Flow susceptibility of heterogeneous marly formations : implications for torrent hazard control in the Barcelonnette Basin (Alpes-de-Haute-Provence, France). In *Third International Conference on Debris-Flow Hazards Mitigation*, number 1996, pages 351–362, 2003.

E. Meyer-Peter and R. Müller. Formulas for bed-load transport. In *Proceedings of the 2nd Meeting of the International Association for Hydraulic Structures Research*, pages 39–64, Stockholm, 1948.

C. Montuori. *La formazione spontanea dei treni d'onde su canali a pendenza molto forte: sintesi di ricerche teoriche e interpretazione di risultati sperimentali*. Istituti Idraulici, Università di Napoli, Facoltà di Ingegneria. Instituti Idraulici, Università di Napoli, 1961. URL `http://books.google.fr/books?id=8lUfcgAACAAJ`.

C. Montuori. Discussion: Stability aspect of flow in open channels. *Journal of the Hydraulics Division*, 89:264–273, 1963.

S. Mueller, W. Llewellin, and H. M. Mader. The rheology of suspensions of solid particles. *Proceedings of the Royal Society A: Mathematical, Physical and Engineering Sciences*, 39(4):29, Aug. 2009.

D. J. Needham and J. H. Merkin. On roll waves down an open inclined channel. *Proceedings of the Royal Society A*, 394:259–278, 1984.

C. O. Ng and C. C. Mei. Roll waves on a shallow layer of mud modelled as a power-law fluid. *Journal of Fluid Mechanics*, 263:151–183, 1994.

P. Nielsen and D. P. Callaghan. Shear stress and sediment transport calculations for sheet flow under waves. 47:347–354, 2003.

P. Noble. Existence et stabilité de roll-waves pour les équations de Saint Venant. *Comptes Rendus Mathematique*, 338(10):819–824, may 2004. ISSN 1631073X. doi: 10.1016/j.crma.2004.03.019. URL `http://linkinghub.elsevier.com/retrieve/pii/S1631073X04001426`.

A. M. d. S. Oliveira and S. N. A. d. Brito. *Geologia de Engenharia*. Associação Brasileira de Geologia de Engenharia - ABGE, São Paulo, 1998.

A. V. Oppenheim and R. W. Schafer. *Discrete-Time Signal Processing*. Prentice Hall Press, Upper Saddle River, NJ, USA, 3rd edition, 2009. ISBN 0131988425, 9780131988422.

N. Otsu. A threshold selection method from gray-level histograms. *IEEE Transactions on Systems, Man, and Cyvernetics*, SMC-9(1):62–66, 1979.

D. Ould Ahmedou, a. Ould Mahfoudh, P. Dupont, a. Ould El Moctar, a. Valance, and K. R. Rasmussen. Barchan dune mobility in Mauritania related to dune and interdune sand fluxes. *Journal of Geophysical Research: Earth Surface*, 112(2):1–18, 2007. ISSN 21699011. doi: 10.1029/2006JF000500.

G. Ovarlez, S. Cohen-Addad, K. Krishan, J. Goyon, and P. Coussot. On the existence of a simple yield stress fluid behavior. *Journal of Non-Newtonian Fluid Mechanics*, 193:68–79, Mar. 2013. ISSN 03770257. doi: 10.1016/j.jnnfm.2012.06.009.

T. C. Papanastasiou. Flows of Materials with Yield. *Journal of Rheology*, 31(5):385, 1987. ISSN 01486055. doi: 10.1122/1.549926. URL `http://scitation.aip.org/content/sor/journal/jor2/31/5/10.1122/1.549926`.

D. Paphitis. Sediment movement under unidirectional flows: an assessment of empirical threshold curves. *Coastal Engineering*, 43(3-4):227–245, Aug. 2001.

J. P. Pascal. Instability of power-law fluid flow down a porous incline. *Journal of Non-Newtonian Fluid Mechanics*, 133(2-3):109–120, feb 2006. ISSN 03770257. doi: 10.1016/j.jnnfm.2005.11.007.

S. V. Patankar and D. B. Spalding. A calculation procedure for heat, mass and momentum transfer in three-dimensional parabolic flows. *Numer. Heat Transfer*, 15(10):1787–1806, 1972.

J. M. Piau. Flow of a yield stress fluid in a long domain, application to flow on an inclined plane. *Journal Rheology*, 40:711–723, 1996.

G. Pinho, C. Francisco, and C. Salgado. Análise espacial dos movimentos de massa em Nova Friburgo/RJ: o caso do desastre natural de janeiro de 2011. *Revista Tamoios*, 9(1), 2013. ISSN 1980-4490. URL `http://www.e-publicacoes.uerj.br/index.php/tamoios/article/view/5355`.

V. M. Ponce. New perspective on the Vedernikov Number. *Water Resources Research*, 27(7):1777–1779, jul 1991. ISSN 00431397. doi: 10.1029/91WR01033. URL `http://doi.wiley.com/10.1029/91WR01033`.

P. Prinos, D. Sofialidis, and E. Keramaris. Turbulent Flow Over and Within a Porous Bed. *Journal of Hydraulic Engineering*, 129(September):720–733, 2003.

A. Radice, F. Ballio, and V. Nikora. On statistical properties of bed load sediment concentration. *Water Resources Research*, 45(6):1–8, 2009.

K. R. Rajagopal. On implicit constitutive theories for fluids. *Journal of Fluid Mechanics*, 550:243–249, 3 2006. ISSN 1469-7645. doi: 10.1017/S0022112005008025.

A. R. Rao and M. Mishra. Peristaltic transport of a power-law fluid in a porous tube. *Journal of Non-Newtonian Fluid Mechanics*, 121(2-3): 163–174, aug 2004.

E. R. G. Rebello, B. E. F. C. C. Carvalho, J. A. V. Costa, M. A. S. Freitas, and O. A. Cavalcante. Condições metereológicas das chuvas fortes que atingiram a região serrana do rio de janeiro no dia 12.01.2012. In *Anais do Congresso de Desastres Naturais*, volume 1, Rio Claro-SP, 2012.

A. Recking, P. Frey, A. Paquier, and P. Belleudy. An experimental investigation of mechanisms involved in bed load sheet production and migration. *Journal of Geophysical Research*, 114(F3):F03010, Aug. 2009. ISSN 0148-0227.

A. Remaître, J.-P. Malet, O. Maquaire, C. Ancey, and J. Locat. Flow behaviour and runout modelling of a complex debris flow in a clay-shale basin. *Earth Surface Processes and Landforms*, 30(4):479–488, apr 2005. ISSN 0197-9337. doi: 10.1002/esp.1162. URL `http://doi.wiley.com/10.1002/esp.1162`.

G. L. Richard and S. L. Gavrilyuk. A new model of roll waves: comparison with Brock's experiments. *Journal of Fluid Mechanics*, 698:374–405, 2012. ISSN 0022-1120. doi: 10.1017/jfm.2012.96.

G. P. Roberts and H. A. Barnes. New measurements of the flow-curves for carbopol dispersions without slip artefacts. *Rheological Acta*, 40(11): 499–503, 2001.

N.-E. Sabiri and J. Comiti. Pressure drop in non-Newtonian purely viscous fluid flow through porous media. *Chemical Engineering Science*, 50(7): 1193–1201, 1995.

F. L. Santos. Estudo teórico-experimental em via de determinação de lei de atrito em escoamentos de fluidos hiperconcentrados, 2003.

H. Schlichting. *Boundary-Layer Theory*. McGraw-Hill, 7 edition, 1979.

A. Shields. Application of Similarity principles and Turbulence Research to bed-load movement. *Mitteilungen der Preussischen Versuchsanstalt für Wasserbau und Schiffbau*, 1936. Original version in german (Anwendung der Aehnlichkeitsmechanik und der Turbulenz Forschung auf die Geschebebewegung).

A. Singh, K. Fienberg, D. J. Jerolmack, J. Marr, and E. Foufoula-Georgiou. Experimental evidence for statistical scaling and intermittency in sediment transport rates. *Journal of Geophysical Research: Earth Surface*, 114(1):1–16, 2009.

A. Singh, F. Porté-Agel, and E. Foufoula-georgiou. On the influence of gravel bed dynamics on velocity power spectra. *Water Resources Research*, 46(4):1–10, 2010. ISSN 19447973. doi: 10.1029/2009WR008190.

A. Siviglia, G. Nobile, and M. Colombini. Quasi-Conservative Formulation of the One-Dimensional Saint-Venant–Exner Model. *Journal of Hydraulic Engineering*, (10):1521–1526, 2008.

T. Sochi. Flow of non-Newtonian fluids in porous media. *Journal of Polymer Science Part B: Polymer Physics*, 48(23):2437–2767, Dec. 2010. ISSN 08876266.

A. N. Strahler. Dynamic basis of geomorphology. *Bulletin of the Geological Society of America*, 63:923–938, 1952.

A. L. Toniati, G. D. F. Maciel, and F. d. O. Ferreira. Determinação do perfil de velocidade média e tensão de cisalhamento no fundo em escoamentos lamosos pulsantes. In *Anais do XXI Simposio Brasileiro de Recursos Hidricos*, pages 1–8, Brasilia, DF, Brasil, 2015. ABRH.

J. H. Trowbridge. Instability of concentrated free surface flows. *Journal of Geophysical Research*, 92(C9):9523–9530, 1987.

O. Ubbink and R. I. Issa. A method for capturing sharp fluid interfaces on arbitrary meshes. *Journal of Computational Physics*, 153(1):26–50, 1999.

T. W. van Asch, J.-P. Malet, L. P. van Beek, and D. Amitrano. Techniques, issues and advances in numerical modelling of landslide hazard. *Bulletin de la Société Géologique de France*, 178(2):65–88, mar 2007. ISSN 0037-9409. doi: 10.2113/gssgfbull.178.2.65.

D. a. van der A, J. S. Ribberink, J. J. van der Werf, T. O'Donoghue, R. H. Buijsrogge, and W. M. Kranenburg. Practical sand transport formula for non-breaking waves and currents. *Coastal Engineering*, 76:26–42, June 2013.

L. C. van Rijn. Sediment Transport, Part I: Bed Load Transport. *Journal of Hydraulic Engineering*, 110(10):27, 1984.

L. C. van Rijn. Unified View of Sediment Transport by Currents and Waves . I : Initiation of Motion , Bed Roughness , and Bed-Load Transport. *Journal of Hydraulic Engineering*, 133(June):649–667, 2007.

J. P. VanDoormal and G. D. Raithby. Enhancements of the simple method for predicting incompressible fluid flows. *Numer. Heat Transfer*, 7:147–163, 1984.

V. V. Vedernikov. Conditions at the front of translation wave disturbing a steady motion of a real fluid. *(Comptes Rendus) Doklady Akademiya Nauk SSSR*, 48(4):4, 1945.

H. K. Versteg and W. Malalasekera. *An introduction to computational fluid dynamics - The finite volume method*. Prentice Hall, New York, 1995.

T. Von Kármán. Mechanische ähnlichkeit und turbulenz. *Nachrichten von der Gesellschaft der Wissenschaften zu Göttingen, Mathematisch-Physikalische Klasse*, 1930:58–76, 1930.

M. Wong and G. Parker. The bedload transport relation of meyer-peter and müller overpredicts by a factor of two. *Journal of Hydraulics Engineering*, 132:1159–1168, 2006.

B. Zanuttigh and A. Lamberti. Instability and surge development in debris flows. *Reviews of Geophysics*, (45):1–45, 2007.

C. Zeng, P. Cui, Z. Su, Y. Lei, and R. Chen. Failure modes of reinforced concrete columns of buildings under debris flow impact. *Landslides*, 12(3): 561–571, June 2015. ISSN 1612-510X. doi: 10.1007/s10346-014-0490-0. URL `http://link.springer.com/10.1007/s10346-014-0490-0`.

C. Zhao, J. Gao, M. Zhang, T. Zhang, and F. Wang. Response of roll wave to suspended load and hydraulics of overland flow on steep slope. *Catena*, 133:394–402, 2015. ISSN 03418162. doi: 10.1016/j.catena.2015.06.010.

S. Zhiyao, W. Tingting, X. Fumin, and L. Ruijie. A simple formula for predicting settling velocity of sediment particles. *Water Science and Engineering*, 1(1):37–43, 2008. ISSN 16742370. doi: 10.3882/j. URL `http://dx.doi.org/10.1016/S1674-2370(15)30017-X`.

INSA de RENNES
Service des Formations

AVIS DU JURY SUR LA REPRODUCTION DE LA THESE SOUTENUE

Titre de la thèse:
On unsteady open-channel flows: a contribution to non-stationary sediment transport in runoff flows and to unstable non-Newtonian mudflow studies

Nom Prénom de l'auteur : FIOROT GUILHERME HENRIQUE

Membres du jury :
- Monsieur DE FREITAS MACIEL Geraldo
- Monsieur VALANCE Alexandre
- Monsieur DEL RIO VIEIRA Edson
- Madame CAMANO SCHETTINI Edith Beatriz
- Madame DE OLIVEIRA BORGES Ana Luiza
- Monsieur FREY Philippe
- Monsieur FRACCAROLLO Luigi
- Monsieur DUPONT Pascal

Président du jury : A. VALANCE

Date de la soutenance : 01 Juillet 2016

Reproduction de la these soutenue

Thèse pouvant être reproduite en l'état
~~Thèse pouvant être reproduite après corrections suggérées~~

Fait à Rennes, le 01 Juillet 2016

Signature du président de jury

Valene

Le Directeur,

M'hamed DRISSI

Résumé

L'objectif général de cette thèse est l'étude de d'écoulement instationnaire du type coulée de boue dans des canaux naturels. La pluie, source du débit liquide, entraine le ruissellement, responsable du mouillage du sol, de la réduction de sa cohésion et de l'érosion des petites particules de sédiments. A partir de là, le transport de sédiments peut augmenter avec le débit et la pente du sol jusqu'à ce que la concentration en particules atteignent des niveaux très importants dans la composition du fluide.

Dans une première partie, un banc expérimental a été conçu pour simuler des écoulements ruissellants sur un lit mobile. Un système de mesure a été inventé et implémenté pour mesurer le débit solide instantané et le frottement instantané. Ces systèmes sont utilisés pour étudier l'effet des ondes de surface libre sur le transport de sédiments. Ces données sont employées pour corréler les charactéristiques entre l'écoulement et le transport solide. L'analyse des résultats permet d'observer que pour un écoulement moyen donné, la présence des ondes réduit la quantité moyenne des sédiments transportés.

Dans une deuxième partie, la dynamique des écoulements très concentrés est étudiée grâce à un modèle de roll waves de première ordre pour les écoulements laminaires des fluides de type Herschel-Bulkley. Les résultats présentés indiquent que des roll waves sont certainement présentes dans un événement naturel publié et pris comme cas d'étude. Les propriétés des ondes prédites sont estimées avec un écart de 8% par rapport à l'amplitude moyenne mesurée. Finalement, la solution théorique pour le profil de vitesse est modifiée pour prendre en considération l'effet de la porosité. La solution mathématique est comparée à des simulations faites avec FLUENT. Une analyse paramétrique est effectuée, et la comparaison avec le cas d'étude déjà publié est améliorée.

En conclusion générale, les phénomènes instationnaires qui peuvent apparaitre lors de l'évolution d'une coullée de boue affectent la dynamique générale du système couplé (écoulement-transport sédimentaire) par rapport au cas permanent et uniforme. Vérifier que ce type de phénomènes peut apparaître lors d'un événement naturel comme les coulées de boue doit être une étape importante d'un projet d'ingénierie, afin de limiter les risques de dommages.

Abstract

This thesis was motivated by the need to better understand time-dependent features related to mudflow evolution on natural sloped channels. Basically, the research is focused on events that are confined in channels formed due to the topography. The rain, source of the liquid discharge, generates the runoff flow which is responsible for wetting the soil surface, promoting reduction of soil cohesiveness and erosion of small particles such as clay and sand. From this point, the sediment transport can increase as small water flows merge and form greater streams. The scenario keeps its evolution until it reaches high concentration of particles in the fluid mixture.

In the first part, to study the non-permanent feature of sediment transport, an open-channel experiment was designed for simulating runoff flow over a mobile bed. A measurement system was designed and constructed to instantaneously inspect the solid discharge of particles and the flow friction at the bed. This apparatus is further used to explore the influence of free-surface waves on the sediment transport. Hydraulic properties of flows are qualitatively and quantitatively studied and data are used to correlate characteristics of flow and sediment transport. A set of experimental runs is presented and explored. Analysis of results shows that for fixed flow conditions, waves induce an overall smaller quantity of transported sediment.

In a second part, the dynamics of high concentrated flows is addressed and this thesis attempts to apply a first-order roll-wave model for Herschel-Bulkley laminar fluid flow to a registered natural event. Results presented point out that roll waves could have occurred during this already published case-study event. Simulations could predict wave heights within 8% on uncertainty with respect to the mean amplitude of measured waves. Finally a new theoretical solution for the velocity profile is proposed taking into account the porosity of the bed. Results are then compared with numerical simulation performed in FLUENT. A parametric analysis is employed and the case-study is once again evaluated.

As general conclusion, the non-permanent phenomena that can appear during the evolution of a mudflow event affect the overall dynamics of the coupled system (hydraulic-sediment transport) in comparison to the steady and uniform case. Verifying that such phenomena could appear should indeed be an important part in hydraulic engineering projects, especially when dealing with lives, which is the case of mudflows.

INSA RENNES

N° d'ordre : 16ISAR 11 / D16 - 11

Institut National des Sciences Appliquées de Rennes
20, Avenue des Buttes de Coëmes • CS 70839 • F-35708 Rennes Cedex 7
Tel : 02 23 23 82 00 - Fax : 02 23 23 83 96